Hypoxia Signaling in Breast Tumor Progression, Dissemination, and Dormancy in the Bone

By

Vera Mayhew Todd

Dissertation

Submitted to the Faculty of the

Graduate School of Vanderbilt University

in partial fulfillment of the requirements

for the degree of

DOCTOR OF PHILOSOPHY

in

Cancer Biology

September 30, 2021

Nashville, Tennessee

Approved:

Julie A. Rhoades, Ph.D

James E. Cassat, Ph.D.

Albert B. Reynolds, Ph.D.

Rachelle W. Johnson, Ph.D

To my parents, for their inspiring example

and

To my husband, Tyler, for his constant love and encouragement

ACKNOWLEDGEMENTS

The work presented in this dissertation was made possible by the financial support of the Cellular, Biochemical, and Molecular Sciences Training Program and the R00 “Characterization of breast cancer dormancy in bone” (Rachelle Johnson). This work would also not have been possible without the support and guidance of many individuals during my graduate career.

First, I must thank my mentor, Rachelle Johnson. Thank you for teaching me so much and helping me grow and mature as a scientist. Thank you for being a constant advocate and for always being supportive of my goals. I also want to acknowledge the contributions of my thesis committee members, Julie Sterling, Al Reynolds, and Jim Cassat. Thank you all for your feedback and guidance throughout my graduate career and for pushing me to excel.

This work would also not have been possible without the contributions of my collaborators, Joshua Johnson, Lauren Himmel, Christopher Pinelli, and Miranda Clements. Thank you for your hard work and expertise.

To the dedicated members of the Johnson Lab, both past and present, thank you for making my time in the lab a joy. In particular, Tolu Omokehinde and Courtney Edwards, it has been an honor to work alongside you during these years. I cannot wait to see where you will go from here and the good that you will do. Lawrence A. Vecchi III, I could not have done this without you. Thank you for always brightening the lab with your welcoming smile and good attitude. Dhiyvaa Anandan and Katie Snow, it was a privilege to work with you and to see you grow as scientists during our time together.

I would also like to thank my parents, Wallis and Glenn, for always supporting me, encouraging me, and raising me to believe in my potential. To my mother- and father-in-law, Sharron and Shane, thank you for being my second set of parents and showing me so much love from the very beginning. Above all, to my husband, Tyler, I do not know if I could have made it here without you. Thank you for making the hard days better and for celebrating my every success, however small.

TABLE OF CONTENTS

LIST OF TABLES

LIST OF FIGURES

ABBREVIATIONS

A2BR	Adenosine receptor 2B
ADH	Atypical ductal hyperplasia
AKT	AKT serine/threonine kinase
AKT1	AKT serine/threonine kinase 1
AKT2	AKT serine/threonine kinase 2
ANGPTL4	Angiopoietin like 4
ANOVA	Analysis of variance
Arg-I	Arginase I
ARNT	Aryl hydrocarbon receptor nuclear translocator, gene encoding HIF1β protein
ATCC	American Type Culture Collection
Atg7	Autophagy Related 7
B2M	Beta 2 microglobulin
BCA	Bicinchoninic acid
Becn1	Beclin 1
BMDC	Bone marrow derived cell
BMP2	Bone morphogenetic protein 2
BSA	Bovine sereum albumin
BV/TV	Bone volume of total volume
CA	Constitutively active
CAIX	Carbonic anhydrase IX
CAM	Chorioallantoic membrane
CD133	Prominin 1
CD15	Fucosyltransferase 4
CD24	Cluster of differentiation 24
CD4	T-Cell surface glycoprotein CD4
CD44	Hematopoietic cell E- and L-selectin ligand
CD45	Protein tyrosine phosphatase receptor type C
CD8	T-Cell surface glycoprotein CD8
CDH1	E-cadherin

CDH2	N-cadherin
CK	Cytokeratin
COL1A1	Collagen type I alpha 1 chain
COL14A1	Collagen type XIV alpha 1 chain
COL23A1	Collagen type XXIII alpha 1 chain
COL3A1	Collagen type III alpha 1 chain
COL4A5	Collagen type IV alpha 5 chain
COL4A6	Collagen type IV alpha 6 chain
COL6A1	Collagen type VI alpha 1 chain
COL6A6	Collagen type VI alpha 6 chain
C-P4H1	Collagen prolyl 4-hydroxylase 1
C-P4H2	Collagen prolyl 4-hydroxylase 2
C-P4HA1	Collagen prolyl 4-hydroxylase subunit alpha 1
C-P4HA2	Collagen prolyl 4-hydroxylase subunit alpha 2
CSC	Cancer stem cells
CTNNB1	Beta-Catenin
CXCL12	C-X-C motif chemokine ligand 12
CXCR4	C-X-C motif chemokine receptor 4
DAB	3,3′-Diaminobenzidine
DAPI	4',6-Diamidino-2-Phenylindole
DEC2	Differentially expressed in chondrocytes 2, also known as SHARP1
DCIS	Ductal carcinoma in situ
DCN	Decorin
DFOM	Desferrioxamine
DMD	Dystrophin
DMEM	Dulbecco’s modified eagle medium
DN	Dominant negative
DTC	Disseminated tumor cell
ECM	Extracellular matrix
EDTA	Etheylenediaminetetraacetic acid
EdU	5-ethynyl-2’-deoxyuridine

EGFR	Epidermal growth factor receptor
EMT	Epithelial-to-mesenchymal transition
EpCAM	Epithelial cell adhesion molecule
EPO	Erythropoietin
ER	Estrogen receptor
ERBB3	Erb-B2 receptor tyrosine kinase 3
ERK	Extracellular signal-regulated kinase
F11R	F11 receptor, or junctional adhesion molecule 1
FBN2	Fibrillin 2
FBS	Fetal Bovine Serum
FDR	False discovery rate
FOXP3	Forkhead Box P3
GDF15	Growth differentiation factor 15
GEMM	Genetically engineered mouse model
GEO	Gene Expression Omnibus
GFP	Green fluorescent protein
GLUT1	Glucose transporter type 1
GP130	Glycoprotein 130
H&E	Hematoxylin and eosin
HER2	Human epidermal growth factor receptor 2, also known as ERBB2
HIF	Hypoxia inducible factor
HIF1α	Hypoxia inducible factor 1 alpha
HIF1β	Hypoxia inducible factor 1 beta
HIF2α	Hypoxia inducible factor 2 alpha
HIF3α	Hypoxia inducible factor 3 alpha
HMBS	Hydroxymethylbilane synthase
HNSCC	Human head and neck squamous cell carcinoma
HRE	Hypoxia response element
HRP	Horseradish peroxidase
IACUC	Institutional Animal Care and Use Committee
ICLAC	International Cell Line Authentication Committee

IGF	Insulin-like growth factor
IGF2	Insulin-like growth factor 2
IgG	Immunoglobulin gamma
IκBα	Nuclear factor kappa-B inhibitor alpha
ITGB8	Integrin subunit beta 8
JNK	c-Jun N-terminal kinase
KEGG	Kyoto Encyclopedia of Genes and Genomes
KLF4	Kruppel like factor 4
Krt18	Cytokeratin 18
L1CAM	L1 cell adhesion molecule
LAMA2	Laminin subunit alpha 2
LAMA4	Laminin subunit alpha 4
LAMB1	Laminin subunit beta 1
LDHA	Lactate dehydrogenase A
LEPREL2	Leprecan-Like 2, or P3H3
LIF	Leukemia inhibitory factor
LIFR	Leukemia inhibitory factor receptor
LOX	Lysyl oxidase
LOXL2	Lysyl oxidase like 2
LOXL4	Lysyl oxidase like 4
LUM	Lumican
M1	Classically activated macrophages
M2	Alternatively activated macrophages
Map1lc3a	Microtubule associated protein 1 light chain 3 alpha
Map1lc3b	Microtubule associated protein 1 light chain 3 beta
MAPK	Mitogen-activated protein kinase
M-CSF	Macrophage colony stimulating factor
MFAP2	Microfibril associated protein 2
microCT	Microcomputed tomography
MMP2	Matrix metalloproteinase 2
MMP9	Matrix metalloproteinase 9

MMTV-LTR	Mouse mammary tumor virus long terminal repeats
NANOG	Homeobox transcription factor Nanog
NCBI	National Center for Biotechnology Information
Neu	Rodent ERBB2
NFATc1	Nuclear factor of activated T cells 1
NK	Natural killer
NODAL	Nodal growth differentiation factor
NOS	Nitric oxide synthase
NOTCH1	Notch Receptor 1
NR2F1	Nuclear receptor subfamily 2 group F member 1
NSC	Non-silencing control
NSG	Non-SCID gamma
OMIM	Online Mendelian Inheritance in Man
OPG	Osteoprotegrin
OSM	Oncostatin M
OSX	Osterix
p16	Cyclin dependent kinase inhibitor 2A
p27	Cyclin dependent kinase inhibitor 1B
P4HB	Prolyl 4-hydroxylase subunit beta
PBS	Phosphate buffered saline
PCNA	Proliferating cell nuclear antigen
PCR	Polymerase chain reaction
PD-1	Programmed cell death 1
PD-L1	Programmed cell death 1 ligand
PDGF	Platelet-derived growth factor
Pdgfb	Platelet-derived growth factor subunit B
Pgk1	Phosphoglycerate kinase 1
PHD	Prolyl hydroxylase domain
PI3K	Phosphatidylinositol-4,5-bisphosphate 3-kinase
PKCδ	protein kinase C delta
PKM2	Pyruvate kinase M2

PLOD1	Procollagen-lysine,2-oxoglutarate 5-dioxygenase 1
PLOD2	Procollagen-lysine,2-oxoglutarate 5-dioxygenase 2
PR	Progesterone receptor
P/S	Penicillin/streptomycin
PTH	Parathyroid hormone
PTH1R	Parathyroid hormone 1 receptor
PTHrP	Parathyroid hormone related protein
PTHLH	Parathyroid hormone like hormone, gene encoding PTHrP protein
PyMT	Polyoma middle T antigen
RAB11B-AS1	RAB11B antisense RNA 1
RANK	Receptor activator of nuclear factor kappa-B
RANKL	Receptor activator of nuclear factor kappa-B ligand
RCC	Renal cell carcinoma
RIPA	Radioimmunoprecipitation assay
RNAseq	RNA sequencing
RPPA	Reverse phase protein array
SDS-PAGE	Sodium dodecyl sulfate polyacrylamide gel electrophoresis
SCP	Single cell progenies
SEM	Standard error of the mean
shRNA	Short hairpin RNA
siRNA	Short interfering RNA
SNAI1	Snail family transcriptional repressor 1, Snail
SNAI2	Snail family transcriptional repressor 2, Slug
SNAI3	Snail family transcriptional repressor 3
SOX2	SRY-Box transcription factor 2
Sqstm1	Sequestosome 1
STAT1	Signal transducer and activator of transcription 1
STAT3	Signal transducer and activator of transcription 3
TAZ	WW domain containing transcription regulator 1
TBS	Tris buffered saline
TBST	Trist buffered saline + 0.05% Tween-20

TCGA	The cancer genome atlas
Tek	TEK Receptor tyrosine kinase, or Tie2
TGF-β	Transforming growth factor beta
TGFB1	Transforming growth factor beta 1
TGFB2	Transforming growth factor beta 2
TPSR	Translational Pathology Shared Resource
TRAP	Tartrate-resistant acid phosphatase
TSP1	Thrombospondin 1, also known as THBS1
TWIST1	Twist basic helix-loop-helix transcription factor 1
Ulk1	Unc-51 like autophagy activating kinase 1
VANGARD	Vanderbilt Technologies for Advanced Genomics Analysis and Research Design
VCB	VH, elongin C, elongin B complex
VEGF	Vascular endothelial growth factor
VEGFA	Vascular endothelial growth factor A
VEGFR	Vascular endothelial growth factor receptor
VHL	von Hippel-Lindau tumor suppressor
VIM	Vimentin
YAP	Yes-associated protein 1
ZEB1	Zinc finger E-box binding homeobox 1
Zeb2	Zinc finger E-box binding homeobox 2

CHAPTER I

INTRODUCTION

This chapter is adapted from "Hypoxia in bone metastasis and osteolysis" published in Cancer Letters and has been reproduced in line with publisher policies.
Todd VM, Johnson RW. Hypoxia in bone metastasis and osteolysis. Cancer Lett. 2020 Oct 1;489:144-154. doi: 10.1016/j.canlet.2020.06.004. Epub 2020 Jun 16. PMID: 32561416; PMCID: PMC7429356.

Overview

Breast cancer is the most common cancer diagnosis among women in the United States, with over 275,000 women estimated to be diagnosed in 2020 [1]. Public awareness, early detection screening strategies, and advances in therapy have improved outcomes and lengthened survival of many breast cancer patients. Despite these developments, breast cancer survivors are still at risk of distant recurrence many years after initial diagnosis and treatment due to the ability of metastatic tumor cells to remain dormant for extended periods of time. Additionally, it is becoming increasingly appreciated that breast cancer cells are capable of metastasizing to distant tissue at early stages of disease [2, 3]. This leaves many patients, even those who were diagnosed at early disease stages, at risk of developing incurable bone lesions and related complications such as severe bone pain, hypercalcemia, and increased risk of fracture [4, 5]. Thus, metastatic dissemination to bone can significantly decrease life expectancy and quality of life [6]. Furthermore, the bone is the most common site of metastasis across different breast cancer subtypes [7], with approximately 70% of breast cancer patients presenting with bone metastases upon autopsy [8]. Thus, deepening our understanding of the events that regulate bone metastasis and how breast cancer cells behave once they reach the bone are crucial if we are to improve prevention and treatment of bone metastases.

Hypoxia (low oxygen tensions) is a common feature in solid tumors, since the existing vasculature cannot support the high nutrient and oxygen demands of the dense mass of rapidly proliferating malignant cells. This acts as a stimulus to trigger angiogenesis and other cellular changes to help the tumor cells adapt to survive in this hostile environment. However, tumors

will often still have regions of hypoxia even after the establishment of new blood vessels, since these new blood vessels are poorly organized and structurally abnormal, causing them to be leaky and leading to inefficient perfusion of the tumor [9]. For example, the median oxygen tension in breast tumors has been measured at approximately 28 mmHg (3.7%), whereas normal healthy breast tissue's oxygen levels were around 65 mmHg (8.6%) [10]. Similarly, squamous cell carcinoma of the uterine cervix had a median pO_2 of 9 mmHg (1.2%) while normal cervical tissue was around 42 mmHg (5.5%). The bone microenvironment is also generally hypoxic, with oxygen tensions estimated to range from 4.8 to 21.9 mmHg (0.6-2.9%) depending on the area of the bone marrow [11]. Thus, disseminated tumor cells that reside in the bone may experience severe hypoxia.

The cellular adaptations and responses of tumor cells to hypoxia have been linked to increased metastatic capability, bone destruction, and the decision of tumor cells to maintain dormancy or re-enter a proliferative state. Thus, investigating the mechanisms by which hypoxia alters tumor cell behavior is a key aspect of deepening the current understanding of tumor cell dissemination to, and dormancy within, the bone. While hypoxia clearly plays a role within both the primary tumor and the bone, this dissertation will primarily focus on hypoxia signaling within the primary tumor and its impact on tumor progression and dissemination.

Hypoxia signaling in tumor cells

Cells sense and respond to hypoxia through the hypoxia-inducible factor (HIF) signaling pathway. The functional HIF transcription factor heterodimer forms when an oxygen-sensitive α subunit (HIF1α or HIF2α) binds to the constitutively expressed β subunit (HIF1β, encoded by the ARNT gene) [12-15]. While a third α subunit variant, HIF3α, has been identified, many splice variants of HIF3α are not oxygen sensitive, cannot dimerize with HIF1β, and do not have transcriptional regulatory functions [16-19]. Furthermore, the most common isoform of HIF3α shares only 74% identity with HIF1α and 52-58% identity with HIF2α [20, 21]. Therefore, HIF3α will not be discussed further in this dissertation, since HIF1α and HIF2α are the main drivers of hypoxia responsive pathways.

Under normoxia, HIF1α and HIF2α are hydroxylated on conserved prolyl residues by prolyl hydroxylase domain-containing enzymes (PHD1-3). These hydroxylations allow the von Hippel-Lindau (VHL) E3 ubiquitin ligase to bind the α subunits and polyubiquitinate them,

marking them for degradation by the proteasome [22-24]. VHL is made up of two domains, termed α and β, where the β domain binds the hydroxylated HIF1α or HIF2α peptides [23, 25, 26]. VHL functions in a larger complex with the transcription elongation factors B and C; this complex is called the VCB complex [27-29]. PHD enzymes require molecular oxygen, α-ketoglutarate, ascorbate, and iron in order to be functional [26, 30-33]. Thus, under hypoxic conditions the PHD enzymes are non-functional and the α subunits cannot be bound by VHL and thus are not hydroxylated and degraded. This allows the dimerization and nuclear translocation of the α and β subunit complex, which functions as a transcription factor for target genes by binding to hypoxia response elements (HREs) in the promoter region [34-36] (Fig. 1).

HIF signaling regulates the expression of many genes involved in angiogenesis and metabolism, allowing cells to survive in low oxygen while they recruit new blood vessels to restore ideal oxygen tensions [37-39]. One of the key genes that is upregulated in response to HIF signaling is vascular endothelial growth factor (VEGF), which stimulates angiogenesis by binding to VEGF receptor (VEGFR) on the surface of endothelial cells and causing them to migrate and assemble into new blood vessels [40, 41]. Increased microvessel density improves the delivery of oxygen and nutrients to the hypoxic cells, supporting further cell proliferation. HIF signaling also increases glycolysis by stimulating the expression of glucose transporters, like glucose transporter type 1 (GLUT1), and glycolytic enzymes, like lactate dehydrogenase A (LDHA) [42-45]. These transcriptional changes allow cells to take up more glucose from their environment and derive sufficient energy from glycolysis alone during the time that the oxygen dependent electron transport chain is inactive, thus enabling cells to survive in oxygen-poor microenvironments.

While the primary function of VHL is to act as the negative regulator of HIF-signaling, VHL also possesses HIF-independent functions such as regulation of extracellular matrix (ECM) assembly, microtubule stabilization, transcription, apoptosis, and senescence [46]. VHL also functions as a tumor suppressor and germ-line VHL mutations can cause von Hippel-Lindau syndrome. People with VHL syndrome are predisposed to developing hemangiomas of the cerebellum and retina. Cysts can also develop in the kidneys and pancreas VHL syndrome confers an elevated risk of clear cell renal cell carcinoma and pancreatic neuroendocrine tumors [47]. It is important to note that current evidence indicates VHL syndrome or loss of functional VHL is not involved in breast cancer development [48].

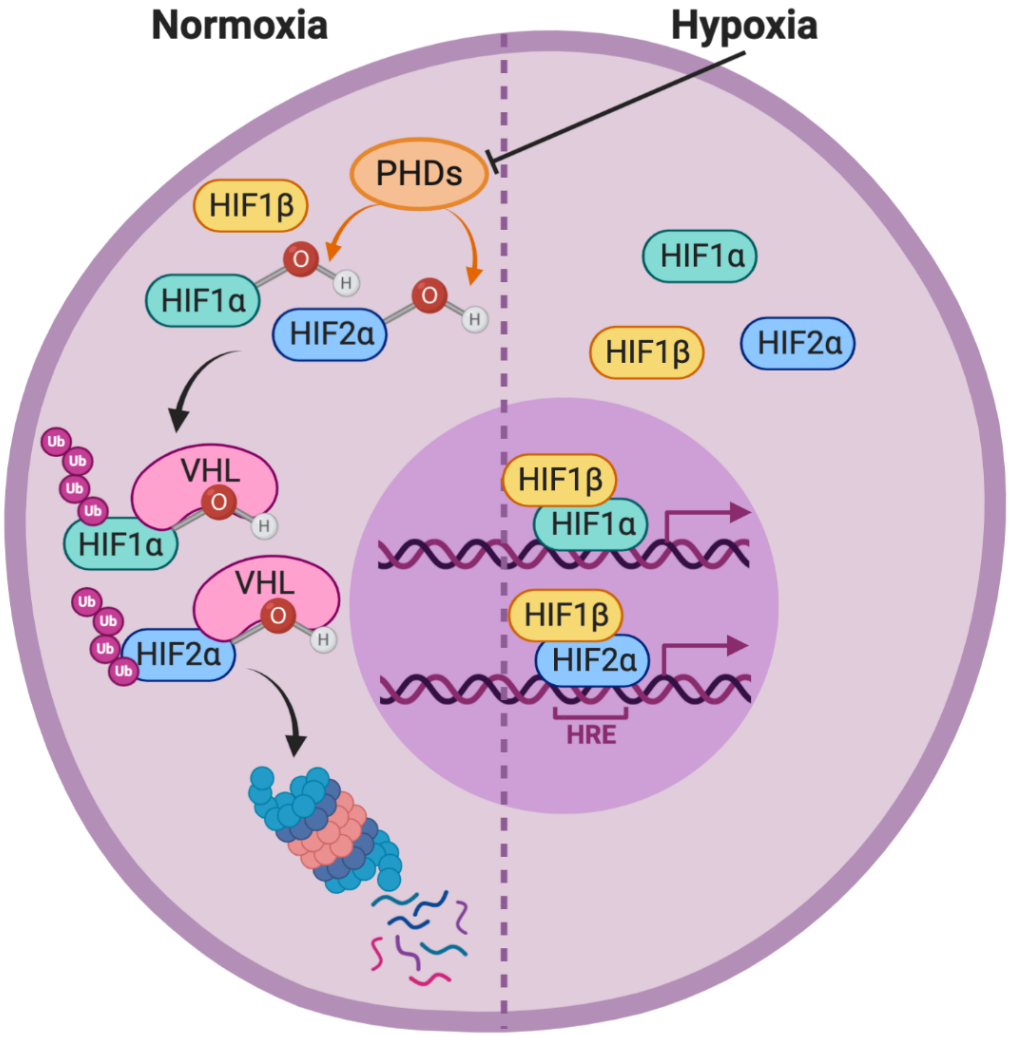

Figure 1. Hypoxia-inducible factor signaling pathway. Under normoxic conditions, prolyl hydroxylase domain containing enzymes (PHDs) hydroxylate the hypoxia inducible factor alpha subunits (HIF1α and HIF2α). These hydroxylations allow the E3 ubituitin ligase von Hippen Lindau (VHL) to ubiquitinate HIF1α and HIF2α, leading to their proteasomal degradation. Under hypoxic conditions, the PHD enzymes are inactive, allowing HIF1α and HIF2α to accumulate in the cytoplasm. The alpha subunits will then dimerize with HIF1β, enter the nucleus, and bind to hypoxia response elements (HREs) in the DNA to act as transcription factors and drive the expression of hypoxia responsive genes.

In the context of tumor cells, HIF signaling regulates genes involved in epithelial-to-mesenchymal transition, invasion, and the regulation of matrix composition and degradation, which promotes the metastasis of malignant cells [49-51]. The role for hypoxia in stimulating cancer cell invasion is documented in many cancer types including breast [52, 53], colon [54], and renal cancer [49]. Increased matrix metalloproteinase (MMP) expression and activity also drive invasion in hypoxic. HIF1α stimulates the expression of MMP9 in human breast cancer cells [53], and hypoxic regions in human breast tumor samples strongly correlate with MMP-2 activation [52]. Treating MDA-MB-231 and MDA-MB-435 human breast cancer cells with antibodies or short interfering RNAs (siRNAs) against membrane-type-1 MMP (MT1-MMP) or MMP2 reduced hypoxia-induced invasion in MDA-MB-231 and MDA-MB-435 human breast cancer cells [52]. Hypoxia not only promotes degradation of the ECM to promote invasion but can also change the composition and structure of the ECM. HIF1α, but not HIF2α, stimulates the expression of collagen prolyl 4-hydroxylase subunit alpha 1 and 2 (C-P4HA1, C-P4HA2) [55], which bind prolyl 4-hydroxylase subunit beta (P4HB) to form collagen prolyl 4-hydroxylase 1 or 2 (C-P4H1, C-P4H2), respectively. Note that these prolyl hydroxylase domain-containing proteins are distinct from the PHDs that regulate HIF1α and HIF2α subunit stability. C-P4H1 and C-P4H2 hydroxylate proline residues in collagen, maintaining thermal stability of the collagen triple helix [56]. Knocking down C-P4HA1 or C-P4HA2 in breast cancer cells decreases lung and lymph node metastases *in vivo*, highlighting the importance of ECM composition in cell adhesion, motility, and invasion [57-59]. HIF1α also stimulates the expression of procollagen-lysine,2-oxoglutarate 5-dioxygenase 1 and 2 (PLOD1 and PLOD2), which regulate collagen crosslinking and ECM stiffness [60, 61]. Matrix stiffness promotes tumor invasion and metastasis [62], and inhibiting PLOD1/2 decreases tumor stiffness and decreases invasion, lung metastasis, and the number of circulating tumor cells [57]. Taken together, inhibition of HIF signaling may decrease metastasis by targeting the physical interactions of the tumor cells with the surrounding ECM.

HIF's pro-metastatic functions are supported by clinical data from breast cancer patients, which found that more intense HIF1α staining in the primary tumor was associated with poor outcomes such as reduced overall survival, therapy resistance, and early relapse [63-66]. HIF1α overexpression was also found to be associated with shorter overall patient survival and recurrence-free survival in lung cancer [67], and increased intratumoral HIF1α staining predicts

poor outcome and response to therapy in many tumor types, including oropharyngeal cancer [68], oral squamous cell carcinoma [69], oligodendroglioma [70], epithelial ovarian cancer [71], and cervical cancer [72]. A meta-analysis of HIF2α as a prognostic marker similarly showed that high HIF2α expression was associated with decreased overall survival, disease-specific survival, disease-free survival, metastasis-free survival, and progression-free survival in patients suffering from various types of solid tumors [73]. While hypoxia has classically been considered a feature of solid tumors rather than hematological malignancies, the increased hypoxia in myelomatous and leukemic bone marrow is now well-established [74-77]. Furthermore, in acute myeloid leukemia, hypoxia promotes chemoresistance [78] and increased HIF1α expression is associated with decreased overall survival and event-free survival [79].

Hypoxia and HIF signaling also play critical roles in skeletal development and osteogenesis. For example, HIF1α and VHL expression in osteoblast-lineage cells, defined by osterix (OSX) expression, impacts bone mass in mouse models, with *Hif1α* deletion resulting in reduced bone mass and *Vhl* deletion resulting in dramatically increased bone volume [80]. Similarly, combined deletion of *PHD1, PHD2,* and *PHD3,* which stabilizes HIF, in OSX-lineage cells causes excessive trabecular bone growth due to overly active HIF signaling [81]. While the actions of HIF signaling in endochondral ossification and growth plate development, for example, are well described in the literature [8], I will focus on the role of hypoxia in metastasis, tumor growth in the bone, and osteolysis.

Blood flow and hypoxia in bone

The bone marrow is the site of hematopoiesis and thus houses a vast array of cell types including hematopoietic stem cells, various progenitor cells, mature immune cells, megakaryocytes, as well as osteoblasts and osteoclasts that control bone turnover and homeostasis. Thus, the bone marrow is highly vascularized to support the metabolic needs of all of these cells. The vascular structure of the bone was first described in the 1950s and 1960s, where it was found to possess a similar hierarchical organization of blood flow as many other organs [82-85]. The bone has large arterial vessels that feed into a dense capillary network before eventually draining into a large central vein, which in the case of long bones runs along the center of the diaphysis, the main shaft that contains the marrow [84, 86, 87]. As very dense cortical bone encases the bone marrow, blood vessels can only enter and exit the bone at specific points. High-resolution

microscopy of murine long bones has revealed that they are supplied by approximately 16 nutrient arteries that feed into the endosteal capillary network [88]. These arterial capillaries eventually connect to the venous tree, where blood drains into the large central sinus and then exits the bone through one of two exit sites. In addition, hundreds of transcortical capillaries were discovered that traverse perpendicularly through the cortical bone along the entire bone shaft, forming a direct connection between the endosteal and periosteal circulations. Surprisingly, these transcortical capillaries are responsible for roughly 80% of arterial, and 59% of venous blood flow, indicating that these small vessels are responsible for the majority of blood supply to the bone rather than the larger nutrient arteries.

Another challenge that is presented by the dense cortical bone is that it has been extremely challenging to measure the oxygen tensions within the bone marrow. Mathematical models have attempted to estimate the oxygen levels in bone marrow, but the complicated cellular composition and structural intricacies of the bone limit the accuracy of the estimates [89-91]. For example, the various bone marrow resident cell types have different oxygen consumption rates, the distribution of different cell types throughout bone marrow niches is not uniform or well defined, and the structure of the trabecular bone and capillaries beds are extremely complex. These models estimate that the oxygen tensions at the inner layer of trabecular bone range from 2.5 to 35.2 mmHg (0.3-4.6% pO_2), depending on the thickness of the trabeculum and the distance from a capillary [91].

While the oxygen levels in long bones have not yet been measured, two-photon phosphorescence lifetime microscopy has allowed for the direct measurement of calvarial bone marrow oxygen tensions in live mice [11]. This revealed that while the bone marrow is a highly vascularized tissue, the bone is a generally hypoxic organ that contains niches of severe hypoxia. Using two-photon *in vivo* imaging, Spencer *et al.* followed individual blood vessels as they ran deeper into the bone marrow. From this longitudinal analysis, they observed rapid oxygen depletion as the blood traveled from the cortical bone, a region of low cellularity, to the bone marrow, a densely cellular tissue. Endosteal regions were found to be better oxygenated, with a mean intravascular pO_2 of 21.9 mmHg (2.9%) and extravascular pO_2 of 13.5 mmHg (1.8%), compared to deeper sinusoidal regions that had a mean intravascular pO_2 of 17.7 mmHg (2.4%) and extravascular pO_2 of 9.9 mmHg (1.3%). These measurements also show that in addition to oxygen tensions decreasing along the length of the blood vessel, they drop sharply between

intravascular and extravascular readings. Thus, even bone marrow that is close to blood vessels experience low oxygen levels, with extravascular oxygen tension measurements ranging from 4.8 to 21.1 mmHg (0.6-2.8%). This rapid oxygen depletion, both longitudinally and laterally, is likely due to the high metabolic demands of the bone marrow, in accordance with its highly cellular nature and actively dividing cell populations. It is important to note that these measurements are from the calvaria of mice, which is structurally distinct from other bones such as long bones or vertebrae that are also common anatomical sites of metastasis. However, bone marrow in these other sites would likely be subject to oxygen tensions as low as what was measured here, or possibly even lower. As will be discussed below, the hypoxic conditions that bone metastatic cells and bone resident cells experience have important implications for tumor growth in the bone and osteolysis.

Hypoxia in bone metastasis

While hypoxia and active HIF signaling in primary tumors is predicted to drive distant metastasis, a direct relationship between tumor hypoxia and bone metastasis has been difficult to establish. Clinical evidence supports this theory, as increased HIF1α expression, as well as decreased VHL expression, has been observed in primary breast tumor samples from patients with bone marrow metastasis compared to those with no tumor cells detectable in their bone marrow [92].

Lu *et al.* attempted to address this question of whether HIF signaling in the primary tumor drives bone metastasis. They found that MDA-MB-231 variant cells expressing a dominant negative (DN) form of HIF1α (DN-HIF1α) formed significantly fewer bone metastases than control cells, following mammary fat pad injection [93]. Liao *et al.* performed a similar study using a genetically modified mouse model that had mammary specific deletion of *Hif1α* and expression of the polyoma middle T antigen (PyMT) that drives spontaneous mammary tumorigenesis [94]. These mice had decreased pulmonary metastasis compared to control mice, but tumor dissemination to bone was not evaluated in this study. Similarly, a recent study found that a HIF2α-driven long non-coding RNA, RAB11B-AS1, increases dissemination to, and colonization of, the lung and liver following orthotopic injection of human breast cancer MDA-MB-231 cells [95]. This study found that RAB11B-AS1 overexpression in MDA-MB-231 cells increased their migration and invasion and upregulated the expression of angiogenesis genes like

VEGFA and ANGPTL4, thereby promoting distant metastasis. While these studies establish that active HIF signaling in the primary tumor is capable of driving dissemination to distant sites, only the study by Lu *et al.* evaluated dissemination to the bone. No studies using a spontaneous tumor model have yet validated that HIF signaling factors drive bone metastasis.

Whether dissemination from the primary site to the bone is HIF dependent remains unclear, but the role of HIF signaling in tumor growth and osteolysis once tumor cells reach the bone marrow has been investigated more directly. Hiraga *et al.* generated MDA-MB-231 cells that expressed DN-HIF1α or a constitutively active (CA) HIF1α and compared tibial tumor volume following intracardiac inoculation [96]. The mice injected with DN-HIF1α cells had significantly reduced tumor burden in the tibia compared to empty vector control cells, while CA-HIF1α cells grew more aggressively in the tibia and induced greater osteolysis. CA-HIF1α cells expressed significantly higher levels of VEGF *in vitro*, and hypoxia inhibited the differentiation of mesenchymal cells (C3H10T1/2) to alkaline phosphatase-positive osteoblast-like cells in response to bone morphogenetic protein 2 (BMP2) stimulation. Hypoxia also increased Tartrate-resistant acid phosphatase (TRAP)-positive osteoclast-like cell formation from spleen cell cultures treated with soluble receptor activator of nuclear factor kappa-B ligand (RANKL) and macrophage colony stimulating factor (M-CSF). Taken together, this indicates that hypoxia causes tumor cells to recruit additional vasculature to support their outgrowth in the bone, while simultaneously shifting the activity of bone resident cells to promote osteolysis. In a separate study, HIF1α knockdown in MDA-MB-231 cells decreased bone colonization and increased survival in nude mice inoculated with the tumor cells via intracardiac injection [97]. HIF1α knockdown also decreased the microvessel density within the bone metastatic lesions they observed *in vivo*, and culturing MDA-MB-231 cells in 1% O_2 caused the cells to upregulate VEGF and CXCR4 transcription in a HIF1α-dependent manner.

When discussing bone metastasis, it is important to recognize that the immune system also impacts primary tumor growth, metastasis, and growth of disseminated cells [98]. Tumor associated macrophages have been recognized for their importance in driving angiogenesis, tumor growth, invasion, and metastasis [99-101]. In the primary tumor, the presence of regulatory T cells (Tregs) has been associated with poor prognosis [102], and Tregs are increased in the bone marrow of prostate cancer patients with bone marrow metastases [103]. In addition, Tregs have been found to produce RANKL [104], suggesting they may contribute to the cycle of

bone destruction. Cytotoxic T cells are one of the main cell types responsible for the destruction of tumor cells, but their activity can be inhibited by TGF-β released from osteoclastic resorption of bone [105, 106]. Along with cytotoxic T cells, natural killer (NK) cells are important in tumor cell destruction and are often responsible for killing metastatic cells while they are in circulation, preventing metastatic seeding [107]. Furthermore, depletion of NK cells and cytotoxic T cells has been shown to drive metastasis to bone in a 4T1 cell model of breast cancer [108].

It is important to note that many of the studies investigating the role of hypoxia in bone metastasis and tumor growth in bone have used MDA-MB-231 human breast cancer cells to model tumor growth in mice. While MDA-MB-231 cells grow aggressively and reliably colonize the bone without the need for exogenous estradiol supplementation, allowing researchers to study mechanisms involved in dissemination and osteolysis with phenotypically normal bone, they require the use of immunocompromised mice. Athymic nude mice are most frequently used, meaning the impact of T cells on the processes under investigation cannot be modeled [109]. Studies employing NSG mice would be further limited in their ability to model physiological disease processes, as they lack functional T and B cells, NK cells, macrophages, and dendritic cells [110]. Hypoxia is known to modulate the function of various immune cell populations and could thus affect the frequency of metastasis from the primary tumor, or the ability of tumor cells to colonize the bone marrow. Culturing T-cells in 1% O_2 was found to induce the expression of FOXP3, a key regulator of Treg cell differentiation, in a HIF1α dependent manner [111]. Thus, extremely hypoxic regions of the bone microenvironment may increase Treg cell differentiation and promote bone metastasis or osteolysis [102-104]. Additionally, HIF1α, but not HIF2α, was shown to drive the expression of programmed death ligand 1 (PD-L1), an immune checkpoint regulator, by binding to an HRE in the PD-L1 proximal promoter [112]. Hypoxia was found to drive PD-L1 expression in myeloid derived suppressor cells, macrophages, dendritic cells, as well as tumor cells (B16-F10, LLC, CT26, 4T1). Increased interactions of PD-L1 and PD-1 on T cells leads to the inactivation of T cells, creating a permissive environment for tumor cell growth. This could occur in the primary tumor or in metastatic lesions. Furthermore, microenvironmental acidification, a common feature among hypoxic solid tumors, can cause T cells to become anergic [113], similarly leading to a growth permissive microenvironment. Taken together, hypoxia drives the generation of a microenvironment in which T cell functions are inhibited or skewed toward an immunosuppressive phenotype.

Interestingly, HIF signaling also plays a role in macrophage polarization, where HIF1α is induced by Th1 cytokines during M1 polarization (classically activated macrophages), while HIF2α is induced in response to Th2 cytokines during M2 polarization (alternatively activated macrophages) [114]. HIF1α then drives the expression of pro-inflammatory M1 macrophage effector genes like nitric oxide synthase (NOS), whereas HIF2α regulates effectors in the anti-inflammatory, pro-repair, or tumor-associated M2 macrophages like arginase I (Arg-I). *In vitro* studies have shown that intermittent hypoxia promotes M1 polarization [115, 116]. Since primary tumors often have fluctuating oxygen levels due to inefficient and disorganized vasculature [117], these conditions could promote pro-inflammatory M1 polarization. However, with the other immune dampening effect of hypoxia, it is difficult to predict whether these M1 macrophages could still exert their typical anti-tumor effects. As a whole, hypoxia appears to dampen the anti-tumor immune response, thereby further tipping the scale in favor of tumor growth and metastasis.

As discussed above, due to the shifting metabolic needs of tumors and the abnormal vasculature that is formed, hypoxia within tumors is highly variable, heterogeneous, and transient. Thus, not all tumor cells within a tumor experience hypoxia. Harrison *et al.* modeled this heterogeneity by creating an inducible HIF1α construct [118]. They fused a mutant form of HIF1α that is stable under normoxia to a destabilization domain, creating an inducible HIF1α that is only stable in the presence of the inducer molecule trimethoprim. MCF7 cells expressing this construct were co-cultured with wild type MCF7 cells, creating a mixture of cells mimicking normoxic and hypoxic cell signaling. Increased hypoxia response gene expression was observed in wild type MCF7 cells following co-culture, as indicated by elevated VEGF, erythropoietin (EPO), and carbonic anhydrase IX (CAIX) mRNA. This suggests that cells with active HIF signaling are capable of inducing a hypoxic-like state in neighboring cells, even when these neighboring cells do not have direct hypoxia-triggered HIF activation. While the mechanism by which this occurs is unclear, these findings suggest that tumoral hypoxia in one region of the tumor could promote the invasive and metastatic capabilities of neighboring tumor cells, contributing to tumor invasion, metastasis, and poor patient outcomes.

Supporting this idea, tumor cells experiencing hypoxia have also been shown to exert effects on surrounding tumor cells in their microenvironment that promote tumor cell survival, invasion, and metastasis. Hypoxia was found to increase extracellular vesicle release from

prostate cancer cell lines (MiaPaCa and AsPC-1) in a HIF1α dependent manner, and change the size distribution of the extracellular vesicles that were released, favoring smaller vesicles [119]. Furthermore, treating these prostate cancer cells with the small extracellular vesicles released from hypoxic cells conferred a growth advantage under hypoxic conditions, compared to treatment by small extracellular vesicles collected from normoxic cells. This suggests that hypoxia not only alters the number and size of the extracellular vesicles, but also the composition of the extracellular vesicles to increase tumor cell survival in these growth-limiting conditions. Another study showed that the expression of RAB22A, a small GTPase that localizes at the plasma membrane with budding microvesicles, has been shown to be hypoxia dependent [120]. Culturing breast cancer cells (MDA-MB-231, MDA-MB-453, or MCF7) in hypoxia increased the number of microvesicles formed as well as RAB22A mRNA levels, and incubating breast cancer cells with these microvesicles induces focal adhesion formation and invasion, *in vitro*. Furthermore, RAB22A knockdown in MDA-MB-231 cells reduced pulmonary metastasis following orthotopic implantation. Clinically, RAB22A mRNA overexpression in primary tumors was found to be associated with decreased overall survival and metastasis-free survival. The implications of RAB22A induced tumor microvesicles on bone metastasis, however, was not investigated. It is unclear whether these microvesicles could localize to the bone marrow and contribute to the establishment of a pre-metastatic niche by altering the bone marrow to make an environment that is more permissive to the survival and outgrowth of metastatic cells.

Other studies have shown that tumor-derived exosomes, another type of extracellular vesicle, are capable of localizing to the bone marrow after intravenous injection, supporting the possibility that hypoxia stimulated extracellular vesicles may similarly be able to home to the bone [121]. Furthermore, tumor-derived extracellular vesicles have been shown to alter the activity of bone-resident cells in multiple tumor types [122]. For example, amphiregulin-containing exosomes released from non-small cell lung cancer cells have been found to induce EGFR signaling in pre-osteoclasts and promote osteoclastogenesis *in vitro* [123], and multiple myeloma exosomes simultaneously enhanced osteoclast activity and inhibited osteoblast differentiation and activity [124]. Additionally, exosome-mediated transfer of pyruvate kinase M2 (PKM2) from primary prostate cancer cells to bone marrow stromal cells was shown to increase CXCL12 expression in the bone marrow stromal cells in a HIF1α-dependent manner, enhancing seeding and growth of metastatic cells in the bone marrow [125]. These examples

illustrate how hypoxic tumor cell-derived extracellular vesicles may be capable of altering the bone metastatic niche, an already fertile soil for tumor cells, and make it even more amenable to metastatic seeding and outgrowth. The establishment of such pre-metastatic niches has mainly been reported in the lungs, where primary breast tumor secreted factors and extracellular vesicles have been shown to induce vascular leakiness, alter the behavior of stromal cells, remodel the ECM, trigger the recruitment of bone marrow derived cells (BMDCs) to the lungs [126-129]. These BMDCs then secrete inflammatory cytokines, growth factors, proangiogenic factors, and ECM altering factors such as matrix metalloproteinase 2 (MMP2), preparing the site for the arrival of metastatic cells [126, 127]. Tumor derived factors have also been shown to modulate the behavior of perivascular cells, inducing a phenotypic switch to a less differentiated state, marked by expression of the pluripotency gene Kruppel like factor 4 (KLF4) [130]. These perivascular cells have enhanced ECM deposition, which in turn supports metastasis. Importantly, recent research supports the notion that pre-metastatic niches can form in the bone marrow as well [125]. This new paradigm may further deepen our understanding of why certain cancer types preferentially metastasize to the bone, or why certain patients develop bone metastases while other do not.

Apart from the role of HIF signaling in the tumor cells, active HIF signaling in bone resident cells also controls metastasis to the bone. Devignes *et al.* established that HIF1α and VHL expression in osteoblast-lineage cells could influence the ability of injected tumor cells to colonize the bone [131]. When mice lacking Hif1α expression specifically in osteoblast-lineage cells ($\Delta Hif1\alpha^{OSX}$ mice) were inoculated with a PyMT-derived cell line via intracardiac or orthotopic injection, $\Delta Hif1\alpha^{OSX}$ mice developed bone metastases less frequently than control mice. Interestingly, the primary tumors that grew after orthotopic injection were also significantly smaller in $\Delta Hif1\alpha^{OSX}$ mice. Conversely, ΔVhl^{OSX} mice developed bone metastases more frequently and more rapidly than control mice after intracardiac or orthotopic injection, and grew larger, more proliferative primary tumors. This indicates that signals from bone resident cells are capable of controlling distant tumor proliferation. This bone-imposed control of tumor growth was found to be CXCL12 mediated, where $\Delta Hif1\alpha^{OSX}$ mice had decreased numbers of $CXCL12^{+}$ osteoprogenitor cells, whereas ΔVhl^{OSX} mice had significantly more $CXCL12^{+}$ osteoprogenitor cells and also had higher circulating plasma CXCL12 levels. CXCL12 expression can be induced by hypoxia [132-135] and is known to promote mammary tumor cell

growth and dissemination by signaling through CXCR4 on breast cancer cells [136]. These findings underscore the fact that the effects of hypoxia and HIF signaling do not only have local effects, but can exert control on distant seemingly unrelated organs to impact tumor growth.

Hypoxia's role in tumor-induced osteolysis

Hypoxic signaling in the bone can exert distant effects on tumor cells to influence their growth and metastasis, but HIF signaling in tumor cells can also have distant effects on the bone to promote osteolysis and prepare the bone for colonization (Fig. 2). One such hypoxia-induced tumor-secreted factor is lysyl oxidase (LOX). The LOX family of secreted copper-dependent amine oxidases covalently crosslink collagen and elastin to increase ECM stiffness, which has been shown to increase tumor cell invasion in breast and colorectal cancer [62, 137, 138]. LOX expression can be HIF1α induced, and increased expression of some LOX family members has been reported in colorectal, breast, prostate, lung, and bladder cancer [137-141]. Reynaud *et al.* identified that tumor-secreted LOX in colorectal cancer generates osteolytic lesions in mice following intra-arterial inoculation of LOX overexpression Hct116 human colorectal cancer cells [142]. LOX overexpression led to greater total bone lysis area, increased bone tumor burden, and increased numbers of osteoclasts in the bone. Furthermore, treating LOX overexpressing Hct116 tumor bearing mice with a LOX inhibitor prolonged metastasis-free survival to control levels, confirming that LOX is capable of driving this increased metastasis and osteolysis. Similar findings are reported from Cox *et al.* in the context of breast cancer showing that LOX drives osteoclastogenesis [143]. They found that injecting mice with 4T1 mouse mammary carcinoma cells (expressing high levels of LOX) resulted in osteolytic lesion formation, which could be mitigated by genetic silencing or antibody-based inhibition of LOX. Additionally, they found that LOX acts as a potent activator of osteoclastogenesis by triggering the nuclear translocation of nuclear factor of activated T cells 1 (NFATc1), the master regulator of osteoclastogenesis. Pre-conditioning mice with conditioned media from 4T1 cells increased tumor burden following intracardiac injection of 4T1 cells, suggesting that LOX secreted by tumors induces osteoclastogenesis to create a pre-metastatic niche that is more favorable for tumor growth.

LOX is, of course, not the only driver of osteolytic lesion development. Parathyroid hormone related protein (PTHrP) expressed by bone resident tumor cells disrupts the balance between bone formation and degradation and drives a process called the vicious cycle of bone

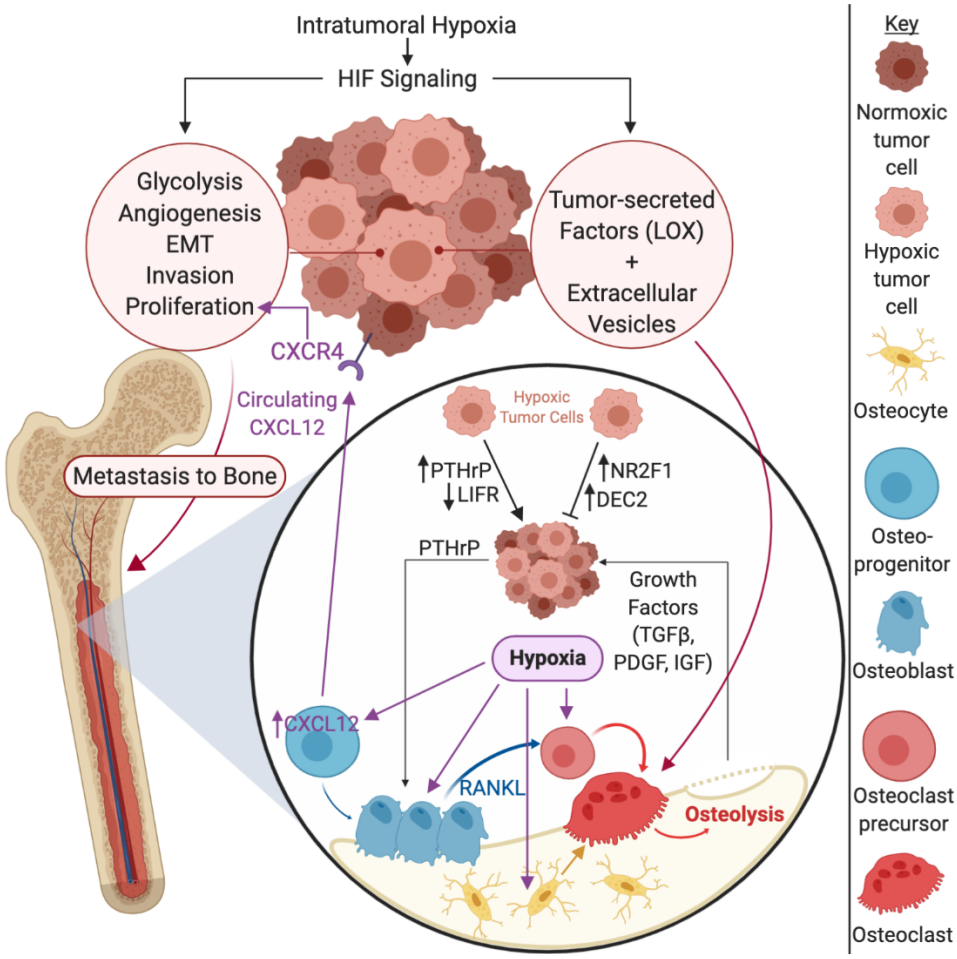

Figure 2. Hypoxia driven factors in the primary tumor and bone metastatic site. Intratumoral hypoxia in the tumor drives hypoxia inducible factor (HIF) signaling within tumor cells, which drives pro-survival and pro-metastatic processes such as glycolysis, angiogenesis, epithelial-to-mesenchymal transition (EMT), invasion, and tumor cell proliferation. HIF signaling also causes tumor cells to secrete factors such as lysyl oxidase (LOX) and to alter extracellular vesicle production, promoting osteolysis. Once tumor cells reach the bone, a physiologically hypoxic microenvironment, hypoxic tumor cells can be maintained in a dormant state, marked by increased expression of nuclear receptor subfamily 2 group F member 1 (NR2F1) and differentially expressed in chondrocytes 2 (DEC2). On the other hand, hypoxia may drive tumor cells out of dormancy by inducing parathyroid hormone related protein (PTHrP) expression and down regulating leukemia inhibitory factor receptor (LIFR), promoting the establishment of clinically significant metastatic lesions. Hypoxia also promotes the expression of PTHrP, driving the vicious cycle of bone destruction. Hypoxia in the bone also promotes osteolysis by direct stimulation of osteoclastogenic factors by osteoblasts, bone marrow stromal cells, and osteocytes. Intermittent hypoxia also stimulates osteoclastogenesis and osteoclast function. Additionally, hypoxia stimulates CXCL12 expression on osteoblast progenitors and increases circulating CXCL12 levels, which can stimulate the growth and metastasis of primary breast cancer cells through CXCR4, indicating that hypoxia in the bone can exert effects on the primary tumor site as well. Additional abbreviations: TGFβ = transforming growth factor receptor beta; PDGF = platelet derived growth factor; IGF = insulin-like growth factor.

destruction [144]. This vicious cycle is observed in several cancer types but has been mainly characterized in breast cancer. In this cycle, tumor cells growing in the bone marrow produce PTHrP [145-150], which functions in a similar manner to parathyroid hormone (PTH). PTH stimulates calcium release from bone as a homeostatic mechanism to maintain proper calcium levels in the blood [151]. PTHrP binds to the parathyroid hormone 1 receptor (PTH1R) on the surface of osteoblasts [152-154], which will in turn stimulate the production of RANKL and inhibit osteoprotegrin (OPG) production from osteoblasts [155]. RANKL can then bind RANK on the surface of osteoclast precursors to stimulate their maturation [156-158]. OPG is a soluble decoy receptor for RANKL [159], so an increase in RANKL and a decrease in OPG will collectively increase osteoclastogenesis and bone resorption, causing the release of growth factors such as transforming growth factor β (TGF-β), platelet-derived growth factor (PDGF) and insulin-like growth factors (IGFs) that are stored in the bone matrix [160-164]. These growth factors will then stimulate the growth of the tumor cells to drive the cycle forward and cause further osteoclastogenesis and osteolysis [144, 165, 166]. HIF signaling is known to partially drive this process, as HIF2α, but not HIF1α, stimulates the expression of PTHrP [167]. Thus, the hypoxic conditions that metastatic tumor cells experience in the bone, a generally hypoxic organ, could promote PTHrP production from tumor cells. Recent studies have also shown that PTHrP expression is hypoxia inducible in chondrocytes, confirming that this regulation is not specific to breast cancer cells alone [168, 169]. PTHrP transcription in chondrocytes is responsive to both HIF1α and HIF2α, though, indicating that the exact mechanism of regulation may be subtly different between cell types [169]. Hypoxia has also been shown to drive RANK and RANKL expression in breast cancer cells [170], potentially driving osteolysis through a more direct tumor-osteoclast interaction.

Hypoxia can also cause other cell types in the bone to produce osteoclastogenic factors. Hypoxia causes osteoblastic cells to upregulate VEGF [171, 172] production, bone marrow stromal cells to increase insulin-like growth factor 2 (IGF2) production [173], and osteocytes to upregulate the production of growth differentiation factor 15 (GDF15) [174], all of which promotes osteoclastic differentiation. Interestingly, HIF-signaling in osteoblasts has also been shown to drive OPG production, thus inhibiting osteoclastogenesis [81, 175]. There are some conflicting reports, however, on whether the regulation of RANKL, a key osteoclast stimulatory factor, is HIF dependent. Lee *et al.* recently reported that genetic deletion of HIF2α in

osteoblasts (using Col1a1-Cre) resulted in mice with increased bone mass, and that RANKL is regulated in a HIF2α-dependent manner [176]. Wu *et al.* had previously reported that increased HIF signaling resulting from genetic deletion of PHD2 and PHD3 in osteoprogenitor cells (using Osx-Cre) caused increased bone mass through the induction of OPG but did not alter RANKL production of osteoblasts [81]. Additionally, Wu *et al.* created variants of the PHD2/3 knockout mice expressing constitutively active forms of HIF1α or HIF2α in their osteoblasts and confirmed that RANKL expression was not significantly increased in either case. These findings are consistent with a report by Shao *et al.* in which they found that *in vitro* deletion of VHL in primary calvarial osteoblasts, and thus upregulation of HIF1α (HIF2α was not evaluated), increased OPG expression but not RANKL expression [175]. Furthermore, these results are supported by earlier reports that VHL deletion in osteoblasts causes high bone density [177]. The reason for the differing results pertaining to the role of HIF2α in RANKL induction is unclear but could be due to differences in the mouse strains or genetic markers used for osteoblast-specific deletion of targets of interest. Taken together, it is clear that HIF signaling is capable of modulating the activity of many bone resident cells and plays a critical role in the regulation of bone turnover and the development of osteolytic lesions.

Hypoxia has also been shown to stimulate osteoclastogenesis more directly. Arnett *et al.* found that culturing mouse marrow cells with M-CSF and RANKL on dentine in 2% oxygen *in vitro* increased resorption area by 9.5-fold and osteoclast number by 3.5-fold over a 13 day period, compared to atmospheric oxygen tensions [178]. Interestingly, culturing mature rat osteoclasts on dentine in low oxygen tensions reduced the number of osteoclasts and the resorption area, suggesting that the hypoxic stimulation of osteolysis is likely acting on pre-osteoclasts. These experiments were performed in sealed flasks that were filled with gas mixtures containing specific percentages of oxygen, and re-gassed daily. This means that the exact oxygen tension in the flask would fluctuate as the oxygen is depleted and then replenished, causing the cells to undergo cycles of reoxygenation. A later study using a gloved hypoxia chamber confirmed that short-term hypoxia (24 hours) stimulates osteoclast activity but also initiates osteoclast apoptosis [179]. Furthermore, this study confirmed that reoxygenation following short-term hypoxia is able to rescue osteoclasts from apoptosis, indicating that short-term hypoxia may promote osteoclastogenesis, while osteoclasts are unable to survive in extended periods of hypoxia. A recent study confirmed that constant hypoxia inhibits osteoclast

differentiation, and thus bone resorption, and found that this was mediated by decreasing the phosphorylation of c-Jun N-terminal kinase (JNK) and nuclear factor kappa-B inhibitor α (IκBα) [180]. This study also found that hypoxia abrogated NFATc1 transcriptional upregulation in response to M-CSF and soluble RANKL treatment in RAW264.7 macrophage cells or bone marrow derived monocytes. Several studies also show that HIF1α induction inhibits osteoclastogenesis [181-183], but some of the findings indicate that osteoclast differentiation in hypoxia enhances the resorptive capabilities of the cells once they mature [182]. Thus, the regulation of osteoclastogenesis and osteoclast activity appears to be very sensitive to the severity and duration of hypoxia, as well as the timing of when the differentiating cells experience hypoxia.

A recent study proposed a promising new hypoxia modulating therapeutic avenue to treat bone metastases and decrease osteolytic bone destructions [184]. Transcutaneous CO_2 administration increases the CO_2 concentration in the treated tissues, causing increased oxygen unloading from hemoglobin in red blood cells. Following intratibial inoculation of mice with MDA-MB-231 cells, transcutaneous CO_2 administration decreased tumor growth by 2-fold, inhibited osteolysis, and significantly decreased HIF1α stabilization. The number of osteoclasts was also significantly decreased and RANKL expression in the bone was similarly inhibited. Notably, transcutaneous CO_2 treatment was initiated 4 weeks post tumor cell inoculation, and was only performed for 10 minutes, twice a week, for 2 weeks. The ability of this minimally invasive treatment to stall the growth of established tumors makes it a clinically attractive avenue that warrants further investigation.

Since high intratumoral HIF1α and HIF2α levels are known to correlate with poor patient outcomes in many cancer types, as discussed previously, several HIF1α and HIF2α targeting agents have been tested clinically. PX-478, a selective HIF1α inhibitor (NCT00522652), EZN-2968, an antisense oligonucleotide inhibitor of HIF1α (NCT00466583 and NCT01120288), and RO7070179, a HIF1α mRNA antagonist (NCT02564614), have all completed phase 1 clinical trials for patient with advanced solid tumors. One of the EZN-2968 trials (NCT01120288) exhibited some preliminary evidence that this agent was capable of decreasing HIF1α mRNA and proteins levels in solid tumors but had to be closed prematurely when further development was suspended [185]. Several trials investigating HIF2α inhibitors are also currently underway, most of which focus on clear cell renal cell carcinoma: PT2977 (Phase

1 NCT02974738 and Phase 2 NCT03634540), MK-6482 (Phase 3 NCT04195750), PT2385 (Phase 1 NCT02293980 and Phase 2 NCT03108066, NCT03216499). An RNA interference therapeutic (ARO-HIF2) is also currently under investigation in a phase 1 trial (NCT04169711). In addition to these drugs that directly target HIF subunits, some drugs are being developed that are only activated in hypoxia in hopes of improving tumor-specific drug activity. For example, TH-302, a hypoxia-activated prodrug has completed phase 1 testing for use in treating patients with advanced kidney cancer or liver cancer that cannot be removed by surgery (NCT01497444). Thus, while hypoxia targeting therapies are not currently in routine clinical use, this therapeutic direction is actively under investigation.

Hypoxia's role in tumor dormancy

Upon tumor dissemination to bone, the cells may begin to grow and form clinically detectable macrometastatic lesions that degrade the bone and cause severe bone pain, fractures, and hypercalcemia [186, 187]. Alternatively, tumor cells may enter a dormant state after arrival in the bone, where they can remain for a prolonged period before eventually growing into a macrometastatic lesion. The theory of tumor dormancy is supported by clinical observations that some cancer patients relapse many years after initial treatment and declaration of "cancer free" status. In breast cancer, estrogen receptor (ER) positive disease is particularly notable for its long window between initial treatment and relapse [188]. Additionally, the bone is the most common site of metastasis for breast cancer [7]; thus, tumor dormancy in bone is frequently studied in the context of this disease.

Tumor dormancy remains a poorly defined process, and multiple types of dormancy have been described and hypothesized [188]. The most commonly accepted definition of dormancy is a non-proliferative quiescent tumor cell that is arrested in G_0-G_1 phase of the cell cycle, as indicated by negative staining for Ki-67 and/or proliferating cell nuclear antigen (PCNA) [189, 190]. In this "cellular dormancy" model, some reactivation stimulus would cause this dormant disseminated tumor cell to reenter the cell cycle, proliferate, and grow into a detectable metastasis. In the "micrometastatic dormancy" model, the disseminated tumor cell exists in the context of a cluster of cells as a clinically undetectable micrometastasis. These micrometastases are hypothesized to have balanced rates of proliferation and cell death, leading to a stable micrometastasis. Another mechanism that has been proposed in the micrometastatic dormancy

paradigm is the possibility that micrometastases may be composed of slow cycling cells that take an extended period to grow into a lesion that is large enough to be clinically detected. In either case, this model posits that the disseminated tumor burden remains static until the tumor cells are reactivated by exogenous stimuli. It is important to note that these models are not mutually exclusive. Individual quiescent cells may exist in the context of a micrometastasis, and a cell could first escape cellular dormancy, grow into a micrometastasis, where it again stalls for a period, before eventually developing into an overt metastasis.

Hypoxia and angiogenesis are proposed to play key roles in dormancy by limiting the availability of nutrients that tumor cells need in order to proliferate. This "angiogenic dormancy" model proposes that the inability of the disseminated tumor cells to induce angiogenesis is what keeps them what growing past approximately 1-2 mm in diameter [191]. High expression of anti-angiogenic factors such as thrombospondin 1 (TSP1 or THBS1) in the microenvironment [192] or low expression of angiogenic signals such as VEGF and basic fibroblast growth factor (bFGF) in the tumor cells may cause the micrometastasis to remain static in size [191].

Hypoxia also alters the expression of genes in the tumor cells that are involved in dormancy maintenance, such as leukemia inhibitory factor receptor (LIFR), which acts as a breast cancer tumor suppressor in MCF7 (ER-positive human breast cancer) cells [193, 194] and confers a dormant phenotype in bone-disseminated MCF7 breast cancer cells [195]. Hypoxia decreases the expression of LIFR in both MCF7 and SUM159 (ER-negative human breast cancer) cells *in vitro* and is negatively correlated with LIFR mRNA levels in patient samples [195]. LIFR regulation was, however, found to be HIF-independent, suggesting that HIF signaling is not required for hypoxia to influence dormancy in the bone marrow. LIFR downregulation was observed when breast cancer cells were cultured at 0.5% pO_2, suggesting that regions of extreme hypoxia in the bone marrow may promote tumor cell exit from dormancy. Furthermore, as tumors grow in the bone marrow they will become increasingly hypoxic, which may lead to prolonged repression of LIFR. Additionally, PTHrP has been shown to negatively regulate the expression of LIFR [172] and other dormancy genes in MCF7 breast cancer cells *in vitro* [196]. Since PTHrP is hypoxia responsive [167], this demonstrates another mechanism by which hypoxia may push tumor cells out of dormancy.

There is also evidence that suggests hypoxia may promote dormancy. The dormancy markers NR2F1 (Nuclear Receptor Subfamily 2 Group F Member 1) [197, 198] and DEC2

(Differentially Expressed In Chondrocytes 2, also known as SHARP1) [199] have been reported to be co-expressed with HIF1α and GLUT1, hypoxia markers, in MDA-MB-231 cells in primary tumors following mammary fat pad injection [200]. Analysis of human head and neck squamous cell carcinoma (HNSCC) patient samples similarly showed that hypoxic GLUT1-high portions of tumors frequently had upregulated NR2F1. Additionally, growing HEp3 HNSCC cells using the chick chorioallantoic membrane (CAM) model, non-cycling cells were shown to exhibit more intense pimonidozole staining, which is a marker of hypoxia. Similarly, treating CAM-implanted tumors with desferrioxamine (DFOM, a hypoxia mimicking drug that causes the accumulation of HIF1α) showed that DFOM treated tumors had significantly more quiescent cells. Collectively, these findings suggest that hypoxia may also promote quiescence in the primary tumor.

Interestingly, NR2F1 appears to function differently as a dormancy regulator depending on the site of tumor growth. Following subcutaneous implantation, growth, and resection of HEp3 cells in mice, NR2F1 was knocked down using a tetracycline-inducible method in order to study the effect of NR2F1 expression on the growth of disseminated tumor cells (DTCs) in the lung and bone marrow [197]. While NR2F1 knockdown allowed the disseminated HNSCC cells in the lung to grow more aggressively, NR2F1 knockdown had the opposite effect on bone-disseminated cells, suggesting that NR2F1 expression promotes tumor cell growth or survival in bone. Thus, some dormancy maintenance factors may act in a tumor-type or tissue-type specific manner. It is also important to note that NR2F1 has not been shown to be directly induced by HIF.

These seemingly opposing findings for the role of hypoxia in dormancy maintenance or escape may be explained by the degree of hypoxia that the cells experience or the size and location of the bone metastatic lesion. A better understanding of the cellular and molecular makeup of heterogeneous lesions in the bone metastatic niche is needed to understand the impact of hypoxia on tumor dormancy in bone. Pro-dormancy effects of hypoxia have also not been observed in the context of the bone, suggesting that other signals from the microenvironment may alter how cells respond to hypoxia.

Another avenue by which hypoxia may influence dormancy or the survival of DTCs, is through promoting the stem-like status of cancer cells. It has been proposed that disseminated tumors cells may adopt a cancer stem cell phenotype, thereby allowing the cell to survive in

circulation and grow from a single disseminated tumor cell into a metastasis in the secondary site [201]. Indeed, dormant DTCs and pluripotent stem cells share some prominent characteristics, such as self-renewal and differentiation, quiescence, and chemotherapeutic resistance [201]. It is therefore theorized that the DTCs that survive, escape dormancy, and grow into clinically detectable metastases may be cancer stem cells (CSCs). Hypoxia has been shown in multiple cancer types to promote a CSC phenotype. In breast cancer, hypoxia-induced HIF1α expression was found to increase expression of adenosine receptor 2B (A2BR) in multiple breast cancer cell lines, driving CSC enrichment *in vitro* and lung metastasis *in vivo* [202]. CSC enrichment was measured by mammosphere formation and aldehyde dehydrogenase expression *in vitro*, and A2BR signaling was found to drive this enrichment through activation of protein kinase C-δ (PKCδ). PKCδ in turn activated STAT3, driving the expression of interleukin 6 and NANOG, which are two key mediators of the CSC phenotype. In glioblastoma, chemotherapy-induced HIF1α and HIF2α was found to mediate the dedifferentiation of non-stem glioblastoma cells to CSCs, as marked by the expression of CD133, CD15, or SOX2 [203]. In bladder cancer, HIF1α has been shown to drive CD24 expression, which is a CSC marker, by binding to a functional HRE in the CD24 promoter [204]. These examples illustrate how hypoxia can drive CSC enrichment, thus potentially increasing the number of DTCs that metastasize and survive at distant sites, eventually growing into clinically significant lesions.

Study design and aims

While HIF signaling and the cellular responses it triggers are well characterized, questions remain as to the exact role of HIF signaling in tumor cell dissemination to bone and dormancy within the bone. Since tumoral hypoxia is a common feature of breast tumors and bone-disseminated tumor cells often experience hypoxia, further characterization of the contributions that HIF signaling plays both in the primary and distant site are essential. This dissertation will present findings that will address some of the current gaps in knowledge pertaining to HIF signaling, dormancy, and metastasis, with particular focus on HIF signaling in the primary tumor.

First, Chapter II will discuss currently available experimental models of breast cancer metastasis to bone, as well as the advantages and drawbacks of each, in order to highlight the

challenges of accurately modeling and studying bone metastasis and dormancy. Chapter III will detail the research methods used.

While LIFR expression is known to promote dormancy in bone-disseminated breast cancer cells and its expression is down-regulated in hypoxia, the details of the cellular response to LIFR expression or down-regulation are not well characterized. Chapter IV will discuss the characterization of LIFR-regulated pathways and genes in an attempt to identify novel dormancy regulators.

HIF gene expression in breast cancer cells has been shown to drive tumor cell localization to bone and osteolysis in injection-based mouse models, but the effect that the HIF gene (HIF1α, HIF2α, and VHL) expression in primary breast tumors has on organotropic dissemination patterns has not been investigated in a physiologically relevant spontaneous model of breast cancer. Chapter V will present our findings from the study of Hif1α, Hif2α, and Vhl knockout spontaneous mammary carcinoma mouse strains in order to investigate their contributions to bone dissemination. Finally, Chapter VI will discuss implication of future directions of this work.

CHAPTER II

MOUSE MODELS OF BONE METASTASIS

Overview

Metastasis is a complex, multistep, multi-organ process, making it challenging to study, and necessitating the use of animal models in many instances. The intricate mix of diverse cell types and niches present in the bone in particular, along with the unique architecture of trabecular bone, make it extremely challenging to model *in vitro*. Invasion into underlying tissues in the breast and intravasation, the earliest steps in the metastatic cascade, are best studied with the use of genetically engineered mouse models or orthotopic injection models. Later events, like extravasation following tumor cell circulation survival in the blood, and eventual colonization of the bone marrow, can be modeled with a wider range of models such as injection-based models in which the tumor cells are introduced directly into the bloodstream. Direct interactions between tumor cells and cells of the intact bone microenvironment are best modeled by intratibial or intrafemoral injections. Thus, the stage of the metastatic cascade being investigated will determine the most suitable model for the proposed studies.

Another aspect of the bone that makes it difficult of model *in vitro* is that it is constantly undergoing dynamic cycles of bone turnover. Bone-forming osteoblasts and bone-resorbing osteoclasts live on the surface of the bone, where their activity is tightly coupled and balanced to remove old or damaged bone and replace it with new bone matrix through the bone remodeling process [205]. This cycle of bone turnover is also deeply intertwined with the process of bone colonization by tumor cells, where the presence of breast cancer cells can disrupt physiological bone remodeling signals to promote bone destruction [144].

There are ways to model parts of this bone turnover process *in vitro*. Osteoclasts can be differentiated from precursor cells in culture using macrophage colony-stimulating factor (M-CSF) and RANKL [206], which can then be co-cultured on mineralized substrates like dentin (elephant ivory) and the extent of substrate resorption can be quantified [207]. While these resorption assays are helpful in investigating some relationships between cancer cells and bone resident cells, the mineralized matrix does not closely resemble the intricate structure of trabecular bone. Since bone architecture parameters like curvature and pore size have been

shown to affect how tumor cells and bone-resident cells behave [208, 209], these assays may not completely capture how tumor cells behave *in vivo*. To better model the bone microenvironment *in vitro*, several groups have developed bone-mimicking 3D scaffolds that recapitulate the bone microarchitecture and mineral composition [210-212]. These scaffolds can even be cultured in bioreactors that allow for perfusion flow and mechanical loading to better simulate a physiological bone microenvironment [213-217]. Mesenchymal stem cells, which have the ability to differentiate into osteoblasts, and monocytes, which can differentiate into osteoclasts, have successfully been cultured on 3D scaffolds [210, 218].

Other tissue-engineered bone environments have also been developed, such as humanized ossicles, which more fully capture the human bone marrow microenvironment. Ossicles are small extraskeletal bone compartments that are grown subcutaneously in mice through the injection of a mix of extracellular matrix factors and bone marrow-derived MSCs [219, 220]. Human hematopoietic cells can then be injected directly into the ossicle or delivered intravenously to generate a humanized bone marrow space within the ossicle. The use of ossicle models is still limited, likely owing to the technically challenging process involved in the successful generation of the ossicles. Over time, however, ossicle-based models may become more common in the breast cancer field and become a powerful tool to study both bone colonization and metastatic homing to bone, since they can be easily manipulated and imaged.

While these models are powerful tools and will become increasingly sophisticated over time (e.g. prolonged co-culture of multiple cell lineages in the bioreactor models), an *in vivo* system is still needed to fully capture the complex series of events that lead to the homing, establishment, and growth of disseminated tumor cells in the bone.

Bone metastasis in genetically engineered spontaneous tumor models

Genetically engineered mouse models (GEMMs) have been adapted for breast tumor studies by employing promoter-specific transgene expression to drive tumor formation. These models, in which mice spontaneously develop multifocal mammary tumors, are particularly relevant to the study of tumor formation, progression, and lung metastasis [221], but have not been readily adapted for bone metastasis. This is mainly due to the lack of robust bone metastasis formation in these models. While disseminated tumor cells are detectable in bone, the mice rarely form overt bone metastases [2, 222]. This may be in part due to the etiology of the model, but

typically mice succumb to lung metastases or the tumors grow to a size that requires ethical euthanasia before robust bone metastases are able to form. Thus, this model is useful for the study of early dissemination and mechanisms of outgrowth in bone, but not in the treatment of established bone metastases. A secondary issue is the ability to reliably detect disseminated tumor cells in the bone, owing to the lack of overt bone metastases. While crosses with reporter mice have been established [223], the breeding required for these mice is somewhat laborious since genes that drive tumor formation may also interfere with lactation [224], meaning that female breeders cannot carry the transgene. This breeding becomes even more complicated if additional genetic manipulations are desired, such as conditional knockout of a secondary gene.

In the absence of a reporter, highly sensitive tumor detection techniques are required. To detect disseminated tumor cells in the bone marrow, positive- or negative-selection strategies are often used to enrich for disseminated tumor cells. Negative-selection strategies commonly employ a CD45-based depletion technique to remove most bone marrow cells and thus enrich the proportion of tumor cells in the remaining population. This strategy, however, carries the risk of accidentally removing some tumor cells during the depletion step [225]. Positive-selection strategies, on the other hand, use ferromagnetically-conjugated antibodies against a tumor-specific marker, often epithelial cell adhesion molecule (EpCAM), to specifically collect tumor cells out of the bone marrow mix. A major limitation of this approach is that some tumor cells downregulate markers like EpCAM during the process of epithelial-to-mesenchymal transition (EMT) [226]. Thus, positive-selection likely leaves behind many tumor cells that do not express the selection marker. The recovery of tumor cells can be improved, however, by the use of a second selection marker. While selection-free methods do not have the advantage of enriching tumor cells from the bone marrow sample, they also minimize the risk of losing tumor cells during the selection process. Selection-free flow cytometry or bone marrow smear strategies are commonly used to identify disseminated tumor cells based on tumor markers like EpCAM or cytokeratin and have been used to detect early metastatic cells in PyMT transgenic mice [2]. In these strategies, tumor cells are often detected by staining with an antibody against a tumor-specific marker in addition to DAPI (to identify nuclei) and CD45 (to identify white blood cells). Technical advancements in recent years have allowed automated detection of candidate tumor cells (tumor-marker+/DAPI+/CD45-), which can then be reviewed, validated, and quantified [225].

One of the most commonly used spontaneous mammary carcinoma models is the MMTV-PyMT model [224, 227]. This mouse strain contains the polyoma middle T (PyMT) antigen, which drives tumor formation by interacting with a number of Src family members [228-232], as well as phosphatidylinositol-4,5-bisphosphate 3-kinase (PI3K) [233, 234]. The expression of the PyMT transgene is restricted to the mammary epithelial cells, as it is driven in response to the mouse mammary tumor virus long terminal repeats (MMTV-LTR). The MMTV-LTR promoter is induced in response to progesterone and dihydrotestosterone [235], and is mainly activated in mammary epithelial cells, but can also be active in some off-target tissues such as the salivary glands and lung [224]. Since the PyMT transgene is expressed in all mammary epithelial cells, this transgene will drive tumor formation in any or all of the 10 mammary glands. Thus, MMTV-PyMT mice vary in the number and size of tumors that are formed. Tumors are first palpable around 7-13 weeks of age depending on the background strain of the mouse [227]. MMTV-PyMT mouse are now available on the FVB/N or C57Bl/6 backgrounds, where the C57Bl/6 mice display a longer latent phase before tumors are palpable and an extended disease course [227]. While the timeline of tumor development and progression is obviously condensed in the MMTV-PyMT mice compared to human disease, the different stages of tumor development, from premalignant to malignant, are well captured and comparable to the stages of disease progression in human patients [236]. One of the limitations of this model is that while MMTV-PyMT mice exhibit metastatic dissemination to the lung [224], they do not form overt bone metastases. However, MMTV-PyMT have been instrumental in refining our understanding of metastasis and how tumor cells can disseminate to distant sites at much earlier time points than previously assumed. MMTV-PyMT mice had cytokeratin-positive (CK+) tumor cells detected in the bone marrow starting at 4-6 weeks of age, when only atypical ductal hyperplasia (ADH) or ductal carcinoma in situ (DCIS) was found in the mammary gland [2].

Another closely related model of spontaneous mammary carcinoma is the MMTV-Neu model [237, 238]. Neu is the name for the rodent homolog of human epidermal growth factor receptor 2 (HER2 or ERBB2) and drives carcinogenesis through activation of the PI3K/Akt pathway [239]. Like the MMTV-PyMT model, the expression of Neu is mostly restricted to the mammary epithelial cells since it is driven from the MMTV-LTR promoter. MMTV-Neu tumors are also known to faithfully recapitulate the course of human disease [240]. One of the advantages of the MMTV-Neu model is that the transgene driving carcinogenesis is the same

gene that is amplified in many human patients. Similar to the MMTV-PyMT model, MMTV-Neu mice have been used to study early dissemination and showed that CK+ and HER2+ bone-disseminated tumor cells were detectable in mice as young as 4-9 weeks old when only ADH was detectable in the mammary gland [2].

While these models have not been commonly used to study bone metastasis due to the low levels of bone dissemination, these studies demonstrate that sensitive detection modalities can be leveraged to distinguish tumor cells from bone marrow cells. Thus, the adoption of sensitive tumor cell detection techniques will allow researchers to leverage the benefits of these spontaneous tumor models. One of the advantages of spontaneous genetic models is that tumors grow in a more physiologically relevant manner compared to injection-based models where a mouse is inoculated with a bolus of tumor cells. Thus, these genetic models may be useful in studying the impact of specific genes on metastasis, and especially in studying what factors influence the timeline of metastasis. Spontaneous models, however, also have limitations and are not the most appropriate model in many studies. For example, spontaneous models are likely not the ideal choice for studies that require surgical removal of the primary tumors to allow metastatic cells to be tracked over extended time periods. The multifocal primary tumor formation makes it ethically challenging to perform tumor removal survival surgeries and could lead to extensive surgical intervention and inflammation, which could confound the data. Thus, the advantages and disadvantages of each model must be thoughtfully considered to ensure selection of the optimal model.

Injection models of bone metastasis

While genetically engineered spontaneous tumor models can model each step of the metastatic cascade, they also present several challenges. First, the age at tumor onset and the rate of tumor growth can be quite variable, even within the same genotype, introducing potential age-related variables into bone architecture and tumor dissemination parameters. Second, final tumor mass and volume can also vary widely, which can complicate downstream analysis of metastatic tumor burden. Third, due to the inherent variability in the model, some studies may require relatively large samples sizes, which can be costly, particularly if complex crosses are involved. This also introduces the possibility of genetic drift between the first and last individuals of each

group to be collected, as their birth (and collection) dates could be very far apart from one another.

To address some of these technical challenges, selecting a tumor cell injection-based model may be more appropriate in many settings. While most of these models do not capture the full metastatic cascade, especially early tumor development, they have the advantage of being able to specifically focus on certain steps of the cascade (Fig. 3) and minimize some variables. For example, injection-based models allow you to inject the same number of tumor cells into each mouse, standardize collection time, and eliminate possible off-target effects of genetic manipulation.

Orthotopic injection. Orthotopic injections, or mammary fat pad injections in the case of breast cancer, model all the steps in the metastatic cascade, and are therefore particularly useful when studying how tumor cells disseminate from the primary tumor site to the bone marrow. There are multiple ways in which orthotopic injections can be performed. The simplest method involves injecting cells into the mammary fat pad using visual landmarks such as the nipple and injecting through the skin without creating an incision [241]. This method produces the least amount of inflammation, but it can be challenging to confirm whether the tumor cells were properly injected into the mammary gland, or if the injection location was too shallow or too deep. The second method involves making a surgical incision to expose the mammary gland, although the size of the incision may vary [242, 243]. The mammary gland is identified and stabilized with forceps and the cells are injected directly into the fat pad before the incision is sealed with staples or tissue glue. This method ensures that the tumor cells are injected directly into the mammary fat pad, rather than surrounding tissues; however, this approach produces significantly more inflammation and is considered a surgical procedure. The potential impact of surgical inflammation may profoundly impact tumor cell growth, given that it was recently reported that inflammation due to surgery leads to tumor recurrence in mice [244]. Whichever protocol is selected, mice will need to be placed under anesthesia for the duration of the injection procedure.

Another variable for this injection model is whether the cells are suspended in PBS or a compound such as Matrigel, which polymerizes in the fat pad and prevents tumor cells leakage following injection [241, 242]. Matrigel may not be suitable in all situations, however, as many Matrigel preparations contain growth factors that may influence experimental outcomes. Growth

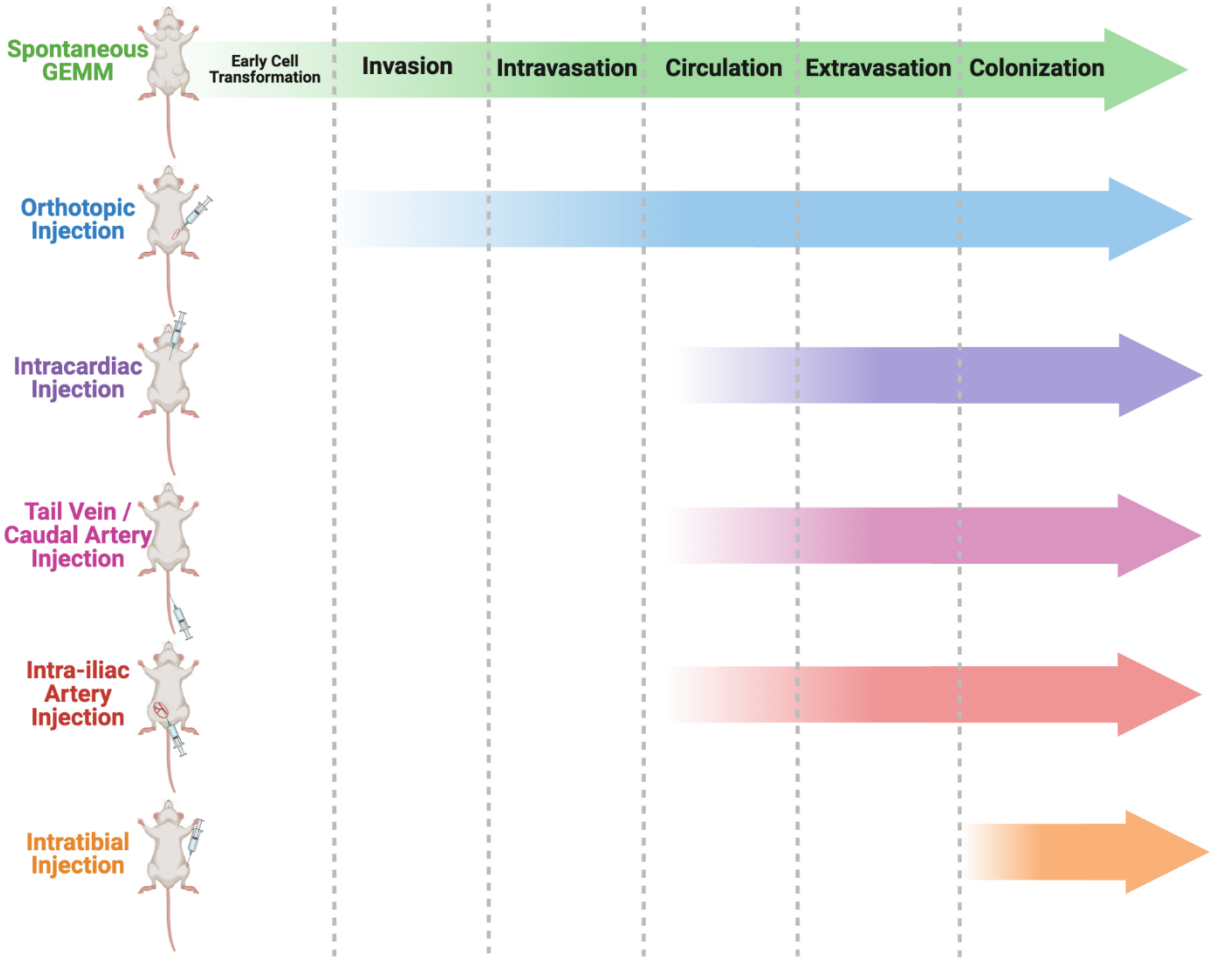

Figure 3. Genetically engineered mouse models (GEMM) model all stages of the metastatic cascade, as well as early steps of mammary cell transformation into cancerous cells. Orthotopic injections also model all stages of the metastatic cascade starting with invasion into surrounding tissues. Intracardiac, tail vein, caudal artery, and intra-iliac artery injections model later stages of metastasis, as tumor cells are injected directly into the circulation. Intratibial injections that place tumor cells directly in the bone marrow will model only the final colonization step.

factor-depleted preparations are also available, however, and may be preferable option for some application. Additionally, since it forms an extracellular matrix-like environment, Matrigel can activate integrin signaling in tumor cells. Matrigel has been shown to enhance tumor growth and metastatic potential [242, 245, 246] and may thus be beneficial in achieving more robust dissemination when using low-metastatic potential cell lines.

Intracardiac injection. Intracardiac injection in one of the most commonly employed models to study bone metastasis and involves the direct inoculation of tumor cells into the left ventricle of the heart, which bypasses the lungs and introduces the cells directly into the systemic circulation. Thus, this method cannot capture the early stages of metastasis (e.g. invasion and intravasation), but appropriately models hematogenous spread throughout the body and later extravasation and colonization of the bone. Since the tumor cells are injected into the bloodstream in this model, it is possible that metastatic lesions will arise in tissues other than the bone, such as the lungs or brain [247, 248]; however, this can be mitigated through the use of the bone-metastatic clones discussed above, which also ensures a minimal number of cells are inoculated. The density of cells that are injected must be kept relatively low to avoid clumping and embolism.

To inject cells directly into the left cardiac ventricle, the heart is located in reference to positional markers on the sternum. The needle is then inserted in the intercostal space (between two ribs) while holding the needle in a steady vertical position. To confirm proper placement, the syringe is closely inspected to determine whether the pulse from the heart is detectable in the cell suspension liquid. The cells are then slowly injected into the ventricle, and the syringe removed. Immediately following injection, pressure is applied on the injection site to prevent cells or blood leaking out of the heart, which may result in the formation of chest tumors that can be mistaken as lung metastases [249]. Of note, it is virtually impossible to distinguish a leaky intracardiac injection from lung metastases, and thus any tumor identified in the lung following this procedure should be analyzed with caution, since the tumors are most likely the result of a leaked injection. Intracardiac injections are a relatively quick and minor procedure given that it is a simple injection; however, given the delicacy of the injection, approximately 10% of the mice will not recover from the procedure. Mice must be carefully monitored post-injection to ensure they recover from the procedure and anesthesia.

Tail-vein and caudal artery injections. Like intracardiac injections, tail-vein injections model hematogenous spread and later steps of the metastatic cascade, since tumor cells are injected directly into the bloodstream through one of the lateral tail-veins [250]. Tail-vein injections are commonly used to model pulmonary metastasis, since the inoculated tumor cells will reach the lungs when the venous blood is pumped from the heart to be reoxygenated. While this injection type is rarely used to model metastasis to the bone, a relatively small number of tumor cells will disseminate to the bone marrow following tail-vein injection [247].

Caudal artery injections are similar to lateral tail-vein injections in that they are directly inoculated into one of the blood vessels in the tail. Injection into the caudal artery, however, delivers tumor cells to the hindlimb bone marrow far more efficiently than tail-vein or even intracardiac injection [251]. Caudal artery injections are also less technically challenging to perform than intracardiac injections and rarely cause acute post-injection mouse mortality. Furthermore, larger cell numbers can be injected using the caudal artery model without risking increased mouse mortality, meaning that higher cell numbers can be injected to achieve more substantial tumor burden in the bone.

Both tail-vein and caudal artery injections have the benefit of being minimally invasive and the mice do not need to be placed under anesthesia. The injection procedure can still be stressful for the mice, however, as they must be placed in a restraining device so that the tail can immobilized to safely perform the injection.

***Intra-iliac artery injection*.** Though more invasive than some other injection techniques, the intra-iliac artery injection method also has some distinct advantages such as efficient delivery of tumor cells to the hindlimb bone marrow [252]. To inject cells directly into the intra-iliac artery a small incision (about 1cm in length) is made between the 4^{th} and 5^{th} mammary glands to expose the iliac vessels and nerves. The vessels are then carefully isolated with forceps from the nerves and surrounding connective tissue. A silk suture is then threaded underneath these vessels to keep them separated from the surrounding structures. Tumor cells are then inserted into the artery. After removing the forceps and suture from the area, a cotton swab is pressed down on the injection site to stop bleeding prior to closure of the incision site with tissue glue.

This injection route can be particularly useful in combination with less aggressive cell lines that would not result in readily detectable tumor burden in the bone using any of the

previously discussed models. Indeed, this method was originally published using the MCF7 model, in which it was shown that MCF7 cells seeded into the bone marrow more efficiently following intra-iliac inoculation compared to intracardiac inoculation [253]. The disadvantage of this procedure is that it is one of the most technically challenging types of injections, since surgery must be performed to expose the artery, with the mice being under anesthesia for a substantial amount of time following inoculation. This requires extensive training to perform properly so as not to nick the artery and cause hemorrhage.

Intra-iliac artery injections have been used to deliver breast cancer cells to the bone to study microenvironmental niche factors that promote bone marrow colonization, such as interactions between tumor cells and osteogenic niche resident cells that are mediated by heterotypic adherens junctions [253]. Other functions of the osteogenic niche, such as its ability to help cancer cells increase intracellular calcium and thus promote cancer cell proliferation [254], and epigenetically reprogram metastatic tumor cells to reduce ER expression and activity to promote therapeutic resistance [255], have also been determined by studies employing the intra-iliac artery model.

***Intratibial injection*.** The intratibial model differs significantly from the other models that are presented in this review, since intratibial injections are not used to model or study metastasis. Since tumor cells are injected directly into the tibial marrow space, this technique is useful in studying the colonization and proliferation capabilities of cells separately from their ability to disseminate to the bone. For example, an intratibial injection model was used to study the ability of a novel Gli inhibitor (GANT-58) to inhibit breast cancer cell colonization of the bone marrow [256]. Intratibial injections were also employed to study the effect that bone stromal cell-derived hyaluronan has on bone metastatic breast cancer cells and found that hyaluronan-rich microenvironments stimulated tumor cell growth and osteolysis [257]. Thus, there are times in which it is appropriate to use the intratibial model, depending on the research question being asked, but it should be considered a post-metastasis model.

Intratibial injections are performed by inoculating tumor cells into the marrow space through the growth plate at the proximal end of the tibia [249]. The mouse's leg is held such that the knee is in a bent position, with the joint exposed. The needle is then inserted under the patella, through the patellar ligament. Firm pressure and a slight drilling motion of the needle

will help to achieve full penetration into the marrow space. A similar technique can be used to perform intrafemoral injections if desired, with the main difference being that the needle is inserted into the distal end of the femur rather than the proximal tibia [258]. While this is not a surgical procedure, the mice must be placed under anesthesia to safely perform the injection. Additionally, since the needle directly punctures the bone, damage to the bone and inflammation can occur at the injection site, which may interfere with later analysis [259].

Intratibial injections can also be useful for studies where the exact location of tumor cells within the bone must be known. Intratibial injections may be ideal for studies comparing imaging modalities, or for longitudinal tumor growth studies, where the same tumor lesion is imaged repeatedly. For example, one study investigated the utility of *in vivo* micro computed tomography (microCT) in tracking tumor-induced bone destruction over time [260]. Mice were inoculated via intratibial injection with MDA-MB-231 cells expressing GFP and subjected to *in vivo* microCT and fluorescent imaging over the course of 4 weeks to monitor bone destruction. This study established the utility of *in vivo* microCT in longitudinal bone lesion monitoring and found that the microCT imaging itself did not interfere with tumor cell growth.

Cell lines commonly used for injection models of bone metastasis

The second general category of mouse models that are used to study breast cancer metastasis to bone are injection-based models. Many cell lines are used for these models, and these can generally be grouped into those with "low bone metastatic potential" and "high bone metastatic potential" (Table 1). Cells with low bone metastatic potential do not aggressively metastasize to bone and either do not form overt metastases or take a longer time for metastatic lesions to become established [195]. These cells model a slower progression of bone metastasis, where tumor cells have disseminated, but have not yet induced osteolytic bone destruction, and some of these cell lines may also model dormancy or a latent tumor phase in bone. The utility of these cell lines has previously been limited due to the technical challenge of detecting low level bone tumor burden. Recent advancements in sensitive flow cytometry and quantitative PCR (qPCR) based detection methods that complement classical immunostaining and histology-based detection methods have increased the utility of these cell lines [261], without introducing fluorescent reporters that have the potential to elicit an immune response *in vivo* [262-266].

Table 1. Bone metastatic capability and hormone receptor status of commonly used breast cancer cell lines.

Cell Line	Species	Bone metastatic potential	ERα Status	PR Status	HER2 Amplification	References
MCF7	Human	low	+	+	-	[267, 268]
T47D	Human	low	+	+	-	[268]
SUM159	Human	low	-	-	-	[269, 270]
D2.0R	Mouse	low	+	?	+	[271]
MDA-MB-231	Human	high	-	-	-	[267, 268]
4T1	Mouse	high	-	-	-	[272]
E0771	Mouse	high	+/-	+/-	+/-	[273, 274]
SSM2/SSM3	Mouse	high	+	+	-	[275]

Human ER+ cell lines. MCF7 [267, 276-279] and T47D [280] cells are estrogen receptor positive (ER+) human breast cancer cells that are used widely in breast cancer research both *in vitro* and *in vivo*. MCF7 cells in particular have been reported to be non-proliferative in bone and do not robustly induce osteolysis [195, 281, 282]. MCF7 cells have been shown to be Ki-67-negative in the majority of metastatic bone lesions [195], and MCF7 cells grown in a 3D environment *in vitro* are reported to frequently express nuclear p27 [281], suggesting these cells enter a state of quiescence *in vivo*. Since some proportion of the cells maintain proliferative markers like Ki-67 or low levels of p27, these studies seem to also support the tumor mass dormancy model, in which micrometastases are maintained in a dormant state due to the balance of proliferation and apoptosis. T47D cells have been shown to enter a non-proliferative (EdU-negative) state when grown in 3D bone-mimetic hydrogels and persist as viable cells for up to 40 days [283], suggesting the cells interacting with bone-like extracellular components triggers a reversible quiescent state. It is important to remember that since these are human cell lines that must be injected into immune-deficient mice, the immune system's role in inhibiting metastatic outgrowth and maintaining tumor mass dormancy cannot be studied *in vivo* using these lines. It is important to note, however, that the behavior of the MCF7 cells *in vivo* can be highly variable and have been reported to extensively colonize the bone *in vivo* on some occasions [284].

Because these cell lines are ER+, they require exogenous estradiol supplementation in order to grow in the orthotopic site (mammary fat pad) or the bone [285-288]. Estradiol supplementation dramatically increases bone volume, substantially altering the normal architecture of the bone and disrupting the marrow space [261, 289, 290]. Thus, while the use of estradiol supplementation supports tumor growth and metastasis in the MCF7 and T47D models, the information that can be gathered about how the tumor cells interact with other bone-resident cell types is limited. Of note, estradiol supplementation is not required for tumor cells to disseminate to bone; MCF7 cells are detectable in bone following intracardiac inoculation independent of estradiol implantation [253, 261, 284], but tumor burden is increased with estradiol [261].

Importantly, the development of sensitive detection methods has now made it more feasible to use these cells without estradiol supplementation. CD298 is a human specific cell marker that can be used to sensitively differentiate human cells from mouse host cells that do not express CD298 [291]. Flow cytometric analysis of bone marrow from mice inoculated with

MCF7 cells by intracardiac injection detected CD298+ cells in 8 of the 10 mice tested [261]. Since MCF7 cells are human cells, human-specific house-keeping genes can also be used to quantify tumor burden using qPCR. Human beta-2-microglobulin (*B2M*) was detectable in whole bone homogenates in 5 out of 10 mice that were MCF7-inoculated without estradiol supplementation, and human hypoxanthine phosphoribosyltransferase 1 (*HPRT1*) was detectable in 4 out of 10 mice [261]. Notably tumor cells were not identifiable in the bones of these mice based on histological analyses performed by a certified veterinary pathologist [261], demonstrating the utility of these sensitive flow cytometry and qPCR techniques. These new tumor cell detection techniques were similarly effective in detecting bone metastatic SUM159 cells, an ER-negative human breast cell lines with low metastatic potential [194, 292, 293]. Though SUM159 cells are used less commonly that MCF7 or T47D cells, they are an important tool to be able to model the behavior of a wider range of breast cancer subtypes. Collectively, since the ER+ human breast cancer cell lines do not robustly colonize the bone, these models are suitable for the study of the early phases of tumor dissemination to bone, which precedes osteolytic bone destruction. It is important to highlight this when using these models, since the typical outcomes of osteolysis are not always the best readout for tumor presence or activity in the bone in these models.

Our lab established a novel bone metastatic variant of MCF7 cells, termed MCF7b cells [294]. These cells were isolated from a mouse that developed spontaneous overt bone metastases approximately 6 months after orthotopic injection of MCF7 cells. MCF7 and MCF7b cells are equally proliferative *in vitro*, have the same epithelial cell morphology, and similar base line expression of AKT, ERK, STAT3, and ERα measured by western blot or reverse phase protein array (RPPA) analysis. While MCF7b cells do not grow as robustly in the orthotopic site, they are more invasive and metastasize more robustly to the bone. These cells are thus a powerful tool to help us understand drivers of bone metastasis.

Mouse ER+ cell lines. While MCF7, T47D, and SUM159 cells have the advantage of modeling how human cells behave *in vivo*, they require the use of immune compromised mice, often athymic nude mice, to prevent host rejection of the inoculated cells [295]. Mouse cell lines, in contrast, may be injected into immune competent mice, but it may also be more challenging to identify disseminated tumor cells in these models since they lack the specificity of human-

specific markers. Thus, the use of mouse mammary carcinoma lines allows researchers to study the interaction of tumor cells with the full array of immune cells and to study how a fully functioning immune system affects metastasis and the growth of tumor cells in the bone. While the use of less aggressive mouse lines has been limited by the technical difficulty of differentiating between mouse tumor cells and host bone marrow cells, more sensitive detection strategies gave increased the utility of these cell lines. One example is the D2.0R line, an ER+ mouse mammary carcinoma cell line with low metastatic potential, meaning lung or bone disseminated cells tend to lie dormant and not develop into proliferative lesions [281, 296]. Non-proliferative D2.0R cells express high levels of p16 and p27 when grown in 3D [281], suggesting that these cells likely enter a similar state of cellular quiescence *in vivo*. Since these tumor cells cannot be distinguished from host bone marrow using human- or mouse-specific markers, the tumor cells must be identified based on epithelial markers that they express, since these markers are not expressed by bone marrow cells. While fluorescence reporters are generally a viable option, tagging the cells with exogenously expressed fluorescent reporters may elicit a host immune response against the reporter protein [262-266], thus eliminating the tumor cells. Cytokeratin 18 (*Krt18*) has been identified as a marker of D2.0R tumor cells and qPCR amplification of *Krt18* has detected tumor burden in bone that was not detectable using standard histological analysis [261]. D2.0R cells have proved to be a useful tool in studying tumor dormancy [281, 297, 298], and may become more commonly used in animal models of bone metastasis with the adoption of sensitive detection techniques such as these.

In recent years, two new ER+, progesterone receptor- positive (PR+) mouse mammary carcinoma cell lines, SSM2 and SSM3 [299], were developed that overcome many of the challenges that researchers have encountered when trying to model hormone receptor positive disease. SSM2 and SSM3 are both derived from spontaneous mammary tumors that arose in $STAT1^{-/-}$ 129S6/SvEv-strain female mice [275]. Roughly 65% of $STAT1^{-/-}$ mice are reported to develop mammary tumors, but the late median onset (23 months) [275] makes this strain non-ideal for use as a model of spontaneous breast cancer. The SSM2 and SSM3 cells derived from this model, however, develop bone metastases in the tibia, spine, and ribs after intracardiac injection detectable by x-ray, *in vivo* CT, and histology, and proliferate in the bone following intratibial injection [299]. A notable advantage of the SSM2 and SSM3 cells is that they do not require estradiol supplementation to grow in the primary site or the bone, unlike MCF7 or T47D

cells, bypassing estradiol-mediated effects on the bone. While they do not require exogenous estradiol, their growth in the primary site is still dependent upon circulating estrogen, since SSM2 and SSM3 cells do not grow in ovariectomized mice following orthotopic inoculation [275]. Surprisingly, SSM2 cells, but not SSM3 cells, are able to grow independently of estrogen in the bone while maintaining ER/PR expression, as they were found to grow in ovariectomized mice after intratibial injection [299], making these cells a suitable model to study the role of the bone microenvironment in hormone-independent growth of tumor cells. This observation also indicates that some tumor cells may have differing levels of estrogen dependence depending on the anatomical site and surrounding microenvironment. Furthermore, these cell lines represent a clinically relevant ER+/PR+ mammary tumor model, since patients with ER+ disease commonly have low STAT1 levels in their tumors [275]. STAT1 expression, however, has been linked to both favorable and poor outcomes in patients [300-303] and thus its role in breast cancer remains unclear.

Human ER- cell lines. In contrast to the less aggressive cell lines that are highly variable in their frequency and extent of bone dissemination, there are a number of aggressive cell lines commonly used in breast cancer research due to their ability to consistently metastasize to the bone in a short timeframe. These highly metastatic lines robustly induce osteolysis that can be easily detected with radiographic imaging to provide a readout of tumor-induced osteolysis [249]. The most common human breast cancer cell line in this category is the ER-negative MDA-MB-231 cell line [267, 304]. MDA-MB-231 cells form overt bone lesions that are detectable by radiography in roughly 30% of mice 10-12 weeks after intracardiac inoculation with 100,000 cells [305].

The robust bone metastatic phenotype of MDA-MB-231 cells has spurred the development of many different sub-clones with differential bone metastatic capabilities. Dr. Joan Massagué's group, for example, has developed distinct sub-clones of MDA-MB-231 cells through *in vitro* single-cell cloning of individual parental MDA-MB-231 cells [305]. These sub-clones are denoted SCPs (single cell progenies) and have a variety of metastatic tropisms [306]. Some clones, like SCP46, aggressively colonize the bone following intracardiac injection but do not readily colonize the lung after tail-vein inoculation, while other clones, such as SCP3, exhibit moderate bone metastatic capabilities but colonize the lung and adrenal glands more

aggressively. Another common method that is used to generate highly bone metastatic sub-clones is to perform *in vivo* selection, where mice are inoculated via intracardiac injection with parental MDA-MB-231 cells and resulting bone lesions are expanded *in vitro* after flushing the bone marrow from hind limbs. This process can be repeated multiple times by inoculating mice with the cells generated from the previous round of selection to generate increasingly bone-tropic cells. Several groups have developed bone-tropic MDA-MB-231 sub-clones using this technique. The Massagué group has developed sub-clones denoted 1833 and 2287, which were generated through one cycle of *in vivo* selection [305]. These sub-clones form large osteolytic lesions in roughly 90% of inoculated mice within 5-7 weeks after intracardiac injection. The bone metastatic sub-clones developed by the Clézardin group are denoted MDA-MB-231/B02 and are the result of six successive *in vivo* passages through bone [307]. Yoneda *et al.* developed the MDA-231BO sub-clone through 11 *in vivo* passages to achieve a cell line that exclusively metastasizes to the bone following intracardiac injection [308]. In addition to these sub-clones, many labs have established their own bone metastatic lines. Comparison of weakly and highly bone metastatic sub-clones of MDA-MB-231 cells, or comparison of sub-clones with different organ-specific tropisms, has proven effective in defining transcriptomic signatures associated with the formation of osteolytic bone metastases [305, 306].

Mouse ER- cell lines. In addition to human cell lines, there are several mouse mammary carcinoma lines that similarly metastasize to the bone in a relatively short timeframe. Two commonly used ER-negative mouse lines are the 4T1 [309] and E0771 cells [251, 273, 274, 310]. Bone metastatic clones of both of these lines have been developed [311, 312], aiding in the identification of genetic or transcriptomic factors that may regulate bone metastasis. 4T1 cells in particular are very widely used and have facilitated many pivotal discoveries. In recent years, parathyroid hormone (PTH) administration has been shown to prevent metastasis of orthotopically injected 4T1 cells [313], oncostatin M (OSM) was found to be necessary for bone metastasis of orthotopically injected 4T1.2 cells (a single cell-derived subclone of 4T1 cells [311]) [314], and a bone-metastatic clone of 4T1 cells was used to study systemic and bone-marrow compartment specific immune changes that accompany bone metastasis [312]. A bone-metastatic clone of E0771 cells (E0771/Bone) that exhibits breast cancer stem-like cell surface markers $CD24^{-}/CD44^{+}$ was recently established by sequential *in vivo* selection, suggesting that

stem-like cells may be integral in tumor colonization and the establishment of bone metastases [315].

Conclusions

Since the bone is the most common site of metastasis for breast cancer cells, various models have been developed to mimic the complex process that cells must undergo to disseminate to, and colonize, the bone. Each of these models has its own advantages and drawbacks, and the combined use of these models across the field continues to shed light on the molecular mediators of bone metastasis.

One notable issue that is shared by most of the models discussed in this review is that they are primarily designed to study metastasis to the long bones, and the hindlimbs in particular. While metastatic lesions in the long bones such as the femur or humorous are somewhat common in human patients, lesions commonly develop in the pelvis, vertebrae, ribs, and other sites. Due to the difficulty in accessing these sites for analysis, their more complicated anatomical structure, and lack of a large marrow space, techniques to analyze these sites in mouse models of bone metastasis are less developed. Further improvements and widespread adoption of new techniques that will allow for better modeling and analysis of additional axial and appendicular skeletal sites will continue to push the bone metastasis field forward.

Additionally, the cell lines and detection techniques that are currently available to study ER+ disease remain underdeveloped. The requirement for exogenous estrogen supplementation to achieve robust bone metastasis using human ER+ cell lines poses a significant obstacle in the study of this common breast cancer subtype. Development of novel cell lines or variants of existing cells lines such as MCF7 and T47D cells may propel new discoveries in the field.

CHAPTER III

MATERIALS AND METHODS

Cell culture and reagents

***Cells*.** Human MCF7 and MDA-MB-231 breast cancer cells and 4T1 mouse mammary carcinoma cells were obtained from ATCC. Human SUM159 breast cancer cells were a gift from the Rutgers Cancer Institute of New Jersey and were cultured in Ham's F12 medium supplemented with 5% FBS, 5μg/ml insulin and 1μg/ml hydrocortisone. Mouse mammary carcinoma cell lines D2A1 and D2.0R were a gift from J. Green at the National Cancer Institute. PyMT-derived tumor cells were established in R. Anderson's laboratory. Human MDA-MB-231b bone metastatic cells were established from the original bone clone made by the Mundy laboratory, and passaged in bone periodically to maintain bone metastatic phenotype [316, 317]. 4T1BM2 bone metastatic mouse mammary carcinoma cells [318] were a gift from N. Pouliot at the Peter MacCallum Cancer Centre. All cell lines, except SUM159 human breast cancer cells, were cultured in DMEM supplemented with 10% fetal bovine serum (FBS) and 1% penicillin/streptomycin (P/S). No cell lines used in this study were found in the database of commonly misidentified cell lines that is maintained by ICLAC and NCBI Biosample. All cells were regularly tested for mycoplasma contamination.

***shRNA*.** Parental MCF7 cells transduced with a non-silencing control (NSC) shRNA and LIFR shRNA#3 were previously generated [195]. Additional LIFR and COL14A1 knockdown lines were generated by transfection of GIPZ lentiviral vectors (Dharmacon, shLIFR#6: V3LHS_347496, shLIFR#8: V3LHS_347498, shCOL14A1#1: V2LHS_15868, shCOL14A1#2: V2LHS_15870, shCOL14A1#3: V3LHS_370361, shCOL14A1#4: V3LHS_370362) into 293T cells to produce lentivirus followed by transduction of MCF7 cells with virus and 5 μg/ml polybrene. All lentiviral transduced cells were selected with 1 μg/ml puromycin. All microscope images of cells were collected on an Olympus BX41 Microscope equipped with an Olympus DP71 camera using the 20X and 40X objectives.

RNA sequencing

RNA samples of MCF7 NSC and MCF7 shLIFR#3 cells (n = 3 independent replicates per group) were submitted to the Stanford Functional Genomics Facility. RNA samples were analyzed for RNA integrity using a Bioanalyzer (Eukaryote Total RNA Nano, Agilent) to ensure all samples had an RNA integrity number of between 8.3–10 (10 is highest quality possible) prior to sequencing on an Illumina NextSeq with coverage of approximately 40 million reads per sample. Vanderbilt Technologies for Advanced Genomics Analysis and Research Design (VANGARD) core at Vanderbilt University Medical Center performed sequence alignment and RNAseq bioinformatics analysis. The shLIFR RNAseq data has been deposited in the GEO database (accession number GSE174592). Gene network maps were generated using the STRING database (https://string-db.org).

Western blotting

Cells grown in a monolayer were rinsed with 1×PBS and harvested for protein in RIPA buffer supplemented with protease and phosphatase inhibitors (Roche). For cells grown in a collagen I matrix, 24,000 cells were suspended in a 3:1 mixture of complete growth media:collagen I (Corning), and plated in triplicate on a 24-well plate (200 µl/well). Plates were incubated for 30 min at room temperature to allow collagen to polymerize before incubation at 37 °C for 4 hours. 1 ml of complete growth media was then added and plates were incubated at 37 °C for 2 weeks, changing media every other day. To harvest cell, 1 ml collagenase type II (1 mg/ml, Worthington) was added to each well and plates were incubated at 37 °C for 10 min. Collagen in each well was then mechanically digested by pipetting up and down a few times and then incubated at 37 °C for an additional 10 min. Technical replicate wells were then pooled and diluted with 10 ml media. Cells were collected by centrifugation and washed with PBS. Cell pellet was then resuspended in 50 µl RIPA buffer supplemented with protease and phosphatase inhibitors (Roche) and incubated at 4 °C while mixing using a rotator. For both 2D and 3D growth conditions, RIPA cell lysates were further mechanically digested by expulsion through an insulin syringe. Protein concentration was determined by BCA assay (ThermoFisher) and 20 µg protein was loaded onto an SDS-PAGE gel in reducing conditions using standard techniques. Nitrocellulose membranes were probed with antibodies against LIFR (Santa Cruz Biotechnology, C-19, catalogue number sc-659, 1:1,000), pERK1/2 Thr202/Tyr204 (Cell

Signaling, catalogue number 9101, 1:1,000), ERK1/2 (Cell Signaling, catalogue number 9102,1:1,000), pAKT Ser473 (Cell Signaling, catalogue number 9271, 1:1,000), AKT (Cell Signaling, catalogue number 9272S, 1:1,000), pSTAT3 Tyr705 (Cell Signaling, catalogue number 9131, 1:1,000), STAT3 (Cell Signaling, catalogue number 9139, 1:1,000), vinculin (Millipore, catalogue number AB6039, 1:10,000), and calnexin (Abcam, catalogue number ab22595, 1:900). All western blots were quantified for relative density using ImageJ. In brief, blot images were converted to a histogram rendering for each lane and peaks were converted to the relative percentage for each blot. Proteins of interest were then normalized to the relative percentage of the loading control for the respective lane. Phosphorylated forms of proteins were first compared to the total protein level before normalizing to the loading control.

Real-time PCR

Cells were harvested in TRIzol (Life Technologies) and mouse samples (tumors, right lung lobes, brains, and intact right femora) were homogenized in 1 mL TRIzol, phenol-chloroform extracted, DNase digested (TURBO DNA-free Kit, Life Technologies), and cDNA synthesized (1ug RNA, iScript cDNA Synthesis Kit, Bio-Rad) per the manufacturer's instructions. Real-time PCR was performed using iTaq Universal SYBR Green Supermix (Bio-Rad) on a QuantStudio 5 (Thermo Fisher) with the following conditions: 2 min at 50 °C, 10 min at 95 °C, (15 s at 95 °C, 1 min at 60 °C) x 40 cycles followed by dissociation curve (15 s at 95 °C, 1 min at 60 °C, 15 s at 95 °C). For each biological replicate, three technical replicates were performed for each gene analyzed. Non-template controls were included as a negative control for each gene analyzed. Analysis was performed by normalizing the expression of the target gene to the average *B2m* or *Hmbs* expression within the same sample to determine ΔCt. The ΔCt was transformed ($2^{-\Delta Ct}$) and the average of the three technical replicates was calculated. The average $2^{-\Delta Ct}$ is presented as target gene "(*LIFR, etc.*): (*B2m* or *Hmbs*) mRNA" in the figures. Figures noted as "Relative (*LIFR, etc.*): *B2m* mRNA" or "Relative mRNA abundance" are normalized against the mRNA abundance in the NSC column.

Human primers for *B2M*, *LIFR*, *NOTCH1*, and *TGFB2* were previously published [195]. Mouse primers for *Pymt* [319] and *Hmbs* [320] were previously published. Primer sequences for *Pthlh* were kindly provided by Drs. Natalie Sims and T. John Martin at St. Vincent's Institute of Medical Research. Mouse primers for *B2m, Vegfa, Hif1α* exon 2, *Hif2α* exon 2, and *Vhl* exon 1

were designed using PrimerBlast (NCBI) against the mouse genome (Mus musculus) and validated by dissociation. Other primer sequences were obtained from the Massachusetts General Hospital (MGH) Primer Bank and validated by dissociation. Real-time PCR primer sequences are compiled in Tables 2 and 3.

The expression of a panel of metastasis-associated genes was quantified using the tumor metastasis (SAB Target List, M384) qPCR array plate (Bio-Rad). Each gene in the array was run in duplicate. Three representative Hif1α$^{f/f}$ and Hif1α$^{-/-}$ tumor homogenate RNA samples were selected base on their *Hif1α* expression. Analysis was performed by normalizing the expression of the target gene to the average *B2m* expression within the same sample to determine ΔCt. The ΔCt was transformed ($2^{-\Delta Ct}$) and the average of the two technical replicates was calculated. ΔCt values for each Hif1α$^{-/-}$ sample was then normalized against the average of the three Hif1α$^{f/f}$ samples to determine enrichment.

TCGA analysis

For COL14A1 analysis, The Cancer Genome Atlas (TCGA) [321] Breast Invasive Carcinoma dataset (Firehose Legacy dataset; http://www.cbioportal.org/study/summary?id=brca_tcga) was accessed on October 27, 2017. Patient survival data was downloaded and survival was analyzed using Graphpad Prism software based on mRNA downregulation.

For hypoxia signature analysis, TCGA Breast Invasive Carcinoma dataset was accessed on 16 November 2020, 17 November 2020, and 15 April 2021 to determine whether the hypoxia gene signature [322] from n=1,100 patients correlated with bone [305] and lung metastasis signatures [323]. Genes from the hypoxia, bone metastasis, and lung metastasis gene signatures were entered into the query gene field for cBioPortal separately. The mRNA expression (RNA Seq V2 RSEM) for each gene across all 1,100 patients was downloaded and saved in Excel format. For each gene in the three gene signatures, the gene expression provided by RNAseq was normalized to the median expression of that gene across all patients as previously published [324]. We next averaged the expression score for all of the genes in that signature for each individual patient. For the bone and lung metastasis signatures, an average gene signature score was calculated separately for the genes that were up or down in the gene signature. A log conversion was applied to the normalized, averaged gene signature expression scores. These

Table 2. Real-time PCR primer sequences for human genes.

Gene Name	Forward Primer Sequence	Reverse Primer Sequence
B2M	GAGTATGCCTGCCGTGTGAA	TGCGGCATCTTCAAACCTCC
CDH1	CGAGAGCTACACGTTCACGG	GGGTGTCGAGGGAAAAATAGG
CDH2	TCAGGCGTCTGTAGAGGCTT	ATGCACATCCTTCGATAAGACTG
COL3A1	GCCAAATATGTGTCTGTGACTCA	GGGCGAGTAGGAGCAGTTG
COL4A5	TGGACAGGATGGATTGCCAG	GGGGACCTCTTTCACCCTTAAAA
COL4A6	GGCTCTACTGGTTTATCGGGA	CCTTGAGTTCCATTACAGCCATC
COL6A1	ACACCGACTGCGCTATCAAG	CGGTCACCACAATCAGGTACTT
COL6A6	TCTATGGCCGATGTTGTGTTC	CTTCCCAGTTCGGGGAGAA
COL14A1	ATGCCAGACCAGAATTACACAG	ACCATCGACCAGGATTACAATGT
COL23A1	TCCATCCGAATGTGTCTGCC	GTAGCCATCTCGTCCTGATTG
CTNNB1	AAAGCGGCTGTTAGTCACTGG	CGAGTCATTGCATACTGTCCAT
DMD	TCAACAGGATTTTGTGACCAGC	GCAACTTCACCCAACTGTCTTG
EGFR	AGGCACGAGTAACAAGCTCAC	ATGAGGACATAACCAGCCACC
ERBB3	GGTGATGGGGAACCTTGAGAT	CTGTCACTTCTCGAATCCACTG
F11R	ATGGGGACAAAGGCGCAAG	CAATGCCAGGGAGCACAACA
FBN2	TGGATTTTGTTCCCGTCCTAAC	CAACGTCCACCATTCTGACAT
ITGB8	ACCAGGAGAAGTGTCTATCCAG	CCAAGACGAAAGTCACGGGA
LAMA2	TTTTGGAACGCTCTCTTGATGAT	CGTTAGGCACTCCGTGTCTG
LAMA4	TCTGCCTTTTGATGCCGTACT	CTCTCCGTGTGCAGTATCCC
LAMB1	TGACTTTCAAGACATTCCGTCC	AGGCGAAGTATCTATACACACCC
LEPREL2	TCAGGGTGCTAAGCTGCTTC	TAGTCCCGATAGGTGTAGGCT
LIFR	GCGTACCGACTGACTGCATTG	CCAGAGGGTGCTTTCCAAGAA
LUM	GGATTGGTAAACCTGACCTTCAT	GATAAACGCAGATACTGCAATGC
MFAP2	CGCCGTGTGTACGTCATTAAC	CCATCACGCCACATTTGGA
MMP9	TGTACCGCTATGGTTACACTCG	GGCAGGGACAGTTGCTTCT
NODAL	CAGTACAACGCCTATCGCTGT	TGCATGGTTGGTCGGATGAAA
NOTCH1	AGCCTCAACGGGTACAAGTG	CACACGTAGCCACTGGTCAT
SNAI1	TCGGAAGCCTAACTACAGCGA	AGATGAGCATTGGCAGCGAG
SNAI2	CGAACTGGACACACATACAGTG	CTGAGGATCTCTGGTTGTGGT
SNAI3	ACTGCGACAAGGAGTACACC	GAGTGCGTTTGCAGATGGG
TGFB1	GGCCAGATCCTGTCCAAGC	GTGGGTTTCCACCATTAGCAC
TGFB2	CAGCTTGTGCTCCAGACAGT	GCTCAATCCGTTGTTCAGGC
TWIST1	GTCCGCAGTCTTACGAGGAG	GCTTGAGGGTCTGAATCTTGCT
VIM	GACGCCATCAACACCGAGTT	CTTTGTCGTTGGTTAGCTGGT
ZEB1	GATGATGAATGCGAGTCAGATGC	ACAGCAGTGTCTTGTTGTTGT

Table 3. Real-time PCR primer sequences for mouse genes.

Gene Name	Forward Primer Sequence	Reverse Primer Sequence
Atg7	TCTGGGAAGCCATAAAGTCAGG	GCGAAGGTCAGGAGCAGAA
B2m	TTCACCCCCACTGAGACTGAT	GTCTTGGGCTCGGCCATA
Becn1	ATGGAGGGGTCTAAGGCGTC	TCCTCTCCTGAGTTAGCCTCT
Cdh1	CAGGTCTCCTCATGGCTTTGC	CTTCCGAAAAGAAGGCTGTCC
Cdh2	AGCGCAGTCTTACCGAAGG	TCGCTGCTTTCATACTGAACTTT
Cxcr4	GAGGCCAAGGAAACTGCTG	GCGGTCACAGATGTACCTGTC
Egfr	ATGAAAACACCTATGCCTTAGCC	TAAGTTCCGCATGGGCAGTTC
Glut1	CAGTTCGGCTATAACACTGGTG	GCCCCCGACAGAGAAGATG
Hif1α exon 2	TCGGCGAAGCAAAGAGTCTG	GCTCACATTGTGGGGAAGTG
Hif2α exon 2	TGAGGAAGGAGAAATCCCGTG	GGGCAACTCATGAGCCAACT
Hmbs	TCATGTCCGGTAACGGCG	CACTCGAATCACCCTCATCTTTG
Map1lc3a	GACCGCTGTAAGGAGGTGC	CTTGACCAACTCGCTCATGTTA
Map1lc3b	TTATAGAGCGATACAAGGGGGAG	CGCCGTCTGATTATCTTGATGAG
Notch1	GATGGCCTCAATGGGTACAAG	TCGTTGTTGTTGATGTCACAGT
Pdgfb	CATCCGCTCCTTTGATGATCTT	GTGCTCGGGTCATGTTCAAGT
Pgk1	TGGTGGGTGTGAATCTGCC	ACTTTAGCGCCTCCCAAGATA
Pthlh	ACATTGCTATGGGAGCCAC	TAGGAATCAGCGCCTCTAAC
Pymt	CTGCTACTGCACCCAGACAA	GCAGGTAAGAGGCATTCTGC
Snai1	CACACGCTGCCTTGTGTCT	GGTCAGCAAAAGCACGGTT
Snai2	CATCCTTGGGGCGTGTAAGTC	GCCCAGAGAACGTAGAATAGGTC
Snai3	GGTCCCCAACTACGGGAAAC	CTGTAGGGGGTCACTGGGATT
Sqstm1	GAACTCGCTATAAGTGCAGTGT	AGAGAAGCTATCAGAGAGGTGG
Tek	CTGGAGGTTACTCAAGATGTGAC	TCCGTATCCTTATAGCCTGTCC
Twist1	GGACAAGCTGAGCAAGATTCA	CGGAGAAGGCGTAGCTGAG
Ulk1	AAGTTCGAGTTCTCTCGCAAG	CGATGTTTTCGTGCTTTAGTTCC
Vegfa	GGAGATCCTTCGAGGAGCACTT	GGCGATTTAGCAGCAGATATAAGAA
Vhl exon 1	GACCCGTTCCAATAATGCCC	CGTCGAAGTTGAGCCACAAA
Zeb1	ACTGCAAGAAACGGTTTTCCC	GGCGAGGAACACTGAGATGT
Zeb2	ATTGCACATCAGACTTTGAGGAA	ATAATGGCCGTGTCGCTTCG

signature scores were plotted against each other as a correlation graph in Prism software (Graphpad) with a linear regression curve.

Proliferation assay

MCF7 NSC and MCF7 shCOL14A1 #1-4 cells were plated at a density of 100,000 cells/well in a 6-well dish. Each day, cells in one set of wells were lifted from the well, mixed with 0.4% trypan blue solution, and viable cells were counted using a TC-20 automated cell counter (Bio-Rad). Each day over the 4-day course, media from all remaining wells was aspirated and replaced with fresh media.

Adhesion assay

Wells of a 96-well plate were coated with fibronectin at 5 or 10 μg/ml, incubated for one hour at room temperature and then rinsed twice with PBS. 50,000 MCF7 NSC or MCF7 shCOL14A1 #1-4 cells in serum-free media were then added and allowed to adhere for 30 min or 1 hour at 37 °C. Media was then removed and well was gently washed with PBS. After adding methanol to wells and incubating for 10 min, methanol was removed and 0.5% crystal violet solution was added to stain adherent cells. After 10 min, crystal violet was removed by gently submerging the plate in water and rocking several times. Washes were repeated until all excess crystal violet was removed. Plates were allowed to dry and then images were collected on an Olympus BX41 Microscope equipped with an Olympus DP71 camera using the 10X objective. For absorbance quantification, 30% acetic acid in PBS was added to each well and incubated while rocking for 10 min. Absorbance was read at 600nm on a plate reader.

Animals

All experiments were performed following the relevant guidelines and regulations of the Animal Welfare Act and the Guide for the Care and Use of Laboratory Animals and were approved by the Institutional Animal Care and Use Committee (IACUC) at Vanderbilt University.

Mammary epithelial tumor cell-specific knock-out of *Hif1α* was achieved by breeding together 3 transgenic mouse strains. First, transgenic mice with loxP sites flanking both alleles of the Hif1α exon 2 (Jackson Laboratory Stock No. 007561, C57/B6 background) [325] were bred with transgenic mice expressing Cre recombinase downstream of mammary tumor virus long

terminal repeats (MMTV-LTR) (Jackson Laboratory Stock No. 003553, C57/B6 background) [326]. The progeny from this cross were then bred with transgenic mice expressing the polyoma middle T (PyMT) oncoprotein under the MMTV-LTR (Jackson Laboratory Stock No. 022974, C57/B6-FVB mixed background) [227]. Virgin female mice with Hif1α wild-type mammary fat pad tumors (Hif1α$^{f/f}$ PyMT^{+} = Hif1α$^{f/f}$, MMTV-Cre negative, MMTV-PyMT positive) or Hif1α-null mammary fat pad tumors (Hif1α$^{-/-}$ PyMT^{+} = Hif1α$^{f/f}$, MMTV-Cre positive, MMTV-PyMT positive) were used in these studies. Non-tumor bearing (PyMT^{-}) controls of both Hif1α$^{f/f}$ and Hif1α$^{-/-}$ mice were also used.

Mammary epithelial tumor cell-specific knock-out of *Hif2α* was achieved using the same breeding strategy as above, but using a transgenic mouse line with loxP sites flanking both alleles of the Hif2α exon 2 (Jackson Laboratory Stock No. 008407, C57/B6 background) [327]: Hif2α$^{f/f}$ PyMT^{+} = Hif2α$^{f/f}$, MMTV-Cre negative, MMTV-PyMT positive; Hif2α$^{-/-}$ PyMT^{+} = Hif1α$^{f/f}$, MMTV-Cre positive, MMTV-PyMT positive.

Similarly, mammary epithelial tumor cell-specific knock-out of *Vhl* was achieved by incorporating a transgenic mouse line with loxP sites flanking both alleles of the Vhl exon 1 (Jackson Laboratory Stock No. 012933, C57/B6 background) [328]: Vhl$^{f/f}$ PyMT^{+} = Vhl$^{f/f}$, MMTV-Cre negative, MMTV-PyMT positive; Vhl$^{-/-}$ PyMT^{+} = Vhl$^{f/f}$, MMTV-Cre positive, MMTV-PyMT positive.

Once weaned, mice were palpated twice per week and tumors were measured in three dimensions with digital calipers. Mice were collected when any tumor had grown to a size of 1 cm in diameter in any dimension, around 4 to 5 months of age. Littermate and cousin control mice were collected for each study. 45 min prior to collection, mice were inoculated with Hypoxyprobe (Hypoxyprobe-1 Omni Kit, Hypoxyprobe, Inc, catalog number HP3-1000Kit) via intraperitoneal injection at a dosage of 60 mg/kg body weight.

PCR

At weaning, tail snips were collected from each mouse. Genomic DNA was extracted from the tail snip and genotyping was performed by PCR amplification of *Hif1α* (F: GGAGCTATCTCTCTAGACC, R: GCAGTTAAGAGCACTAGTTG) [329], *Hif2α* (F: CTTCTTCCATCATCTGGGATCTGGGAC, R: CAGGCAGTATGCCTGGCTAATTCCAGTT) [327], or *Vhl* (F:

CTAGGCACCGAGCTTAGAGGTTGCG, R: CTGACTTCCACTGATGCTTGTCACAG) [329], as well as *Pymt* (F: GGAAGCAAGTACTTCACAAGGG, R: GGAAAGTCACTAGGAGCAGGG), and *Cre* (F: GCGGTCTGGCAGTAAAAACTATC, R: GTGAAACAGCATTGCTGTCACTT). The *Pymt* genotyping reaction also included an internal positive control reaction (F: CAAATGTTGCTTGTCTGGTG, R: GTCAGTCGAGTGCACAGTTT). Primer sequences for *Pymt* and *Cre* genotyping were obtained from Jackson Laboratories.

Recombination and loss of the *Hif1α* exon 2 was confirmed by PCR amplification using a three-primer system split between two separate reactions. The forward primer (Fwd: CAGTGCACAGAGCCTCCTC) binds to *Hif1α* exon 1, the first reverse primer (Rev1: GCTCACATTGTGGGGAAGTG) binds to exon 2, and the second reverse primer (Rev2: ATGTAAACCATGTCGCCGTC) binds to exon 3. The first reaction (Fwd and Rev1 primers) will not amplify a band if recombination has occurred, while the second reaction (Fwd and Rev2) will amplify a lower molecular weight band in the case of recombination. PCR reactions were set up using the HotStarTaq system (Qiagen) using 200 ng of cDNA generated from RNA extracted from tumor homogenates as the template. PCR reactions were carried out in a T100 Thermal Cycler (Bio-Rad) with the following conditions: 15 min at 95 °C, (1 min at 94 °C, 1.5 min at 59 °C, 1 min at 72 °C) x 38 cycles, followed by 10 min at 72 °C. The *B2m* locus was also amplified as a loading control, using the same primers as used for real-time PCR above, using the following conditions: 15 min at 95 °C, (1 min at 94 °C, 1.5 min at 53 °C, 1 min at 72 °C) x 35 cycles, followed by 10 min at 72 °C. Recombination of *Vhl* exon 1 was confirmed by PCR amplification using a one-reaction three-primer system as previously described [330].

Histology

All tissues collected were fixed in 10% formalin for 24 hours. Hind limb bones were then decalcified in EDTA (20% pH 7.4) solution for 72 hr prior to embedding. Tissues analyzed via histology and immunohistochemistry were embedded in paraffin and 5 μM thick sections were prepared for staining. Hematoxylin and eosin (H&E) staining was performed as previously described [316]. H&E stained slides of left lung, liver, and tibia sections were analyzed for the presence of metastatic mammary tumors under masked conditions by a board-certified veterinary anatomic pathologist. All tumors were imaged on an Olympus BX43 microscope equipped with

a SPOT Flex camera (Diagnostic Instruments Inc, Sterling Heights MI). Tumor areas were measured in SPOT software (Diagnostic Instruments Inc) and total tumor area per animal was calculated.

Immunostaining

Pimonidazole. Sections were deparaffinized and rehydrated by soaking the slides in Xylene Substitute (Thermo Fisher), 100%, 95%, 90%, and then 70% ethanol, and finally deionized water. Peroxidase activity was then quenched by incubating the slides in 3% hydrogen peroxide for 15 min. After slowly displacing the hydrogen peroxide solution with deionized water, slides were rinsed three times with PBS. The deparaffinized sections were blocked in serum-free protein blocking agent (Dako) for 5 min and incubated with primary antibody (Hypoxyprobe-1 Omni Kit, Hypoxyprobe, Inc, catalog number HP3-1000Kit, 1:100) in Dako protein block overnight at 4 °C. Negative control sections were incubated with Dako alone. The sections were then washed three times with PBS and incubated with biotinylated secondary antibody (goat-anti-rabbit IgG, Vector, catalog number BA-1000, 1:200) in Dako protein block for 30 min at 37 °C, followed by streptavidin-conjugated HRP (Millipore, OR03L, 1:200) in PBS for 30 min at 37 °C, and developed using the DAB ImmPACT kit (Vector, catalog number SK-4105) for approximately 1 minute. Chromogen development was then quenched by rinsing twice in deionized water. Sections were counterstained with hematoxylin and dehydrated by soaking them in 70%, 90%, 95%, and 100% ethanol, followed by Xylene Substitute. The coverslips were mounted using Permount (Fisher Scientific).

Ki-67. Staining was performed by the Vanderbilt University Medical Center Translational Pathology Shared Resource (TPSR, Nashville, TN) as follows: Slides were placed on the Leica Bond Max IHC stainer. All steps besides dehydration, clearing and coverslipping are performed on the Bond Max. Slides are deparaffinized. Heat induced antigen retrieval was performed on the Bond Max using their Epitope Retrieval 2 solution for 20 minutes. Slides were placed in a Protein Block (Ref# x0909, DAKO, Carpinteria, CA) for 10 minutes. The sections were incubated with anti-Ki67 (Catalog #12202S, Cell Signaling Technology, Danvers, MA) diluted 1:250 for one hour. The Bond Refine Polymer detection system was used for visualization. Slides were the dehydrated, cleared and coverslipped.

For pimonidazole and Ki-67 stains, all images were collected on an Olympus BX41 Microscope equipped with an Olympus DP71 camera using the 4X, 20X, and 40X objectives. Ki-67 or pimonidazole stained area of lung lesions was quantified using ImageJ software with manual tumor area contouring and automatic color thresholding. Pimonidazole-positive tumor area was quantified based on visual inspection of multiple micrographs with 4x objective based on a scale of 0 to 3: 0 = no nuclear staining, 1 = <10% positive nuclear staining, 2 = 10-50% positive nuclear staining, 3 = ≥50% positive nuclear staining. Each field was assigned a score and an average score for the tumor was calculated based on all fields. The number of fields inspected varied from 1 to 4, depending on the size of the tumor.

***CD4/CD8*.** Slides were stained using the Opal 7-Color Manual IHC Kit (PerkinElmer). In brief, slides were deparaffinized and rehydrated in a series of xylene and ethanol washes, microwaved in Rodent Decloaker (Biocare Medical) and then cooled. Slides were washed with water and then TBST (TBS + 0.05% Tween-20) followed by blocking with BLOXALL Blocking Solution (Vector Laboratories). The following antibodies were used: CD4 (Invitrogen, clone 4SM95; 1:100), CD8 (Invitrogen, clone 4SM16; 1:100), ImmPRESS HRP Goat anti-rat IgG (Vector Laboratories; 1:4). Staining with primary and secondary antibodies and OPAL fluorophores were performed per the manufacturer's instructions. All images were collected on a Zeiss 880/Airyscan Microscope using the 20X and 40X objectives. For quantitation, the 20X images were used to manually count the number of $CD4^+$ and $CD8^+$ cells and calculate nuclear area using color thresholding in ImageJ.

Microcomputed tomography (microCT)

Ex vivo microCT was performed on the proximal tibia using the Scanco μCT 50. Scans were initiated from the proximal end of the metaphyseal growth plate and progressed 250 slices distal. Tibiae were scanned at 7 μm voxel resolution, 55-kV voltage, and 200 μA current. Scans were reconstructed and analyzed using the Scanco Medical Imaging Software to determine the bone volume/total volume (BV/TV), trabecular number, thickness, and separation. The most distal slice of the growth plate was used as a reference slice and analysis was set to begin 20 slices distal from this point. A 150 slice region of interest was selected for analysis. An automated

contouring procedure was applied to separate the trabecular bone from the cortical bone and visually verified for each sample.

Flow cytometry

The epiphyses of the femur and tibia from one hindlimb were cut and the bones were flushed using centrifugation to obtain the bone marrow. The bone marrow was filtered through a 40 μm cell strainer to separate the cells from bone debris. Cells were suspended in red blood cell lysis buffer for 5 minutes on ice, spun down, and washed twice with PBS. Bone marrow (2×10^6 cells) was stained in 100ul of 1% BSA in PBS with 100ng EpCAM antibody (BD Pharmingen, catalog number 563478) for 1 hour at 4 °C in the dark. Cells were washed with PBS and resuspended in PBS and 0.5 ng DAPI for 15 min on ice. Flow cytometry experiments were analyzed in the VUMC Flow Cytometry Shared Resource using the 3-laser or 5-laser BD LSRII. Datasets were analyzed using FlowJo software (FlowJo, LLC). Cells were gated based on forward scatter and side scatter to identify single cells and then live cells (DAPI-) were gated based on EpCAM positivity using non-tumor bearing bone marrow as a negative control. Mammary fat pad tumors were mechanically digested and filtered through a 40 μm cell strainer to obtain a single cell suspension. These tumor cells were stained as described above and used as a positive control.

Statistical methods

For all studies, n per group is as indicated in the figure or figure legend and the scatter dot plots indicate the mean of each group and the standard error of the mean. All graphs and statistical analyses were generated using Prism software (Graphpad). All *in vitro* and *in vivo* assays were analyzed for statistical significance using two-tailed t test, Mann-Whitney test, log-rank test, one- or two-way ANOVA with multiple comparisons, or Fisher's exact test, as denoted in figure legends. Pearson and Spearman correlation coefficients were calculated for gene signature correlation analyses. $P < 0.05$ was statistically significant, and *$P < 0.05$, **$P < 0.01$, ***$P < 0.001$, ****$P < 0.0001$.

CHAPTER IV

TUMOR DORMANCY REGULATOR LIFR REGULATES EXTRACELLULAR MATRIX-RELATED GENES INCLUDING COL14A1

Summary

The bone is the most common site of metastasis across in breast cancer and patients remain at risk of delayed recurrence due to bone disseminated tumor cells existing dormancy. Leukemia inhibitory factor receptor (LIFR) expression in breast cancer cells is known to maintain cells in a dormant state, but the downstream effectors of LIFR signaling are not well defined. We found that a cluster of extracellular matrix (ECM) related genes were differentially expressed in MCF7 human breast cancer cells in response to LIFR knockdown. We further investigated the potential dormancy-related functions of one of these gene, collagen type XIV alpha 1 chain (COL14A1), which was downregulated in response to LIFR knockdown. We found that COL14A1 knockdown in MCF7 cells decreased proliferation *in vitro*. COL14A1 knockdown did not alter cell adhesion, expression of epithelial-to-mesenchymal transition (EMT) markers, or activity of major proliferation-related pathways known to be activated downstream of LIFR. While the mechanistic tie between COL14A1 and dormancy remains unclear, further study is warranted to more fully understand how LIFR signaling is influencing breast cancer cell ECM and how this relates to dormancy maintenance or escape.

Introduction

Following dissemination from the primary tumor to a distant site, breast cancer cells can remain dormant, rather than immediately colonizing the tissue to form metastatic lesions. Eventual exit from dormancy can therefore result in delayed metastatic recurrence. The bone is the most common site of metastasis across different breast cancer subtypes [7], and metastatic recurrence in the bone can significantly decrease life expectancy and quality of life, due to severe bone pain, hypercalcemia, and increased risk of fracture [6].

The mechanisms underlying tumor dormancy and how disseminated tumor cells exit dormancy remain under active investigation [331]. Leukemia inhibitory factor (LIF) receptor (LIFR), a member of the glycoprotein 130 (GP130) cytokine family and subunit of a

heterodimeric cytokine receptor expressed in the breast epithelium [332], was previously shown to promote breast dormancy in bone metastatic breast cancer cells [195]. LIFR is also known to act as a breast tumor suppressor [193] and inhibit breast cancer metastasis to the lung and bone [194, 195]. There are multiple cytokines that signal through LIFR, including LIF, oncostatin M (OSM), and ciliary neurotrophic factor (CNTF) which typically results in activation of STAT3, ERK, and AKT pathways across multiple cell types [332]. In breast cancer, the tumor suppressive functions of LIFR were shown to be mediated by downstream YAP/TAZ signaling [194], and the bone metastasis suppressor functions were proposed to be mediated through STAT3 signaling [195]. However, other genes and transcriptional networks that are regulated downstream of LIFR have not been characterized and remain largely unclear. The goal of this study was to identify potential LIFR downstream targets that may promote breast tumor suppression and inhibit metastasis, using short hairpin RNA (shRNA) induced knockdown of LIFR as a screening tool to identify differentially expressed genes.

Results

LIFR alters the expression of genes that regulate the extracellular matrix. In order to identify potential downstream targets of LIFR signaling that contribute to tumor dormancy in breast cancer cells, we performed RNAseq to compare the transcriptional profiles of MCF7 cells with short hairpin RNA (shRNA) knockdown of LIFR (MCF7 shLIFR cells) to MCF7 cells expressing a non-silencing control shRNA (MCF7 NSC cells). We chose this model since MCF7 cells typically lay dormant in the bone marrow following intracardiac inoculation [195, 281, 282], and knockdown of LIFR using a similar lentiviral knockdown strategy leads to MCF7 exit from dormancy and osteolytic bone destruction [195]. Genes identified in the MCF7 shLIFR samples with a minimum log2 fold change of +/- 1 compared to MCF7 NSC samples, with a p-value less than 0.05, were considered in further analyses (Fig. 4A). Of the 642 genes that matched this criteria, 399 genes were able to be mapped using the STRING database to investigate functional protein-protein interactions (Fig. 4B). To identify pathways or clusters of functionally related genes that may be regulated by LIFR, we removed gene nodes from the map that were not connected to any other nodes or were only connected to one or two other nodes. The remaining highly interconnected 17-gene network (Fig. 4C) was enriched for genes involved in several extracellular matrix (ECM) related pathways and some KEGG pathways related to

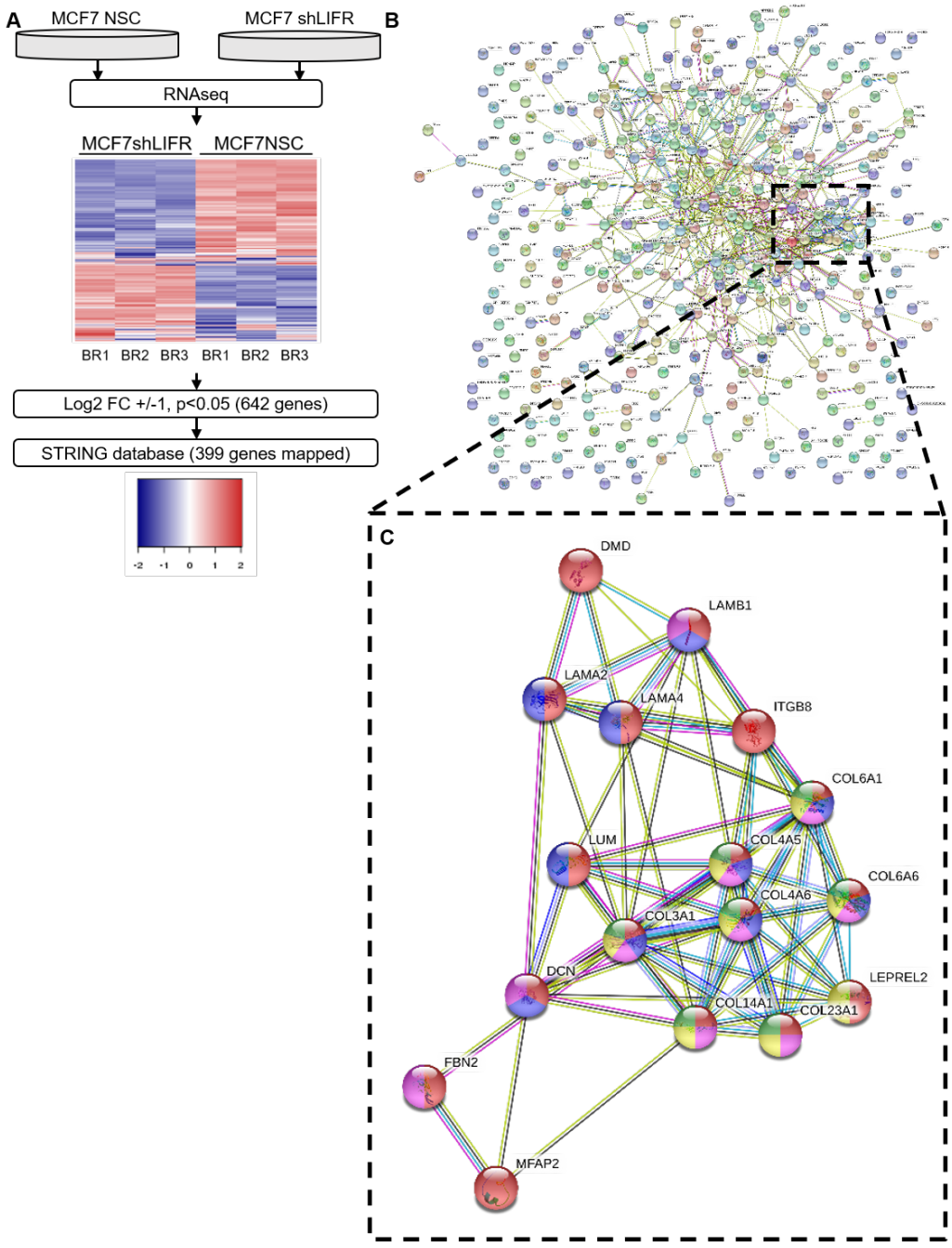

Figure 4. LIFR expression significantly alters the expression of ECM-related genes. (A) Schematic of RNAseq analysis strategy. MCF7 NSC and MCF7 shLIFR cells were analyzed by RNAseq to identify differentially expressed genes. Three independent biological replicates were analyzed for each group of cells. Significance thresholds were set to include genes that had a minimum Log2 fold change of +/- 1 and a p-value less than 0.05. Genes that met these criteria were then mapped using the STRING database to visualize protein-protein interactions. **(B)** STRING map generated from inputting all differentially expressed genes from RNAseq analysis that fit significance threshold criteria. **(C)** Highly interconnected gene network that resulted from removing all genes from the map that were connected to 2 or less other gene nodes. Colors of nodes correspond to the reactome pathways listed in Table 4.

cancer (Table 4). These findings indicate that LIFR expression significantly alters the expression of genes that regulate the ECM and suggests that ECM dysregulation may impact tumor dormancy.

COL14A1 is downregulated in LIFR knockdown cells. After confirmation of LIFR knockdown by western blot (Fig. 5A-B) and real-time PCR (Fig. 5C), expression of the 17 selected candidates from STRING analysis were measured in the MCF7 shLIFR cells to validate the RNAseq results. One gene (DCN) was not able to be validated since no amplification was detected from real-time PCR. Of the remaining 16 candidates, none had significant up- or down-regulation compared to the NSC cells across all three shLIFR clones that matched the directionality of the RNAseq results (Table 2). Five of the 16 candidates had up- or down-regulation that was consistent across the three shLIFR clones and matched the directionality of the RNAseq data, though the mRNA abundance between one or more of the shLIFR clones and the NSC cells did not reach the threshold of statistical significance (COL6A6, COL14A1, LAMA2, LAMA4, LAMB1).

Collagen type XIV alpha 1 chain (COL14A1) was selected for further analysis, as several previous studies indicate it has cancer- or quiescence-related functions [333-336]. COL14A1 expression was slightly reduced in two of the three shLIFR clones and significantly downregulated in one shLIFR clone (#8; Table 5 and Fig. 5D), and data from The Cancer Genome Atlas (TCGA) breast cancer dataset indicates that patients with COL14A1 mRNA downregulation have significantly shorter overall survival compared to patients with wildtype COL14A1 (Fig. 5E). This is consistent with previously reported data demonstrating a reduction in survival in patients with lower LIFR signaling in the primary tumor [195]. Taken together, these findings support a pro-dormancy role for COL14A1 in breast cancer.

COL14A1 knockdown decreases cell proliferation. Since MCF7 cells have the highest COL14A1 expression of the common breast cancer cell lines tested (Fig. 6A), MCF7 cells were used to generate COL14A1 knockdown cells to investigate the role of COL14A1 in breast cancer cell behavior. Four COL14A1 targeting shRNA clones were tested, and all four clones achieved significant knockdown of COL14A1 mRNA (Fig. 6B). We attempted to validate COL14A1 knockdown at the protein level but were unable to detect any COL14A1 protein by western blot

Table 4. Enriched pathways in STRING map. Top five most enriched reactome pathways from the STRING map in Figure 2B, as well as 3 of the 5 most enriched KEGG pathways are listed. KEGG pathway terms that were not cancer-related are not shown. The reactome pathways are color coded to match the nodes in Figure 4B.

Pathway	Description	FDR
Reactome Pathways		
HSA-1474244	Extracellular matrix organization	3.00×10^{-9}
HSA-3000178	ECM proteoglycans	7.48×10^{-8}
HSA-8948216	Collagen chain trimerization	6.64×10^{-6}
HSA-1650814	Collagen biosynthesis and modifying enzymes	6.64×10^{-6}
HSA-1474228	Degradation of the extracellular matrix	7.17×10^{-6}
KEGG Pathways		
hsa04151	PI3K-Akt signaling pathway	5.23×10^{-6}
hsa05200	Pathways in cancer	1.04×10^{-5}
hsa04512	ECM-receptor interaction	1.04×10^{-5}

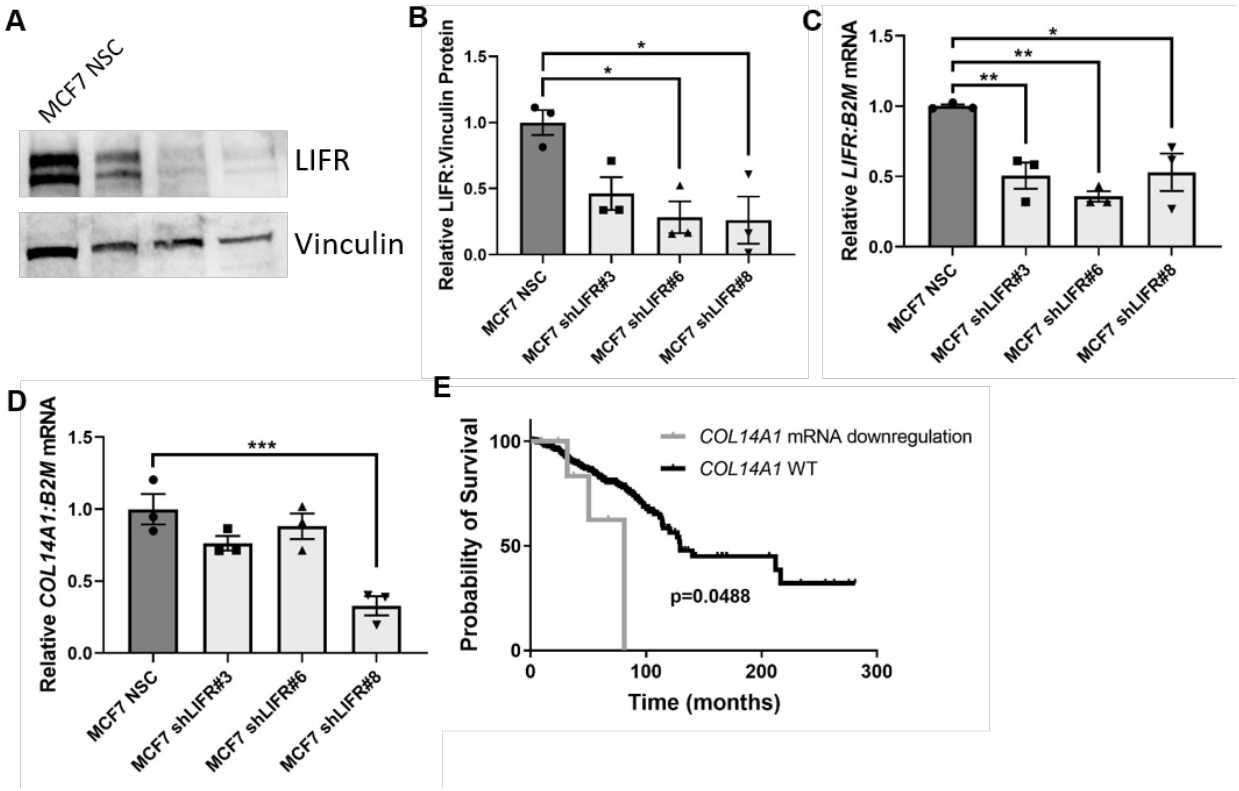

Figure 5. COL14A1 is downregulated in LIFR knockdown cells. (A, B) Western blot validation of LIFR knockdown in 3 separate LIFR targeting shRNA sequences. Representative images of three independent biological replicates are shown. Blots were quantified by densitometry. One-way ANOVA with multiple comparisons, n = 3 independent replicates. **(C)** Real-time PCR validation of LIFR knockdown. One-way ANOVA with multiple comparisons, n = 3 independent replicates. **(D)** Real-time PCR validation of RNAseq results, which indicated COL14A1 downregulation in MCF7 shLIFR cells. One-way ANOVA with multiple comparisons, n = 3 independent replicates. **(E)** Survival analysis of patient data from TCGA Breast Invasive Carcinoma dataset (TCGA Firehose Legacy, previously known as TCGA Provisional dataset) comparing overall survival of patients with wildtype COL14A1 to those with mRNA downregulation of COL14A1. n = 6 *COL14A1* mRNA downregulation, n = 217 *COL14A1* WT. Log-rank test. *P < 0.05, **P < 0.01, ***P < 0.001

Table 5. Real-time PCR validation of selected targets from STRING map cluster in MCF7 shLIFR cells. "RNAseq" column indicates the abundance of each gene transcript in the MCF7 shLIFR cells compared to the MCF7 NSC cells, represented as a Log2 foldchange. A positive number indicates that the gene was upregulated in shLIFR cells, while a negative value indicates downregulation. The values in the "Real-time PCR" columns represent the abundance of the gene transcript in each MCF7 shLIFR clone compared to the MCF7 NSC cells. Green shading in cells indicates that the directionality of expression change (upregulation or downregulation) compared to NSC was consistent with the directionality from RNAseq. One-way ANOVA with multiple comparison against NSC. *P < 0.05, **P < 0.01

Gene Name	RNAseq (Log2 FC)	Real-time PCR (Relative to NSC)		
		MCF7 shLIFR#3	MCF7 shLIFR#6	MCF7 shLIFR#8
COL3A1	-2.27	1.19	0.60	0.72
COL4A5	-1.40	1.25	1.47	1.47
COL4A6	-1.58	1.74	1.89	1.20
COL6A1	-1.19	1.34	0.84	1.05
COL6A6	1.62	1.33 *	1.42	1.50 **
COL14A1	-2.73	0.76	0.88	0.33 **
COL23A1	-1.26	1.10	0.66	0.51 *
DMD	-2.36	1.29	0.72 *	0.85
FBN2	-1.84	1.12	1.72	0.39
ITGB8	-1.07	1.31	1.09	0.50 **
LAMA2	-2.11	0.78	0 *	0.96
LAMA4	-4.21	0.65	0.70	0.40
LAMB1	1.77	2.68 *	18.65 *	19.45
LEPREL2	-1.81	0.76	4.24 **	3.35
LUM	2.41	0.39	1.15	1.23
MFAP2	-1.01	1.07	0.76	0.55

at the appropriate molecular weight (data not shown). Collectively, knockdown of COL14A1 significantly decreased proliferation compared to the NSC cells (Fig. 6C). Only shCOL14A1 #1 cells reached statistical significance when analyzed as an individual cell line compared to the NSC cells (Fig. 6C). Since altering COL14A1 would likely alter the tumor cell ECM, a fibronectin adhesion assay was performed, but no differences in adhesion were detected in any of the COL14A1 knockdown clones (Fig. 6D-E).

COL14A1 knockdown does not alter epithelial phenotype. Since changes in the ECM can alter the epithelial or mesenchymal state of tumor cells, we next investigated the epithelial phenotype of the MCF7 COL14A1 knockdown cells to determine whether COL14A1 knockdown triggers epithelial-to-mesenchymal transition (EMT). No morphological changes were noted in any of the shCOL14A1 clones compared to NSC controls when grown on 2D tissue culture plastic or in a 3D collagen I matrix (Fig. 7A). Next, the expression of a panel of EMT markers was examined by real-time PCR to determine whether any transcriptional changes had occurred that could explain the change in proliferation. While β-catenin (CTNNB1) expression was significantly elevated in one of the shCOL14A1 clones, no other significant changes in EMT marker expression were detectable (Fig. 7B). EMT marker expression changes were not statistically significant whether individual knockdown clones were compared to the NSC cells or whether all the knockdown clones were grouped together and compared to the NSC group. These data indicate that COL14A1 does not regulate an EMT transcriptional program in breast cancer cells.

Major cell proliferation pathway activity is unaltered in response to COL14A1 knockdown. Since our data demonstrate that COL14A1 is reduced in LIFR knockdown cells (Table 5, Fig. 5D), we can conclude that COL14A1 is regulated downstream of LIFR. However, these findings do not provide information on how LIFR signaling may regulate COL14A1 expression, or whether COL14A1 is upstream or downstream of signaling pathways known to be activated by LIFR, such as the MAPK, AKT, and STAT3 pathways [332]. To better determine the position of COL14A1 in the cascade of LIFR signaling downstream events, we probed for proteins involved in major signaling pathways activated by LIFR signaling in COL14A1 knockdown cells. No changes in phosphorylated ERK1/2 (pERK1/2), total ERK1/2, phosphorylated AKT, total AKT, phosphorylated STAT3, or total STAT3 levels were observed when MCF7 shCOL14A1 cells

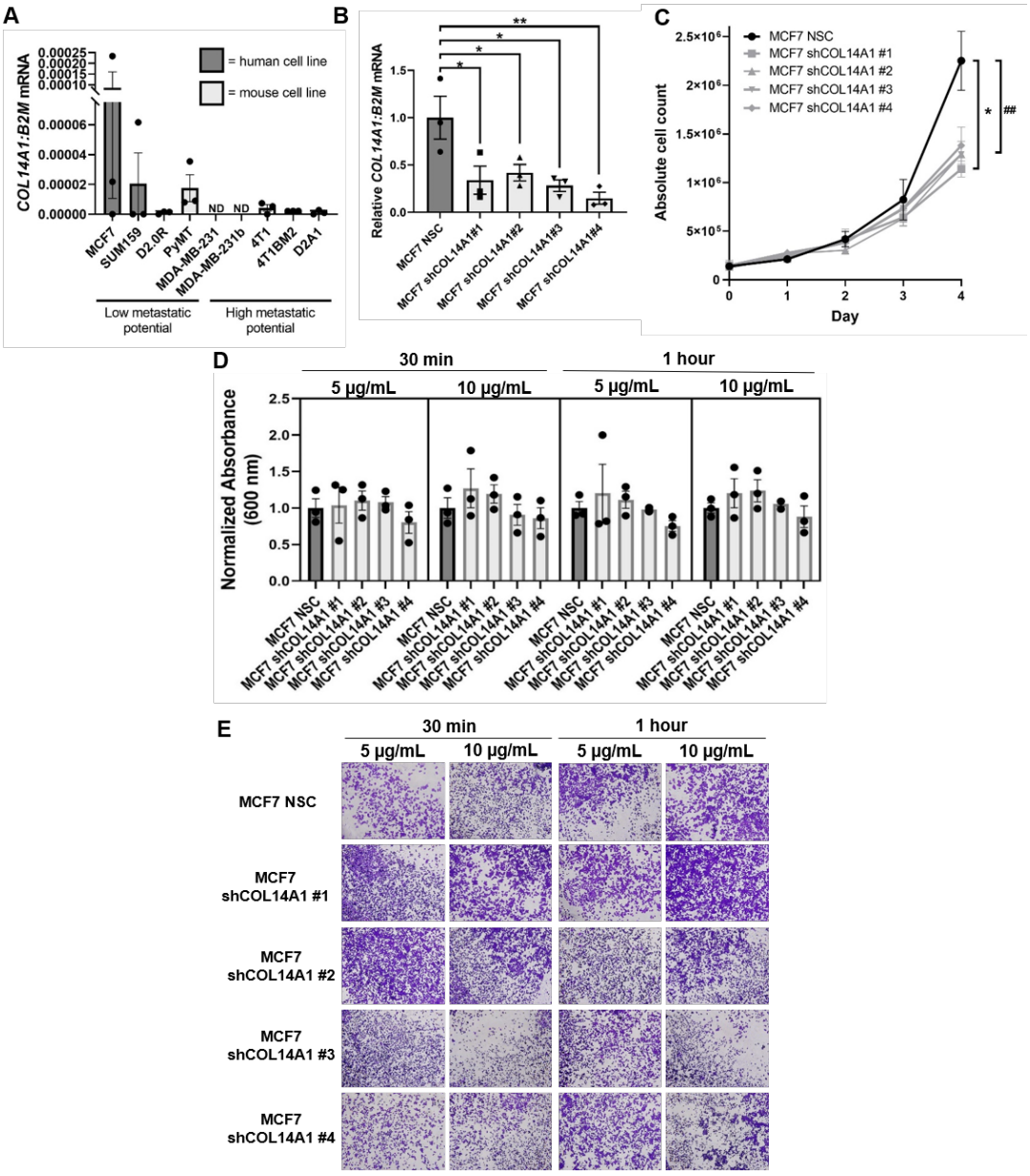

Figure 6. COL14A1 knockdown decreases cell proliferation. (A) Real-time PCR amplification of COL14A1 in a panel of breast cancer cell lines. n = 3 independent replicates. **(B)** Real-time PCR validation of COL14A1 knockdown across 4 separate COL14A1 targeting shRNA sequences. One-way ANOVA with multiple comparisons, n = 3 independent replicates. **(C)** Proliferation curves of MCF7 NSC and MCF7 shCOL14A1 clones across 4 days. Significant difference between NSC and shCOL14A1 #1 curves. * = 2-way ANOVA with multiple comparisons against NSC for each cell line. ## = 2-way ANOVA comparing NSC and all shCOL14A1 clones. n = 3 independent replicates. **(D, E)** Fibronectin adhesion assay comparing MCF7 NSC and MCF7 shCOL14A1 clones. Plates were coated with 5 or 10 □g/mL fibronectin and cells were allowed to adhere for 30 min or 1 hours. Adherent cells were stained with crystal violet and quantified by absorbance of 600 nm light. Images shown were taken with 10x objective. Within each condition, one-way ANOVA with multiple comparisons against NSC, n = 3 independent replicates. *P < 0.05, **P < 0.01, ##P < 0.01.

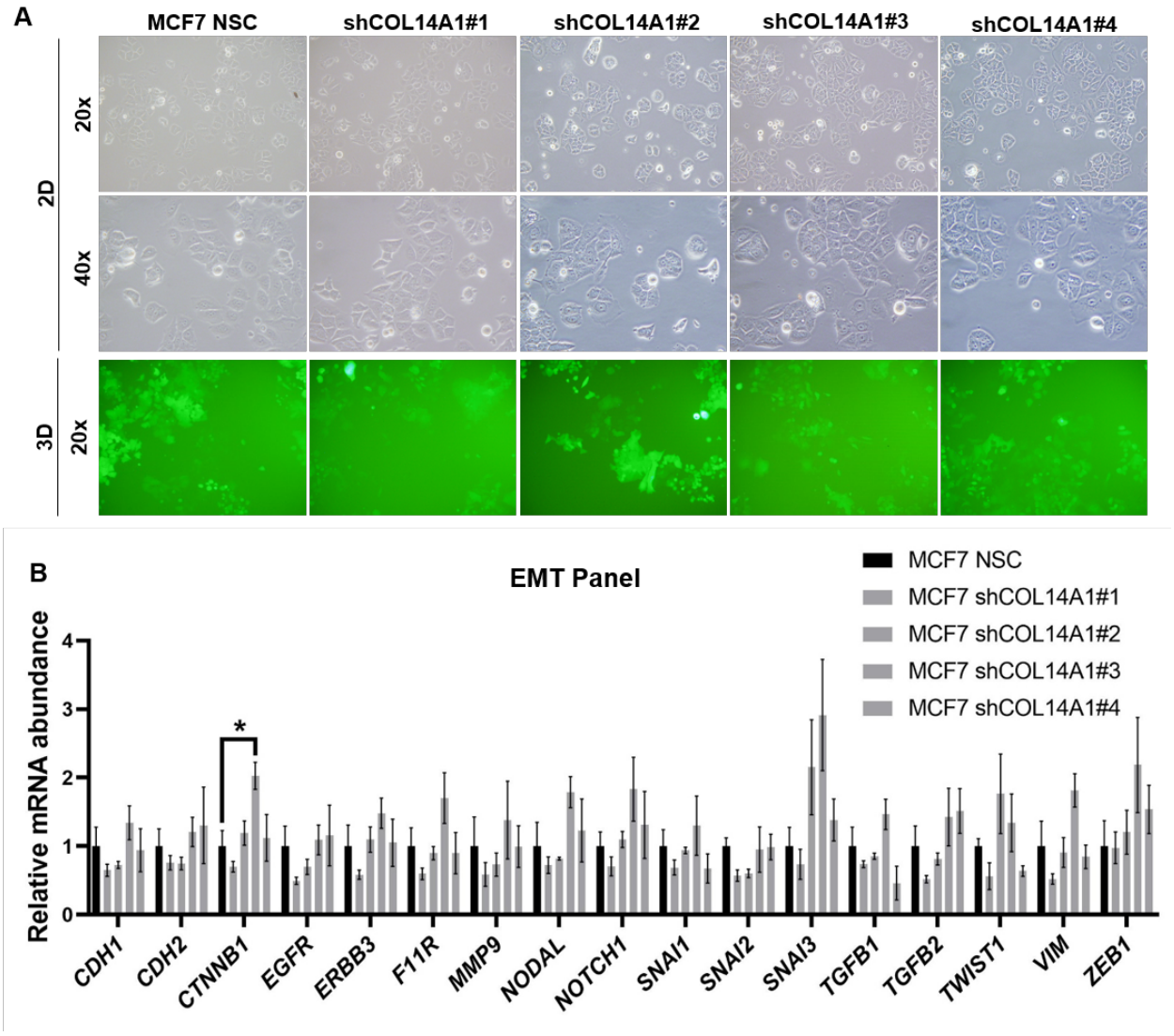

Figure 7. COL14A1 knockdown does not alter epithelial phenotype. (A) Images of MCF7 NSC and MCF7 shCOL14A1 cells depicting cell morphology. Images shown were taken with 20x or 40x objective. Cells were plated on cell culture plastic (2D) or in a type I collagen matrix (3D), as indicated. Cells grown in 2D were imaged 48 hours after plating. Cells grown in 3D were imaged 7 days after plating. **(B)** Real-time PCR amplification of a panel of EMT markers. Order of bars are MCF7 NSC, MCF7 shCOL14A1 #1, MCF7 shCOL14A1 #2, MCF7 shCOL14A1 #3, MCF7 shCOL14A1 #4 (from left to right). For each gene, one-way ANOVA with multiple comparisons against NSC, n = 3 independent replicates. *P < 0.05.

were grown on standard tissue culture plastic (Fig. 8A-D). There was a slight trend toward an increase in STAT3 signaling, but this did not reach statistical significance. Since COL14A1 is an extracellular matrix component, we next investigated whether signaling pathway activity would be altered when cells were grown on type I collagen coated plates. Type I collagen is the major collagen isoform in bone [337-339], and thus growing cells on a collagen matrix would better model the substrate that breast cancer cells would encounter when growing in the bone. Similar to the cells grown on tissue culture plastic, no significant changes in signaling proteins were observed when cells were grown on type I collagen coated plates (Fig. 8E-H). Taken together, it appears that the reduced proliferation observed in the MCF7 shCOL14A1 cells is not the result of reduced signaling activity through any of these major pathways we probed.

Discussion

Collagen type XIV is a fibril-associated collagen secreted into the ECM, where it is involved in the integration of collagen fibrils into larger fibers [340]. Type XIV collagen has been reported to induce quiescence in fibroblasts and reduce DNA synthesis [333], while other studies show that type XIV collagen is highly expressed in metastatic tissues [334]. COL14A1 was found to have increased promoter methylation levels in luminal breast tumors when compared to basal and HER2+ subtypes [335], suggesting that COL14A1 levels could contribute to some of the differences that are observed between different breast cancer subtypes. Additionally, the COL14A1 promoter is frequently methylated in renal cell carcinoma (RCC), which is associated with poor patient prognosis [336].

In this study, we found that COL14A1 is significantly downregulated in response to LIFR knockdown. LIFR knockdown has been shown to promote exit from dormancy and tumor outgrowth in the bone marrow [195], and thus we originally hypothesized that COL14A1 would have pro-dormancy functions since it was down-regulated in these “post-dormant” cells. Instead, COL14A1 knockdown modestly reduced the proliferation of MCF7 human breast cancer cells, indicating that COL14A1 has pro-proliferation functions. These seemingly contradictory results could indicate that the “post-dormant” phenotype observed in LIFR knockdown cells is due to other LIFR downstream effectors, and COL14A1-specific downregulation achieves a different phenotype. The mechanism behind this decreased proliferation in response to COL14A1 knockdown remains unclear at this time, but we have confirmed that it is not due to changes in

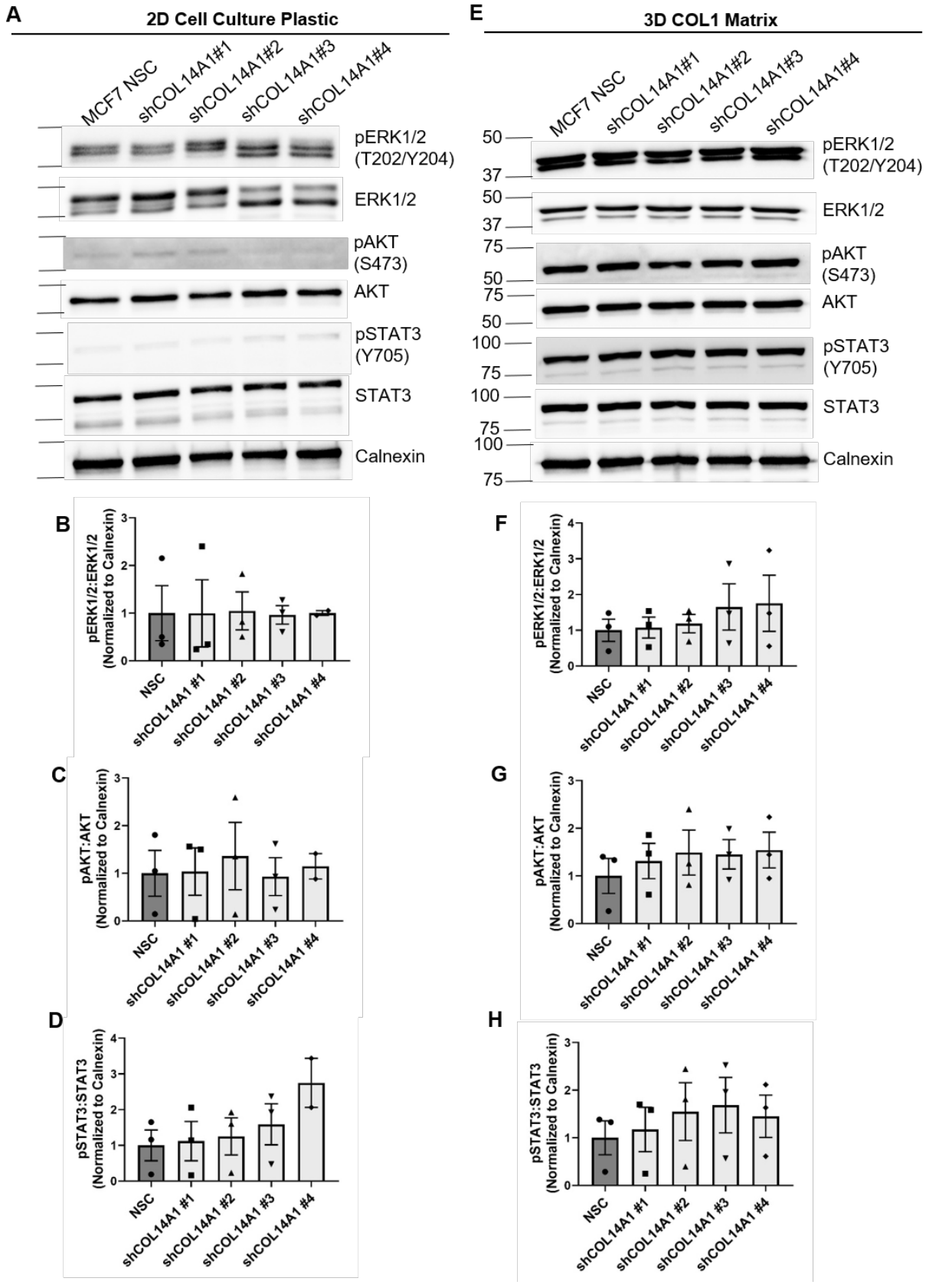
A
2D Cell Culture Plastic
MCF7 NSC
shCOL14A1#1
shCOL14A1#2
shCOL14A1#3
shCOL14A1#4
pERK1/2 (T202/Y204)
ERK1/2
pAKT (S473)
AKT
pSTAT3 (Y705)
STAT3
Calnexin
E
3D COL1 Matrix
B
pERK1/2:ERK1/2 (Normalized to Calnexin)
C
pAKT:AKT (Normalized to Calnexin)
D
pSTAT3:STAT3 (Normalized to Calnexin)
F
G
H
NSC
shCOL14A1 #1
shCOL14A1 #2
shCOL14A1 #3
shCOL14A1 #4

Figure 8. Major signaling pathways are unaltered in COL14A1 knockdown cells. (A-D) Western blot analysis of ERK, AKT, and STAT3 phosphorylation in MCF7 NSC and MCF7 shCOL14A1 cells plated on cell culture plastic. Blots are quantified using densitometry and the phosphorylated isoform levels are compared to the total levels of the target protein. One-way ANOVA with multiple comparisons against NSC, n = 3 independent replicates expect for MCF7 shCOL14A1 #4 where n = 2. **(E-H)** Western blot analysis of ERK, AKT, and STAT3 phosphorylation in MCF7 NSC and MCF7 shCOL14A1 cells plated on type I collagen coated plates. Blots are quantified using densitometry and the phosphorylated isoform levels are compared to the total levels of the target protein. One-way ANOVA with multiple comparisons against NSC, n = 3 independent replicates.

STAT3, AKT, or ERK signaling, which regulate cell proliferation [332, 341-343]. Furthermore, we detected no changes in adhesion, EMT marker expression, or the epithelial or mesenchymal morphology of the cells when grown in 2D or 3D conditions. Thus, the mechanism by which COL14A1 knockdown slows proliferation is still unclear.

One limitation of our study design is that our analysis does not provide information on whether ECM-related genes, including COL14A1, identified from RNAseq are direct downstream targets of LIFR signaling. The mechanistic connection between LIFR signaling and COL14A1 regulation is not yet clear, and due to COL14A1's role in modulating ECM, its function is difficult to study *in vitro.* However, our *in vitro* data suggest that loss of COL14A1 may slow tumor progression. Additionally, since LIFR expression is known to be downregulated in response to hypoxia [195], it would be of worth to determine whether the expression of COL14A1, or any of the other LIFR-regulated ECM factors, is altered in response to hypoxia as well. These findings could shed light on the mechanism of dormancy-escape by breast cancer cells in hypoxia.

Another major finding from this work that warrants further investigation is the fact that LIFR signaling appears to regulate many ECM-related genes. ECM composition and matrix stiffness can alter the behavior of breast cancer cells and are known to promote tumor invasion and metastasis [62] as well as osteolytic gene expression [344]. In addition, breast cancer cells grown in 3D culture have been observed to undergo cytoskeletal reorganization, form actin stress fibers, and begin interacting with the ECM more tightly as they transition from a quiescent to proliferative state [281, 345]. Current evidence suggests a lack of integrin-mediated adhesion between a tumor cell and the ECM can cause the tumor cell to enter a dormant state [345]. Thus, if LIFR downregulation alters ECM composition or tumor cell adhesion to the ECM, this could contribute to tumor cell escape from dormancy. Taken together, more in-depth *in vitro* and *in vivo* studies are warranted to determine the role for COL14A1 and other LIFR-regulated ECM genes in tumor progression, metastasis, and dormancy.

CHAPTER V

HYPOXIA INDUCIBLE FACTOR SIGNALING IN BREAST TUMORS CONTROLS SPONTANEOUS TUMOR DISSEMINATION IN A SITE-SPECIFIC MANNER

Summary

Hypoxia is a common feature in tumors and induces signaling that promotes tumor cell survival, invasion, and metastasis. To better understand the contributions of hypoxia inducible factor 1 alpha (HIF1α), HIF2α, and general HIF pathway activation in metastasis to lung and bone, we employed a PyMT-driven spontaneous murine mammary carcinoma model with mammary specific deletion of *Hif1α, Hif2α,* or von Hippel-Lindau factor (*Vhl*) using the Cre-lox system. We found that *Hif1α* or *Hif2α* deletion in the primary tumor decreased metastatic tumor burden in the bone marrow, while *Vhl* deletion increased bone tumor burden, as hypothesized. Unexpectedly, *Hif1α* deletion increased metastatic tumor burden in the lung, while deletion of *Hif2α* or *Vhl* did not affect pulmonary metastasis. Mice with *Hif1α* deleted tumors also exhibited reduced bone volume as measured by micro computed tomography, suggesting that disruption of the osteogenic niche may be involved in the preference for lung dissemination observed in this group. In contrast, known metastasis regulators such as CXCR4 and parathyroid hormone related protein (PTHrP) appear to regulate bone dissemination in response to VHL or HIF2α expression in the primary tumor. Thus, we reveal that HIF signaling in breast tumors controls tumor dissemination in a site-specific manner.

Introduction

Tumor cells frequently experience hypoxic conditions as the metabolic demands of the proliferating cells exceed the supply of oxygen and nutrients from the existing blood vessels. Cells must adapt to these stressful conditions by altering their metabolism and recruiting new blood vessels to increase oxygen supply [346]. The activation of hypoxia inducible factor (HIF) signaling triggers these transcriptomic adaptations in response to low oxygen levels. Under normoxic conditions, hypoxia inducible factor 1 alpha (HIF1α) and HIF2α are hydroxylated by prolyl hydroxylation domain containing enzymes (PHDs) [12-15], which allows Von Hippel-Lindau factor (VHL) [46], an E3 ubiquitin ligase, to bind to and ubiquitinate HIF1α and HIF2α,

marking them for proteasomal degradation [22-24]. In hypoxic conditions, PHD enzymes are inactive, leading to the stabilization of the alpha subunits, which can then dimerize with HIF1β and translocate to the nucleus [31, 32]. Once in the nucleus, the HIF1 and HIF2 complexes bind to hypoxia response elements (HREs) in the promoters of hypoxia responsive genes and act as transcription factors [34-36]. HIF1α drives the expression of genes such as vascular endothelial growth factor (VEGF) to stimulate angiogenesis [40, 41], as well as glucose transporters, glycolytic enzymes, and lactose dehydrogenase A (LDHA) to shift the main energy source of the cell to glycolysis [42-45, 347]. HIF signaling also promotes tumor cell metastasis by driving the expression of genes that control epithelial-to-mesenchymal transition (EMT), invasion, and extracellular matrix composition [49-51]. Furthermore, clinical evidence from breast cancer patients shows that high HIF1α levels in primary tumors correlate with poor patient outcomes [63-66], and a hypoxic transcriptomic signature in tumor cells is associated with bone metastasis [92, 143]. As such, HIF inhibitors are an attractive therapeutic avenue and are currently in development and undergoing clinical trials [348].

High breast cancer patient morbidity and mortality arises from metastatic dissemination of tumor cells from the primary site, which occurs early in tumor progression [2, 3]. Approximately 70% of breast cancer patients present with lung or bone metastases upon autopsy [8, 349]. Thus, there is an urgent need to identify the molecular factors that drive tumor dissemination to distant metastatic sites. Previous studies suggest that HIF1α expression in breast cancer cells promotes lung dissemination in genetic models [94] and bone colonization and osteolysis following intracardiac or orthotopic inoculation of MDA-MB-231 human breast cancer cells [93, 96, 97]. However, the comparative contributions of Hif1α and Hif2α on spontaneous bone dissemination are not well understood. Furthermore, dissemination patterns to bone and lung, the two leading sites of metastasis for breast cancer, have not been simultaneously evaluated in a spontaneous metastasis model. We therefore generated three transgenic mouse models of spontaneous mouse mammary carcinoma with tumor specific deletion of *Hif1α*, *Hif2α*, and *Vhl* and evaluated the effects of HIF modulation on tumor dissemination to multiple distant sites using highly sensitive detection techniques that have been optimized to detect low levels of disseminated tumor burden [261].

Results

Deletion of Hif1α increases total tumor burden while slowing primary tumor growth. To assess the impact of primary tumor HIF1α expression on breast tumor cell dissemination to the bone, we generated an immune-competent spontaneous murine mammary carcinoma model with mammary specific deletion of *Hif1α* using the Cre-lox system. In this model, mammary tumors grow spontaneously, driven by the polyoma middle T antigen (PyMT) expressed under the mouse mammary tumor virus long terminal repeats (MMTV-LTR), which restricts the oncogene expression to the mammary epithelium. In this study we compared female Hif1α$^{-/-}$ PyMT^{+} mice (Hif1α$^{f/f}$, Cre-positive, PyMT-positive) to control Hif1α$^{f/f}$ PyMT^{+} mice (Hif1α$^{f/f}$, Cre-negative, PyMT-positive) (Fig. 9A). In this spontaneous model, mammary tumors were first palpable around 8 weeks of age and reached endpoint (any tumor reaching 1 cm in diameter) around 20 weeks of age for the Hif1α$^{f/f}$ PyMT^{+} mice, while the Hif1α$^{-/-}$ PyMT^{+} mice took significantly longer (average of 23 weeks of age) to reach end point (Fig. 9B, C). This is consistent with previous reports using this model [94]. Interestingly, the total tumor weight was greater on average in Hif1α$^{-/-}$ PyMT^{+} mice upon sacrifice (Fig. 9D), while the number of tumors per mouse was not significantly increased (Fig. 9E).

We confirmed through real-time quantitative PCR analysis of tumor homogenate RNA that Hif1α$^{-/-}$ tumors had significant deletion of *Hif1α* (Fig. 9F), while transcript levels of *Hif2α*, the other major HIF pathway signaling factor, were unaffected (Fig. 9G). Recombination and deletion of *Hif1α* was further confirmed by PCR amplification of the *Hif1α* locus (Fig. 10A, B). *Hif1α* and *Hif2α* transcript levels were unaffected in the lung, suggesting that we did not have off-target editing in other soft tissue sites (Fig. 10C, D). Furthermore, the expression of *Vegfa*, a downstream target of Hif1α, was significantly lower in Hif1α$^{-/-}$ tumors (Fig. 9H), while the staining intensity of pimonidazole, a hypoxia marker, was comparable in Hif1α$^{f/f}$ and Hif1α$^{-/-}$ tumors (Fig. 9I, J). This confirms that Hif1α$^{-/-}$ tumors have a dampened hypoxia response despite experiencing similar levels of hypoxia as Hif1α$^{f/f}$ tumors.

Deletion of Hif1α in the mammary fat pad reduces trabecular bone volume. Since bone disseminated breast tumor cells can cause the formation of osteolytic lesions, we first assessed trabecular bone volume of tibiae from Hif1α$^{f/f}$ PyMT^{+} and Hif1α$^{-/-}$ PyMT^{+} mice by micro computed tomography (microCT) as a readout of tumor-induced bone destruction. To ensure that

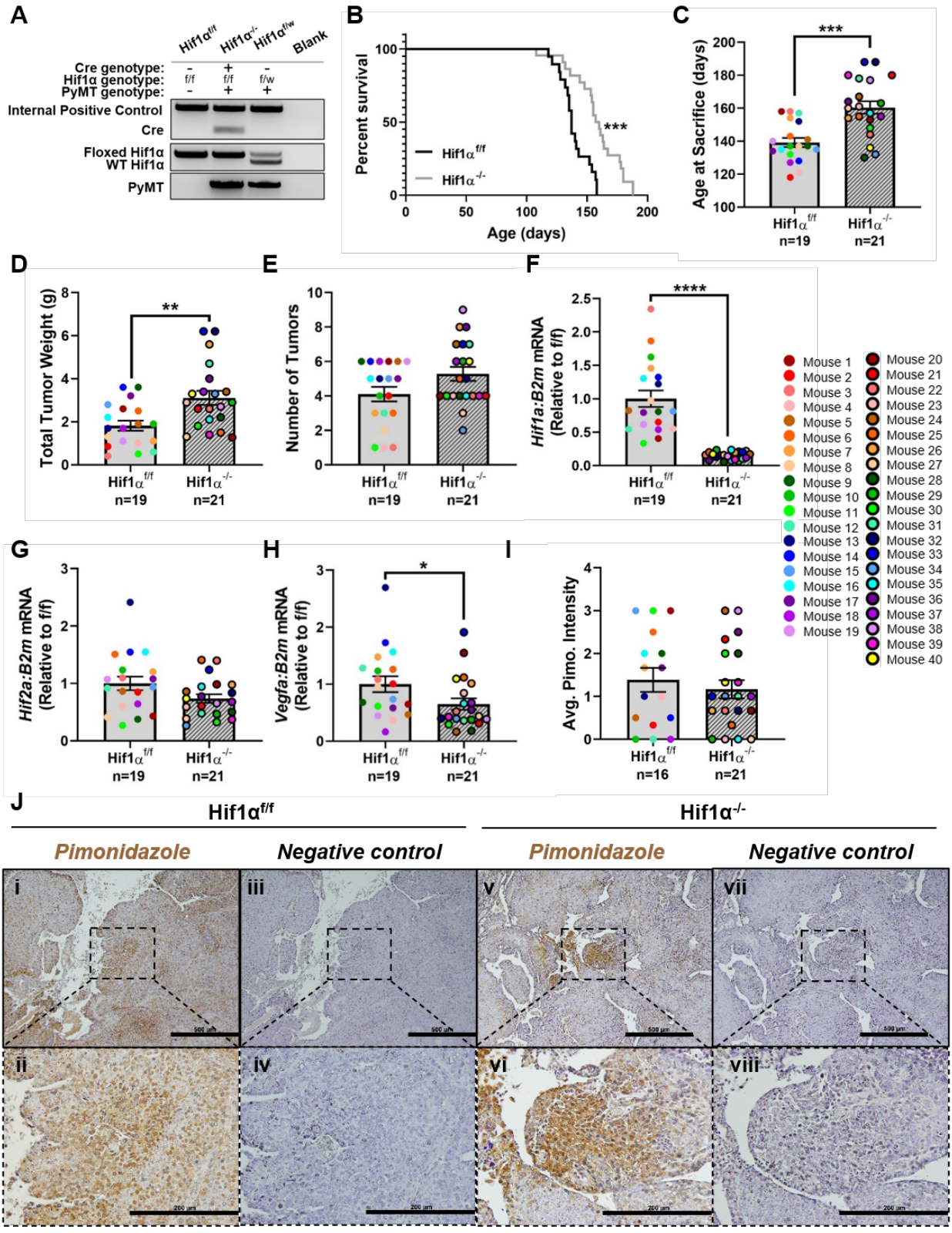
A
Hif1α f/f
Hif1α -/-
Hif1α f/w
Blank
Cre genotype:
Hif1α genotype:
PyMT genotype:
Internal Positive Control
Cre
Floxed Hif1α
WT Hif1α
PyMT
B
Percent survival
Age (days)
Hif1α f/f
Hif1α -/-
***
C
Age at Sacrifice (days)
***
Hif1α f/f n=19
Hif1α -/- n=21
D
Total Tumor Weight (g)
**
E
Number of Tumors
F
Hif1a:B2m mRNA (Relative to f/f)
****
G
Hif2a:B2m mRNA (Relative to f/f)
H
Vegfa:B2m mRNA (Relative to f/f)
*
I
Avg. Pimo. Intensity
Hif1α f/f n=16
Hif1α -/- n=21
Mouse 1
Mouse 2
Mouse 3
Mouse 4
Mouse 5
Mouse 6
Mouse 7
Mouse 8
Mouse 9
Mouse 10
Mouse 11
Mouse 12
Mouse 13
Mouse 14
Mouse 15
Mouse 16
Mouse 17
Mouse 18
Mouse 19
Mouse 20
Mouse 21
Mouse 22
Mouse 23
Mouse 24
Mouse 25
Mouse 26
Mouse 27
Mouse 28
Mouse 29
Mouse 30
Mouse 31
Mouse 32
Mouse 33
Mouse 34
Mouse 35
Mouse 36
Mouse 37
Mouse 38
Mouse 39
Mouse 40
J
Hif1α f/f
Hif1α -/-
Pimonidazole
Negative control
Pimonidazole
Negative control
i
ii
iii
iv
v
vi
vii
viii

Figure 9. Deletion of *Hif1α* increases total tumor burden while slowing primary tumor growth. (A) Example genotyping gel of Cre, floxed Hif1α, and PyMT from Hif1α$^{f/f}$ PyMT^{+}, Hif1α$^{-/-}$ PyMT^{+}, and Hif1α$^{f/w}$ PyMT^{-} mice. **(B)** Survival analysis of Hif1α$^{f/f}$ PyMT^{+} and Hif1α$^{-/-}$ PyMT^{+} mice where endpoint represents sacrifice due to tumor size reaching collection threshold. Log-rank test. **(C-E)** Comparison of the age at sacrifice, total burden at sacrifice, and number of tumors collected per mouse. Two-tailed Mann-Whitney test. (**F-H)** Quantitative PCR analysis of *Hif1α, Hif2α,* and *Vegfa* expression compared to *B2m* from whole tumor homogenate RNA. Expression is normalized to the mean of the f/f control group. Two-tailed Mann-Whitney test. **(I)** The average pimonidazole staining intensity for each mouse across multiple images from a single tumor. Two-tailed Mann-Whitney test. **(J)** Representative images of pimonidazole staining, taken with 10x and 40x objectives. The 40x field is denoted with a dashed box in the 10x view. Scale bars represent 500 μm in 10x fields, and 200 μm in 40x fields. Negative controls lacked the primary antibody incubation step. Graphs represent mean per group and error bars represent s.e.m. *P < 0.05, **P < 0.01, ***P < 0.001, ****P < 0.0001.

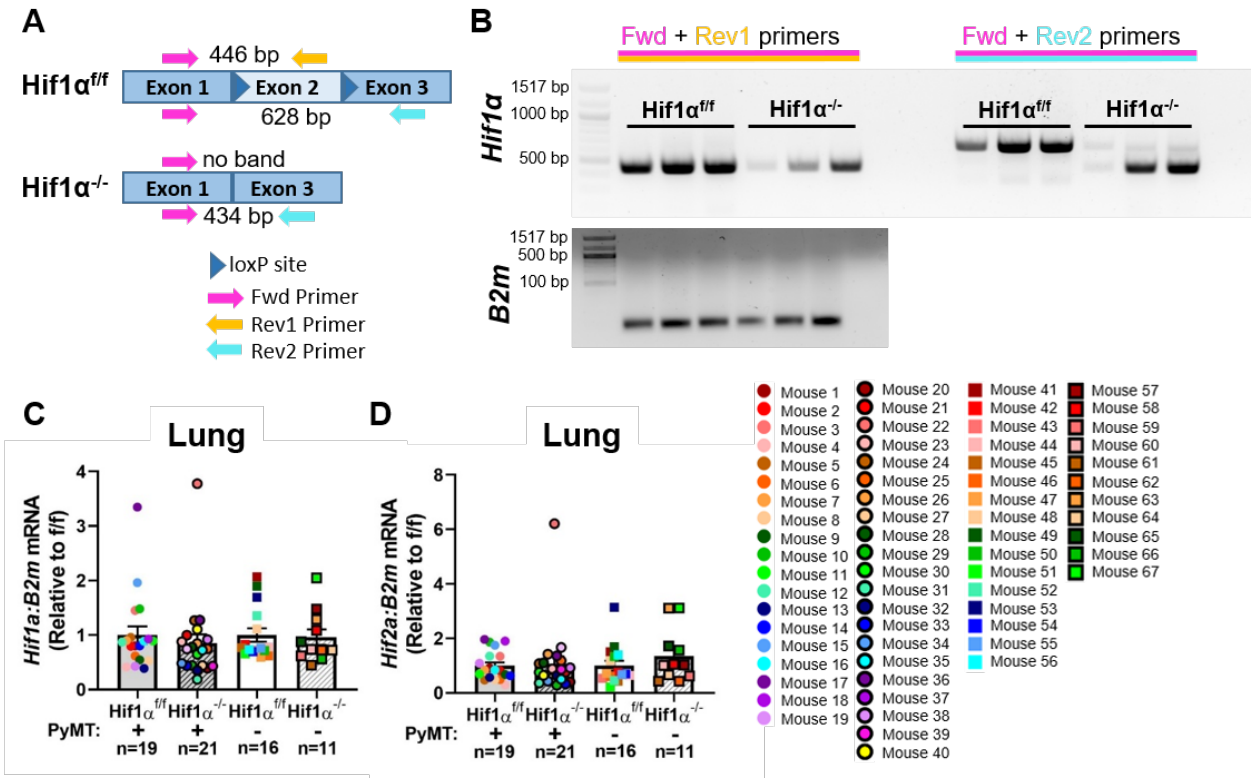

Figure 10. Validation of mammary fat pad-specific *Hif1α* recombination. (A) Schematic of PCR-based validation of *Hif1α* locus recombination using two separate PCR reactions. cDNA was used as the input material for these reactions. Thus, no introns are included in the diagram. The loxP sites shown are for reference to indicate which exon is excised upon recombination. No loxP sequence is present in the mRNA/cDNA. **(B)** DNA electrophoresis gels of the PCR products from the reactions depicted in A. The lower intensity of the bands in the Hif1α$^{-/-}$ tumors from the "Fwd + Rev1" reaction, and the lower molecular weight of the band resulting from the "Fwd + Rev2" reaction indicate successful recombination. The residual band in the Hif1α$^{-/-}$ tumors from the "Fwd + Rev1" reaction is likely from non-recombined stromal cells present in the tumor. *B2m* was also amplified to control against differences in cDNA concentration. **(C, D)** Quantitative PCR analysis of *Hif1α* or *Hif2α* transcript, respectively, compared to *B2m* from right lung homogenate RNA. Two-tailed Mann-Whitney test. Graphs represent mean per group and error bars represent s.e.m.

Hif1α deletion in the mammary fat pad did not alter baseline bone microarchitecture, we also scanned tibiae from non-tumor bearing controls ($PyMT^-$) of each genotype. Bone volume and trabecular number were significantly decreased in $Hif1\alpha^{-/-}$ $PyMT^+$ mice, with an accompanying increase in trabecular spacing (Fig. 11A-D), but bone volume was unaltered with *Hif1α* deletion in $PyMT^-$ mice, suggesting that the reduction in bone volume observed in $Hif1\alpha^{-/-}$ $PyMT^+$ mice was due to tumor-induced osteolysis. $Hif1\alpha^{-/-}$ $PyMT^-$ mice did exhibit a significant increase in trabecular thickness (Fig. 11E), but this may not be biologically significant given the absence of changes in any other structural parameters for bone. Surprisingly, we found no discernible tumor burden present in the bone marrow of $Hif1\alpha^{-/-}$ $PyMT^+$ mice upon histological inspection by a certified veterinary pathologist, save in one mouse (Fig. 11F, G). Thus, *Hif1a* deletion in the primary tumor decreases trabecular bone volume but does not drive the development of macroscopic or osteolytic lesions in the bone.

Deletion of Hif1α decreases bone dissemination while increasing lung metastasis. Given the lack of macroscopic tumor lesions in the bone and the fact that the main site of metastasis for the PyMT-driven mammary carcinoma model is the lung rather than the bone marrow [224, 350], we employed several sensitive strategies to determine whether there were differences in tumor dissemination to bone. First, tumor cells were detected by flow cytometry of bone marrow from the tibiae and femora from $Hif1\alpha^{f/f}$ $PyMT^+$ and $Hif1\alpha^{-/-}$ $PyMT^+$ mice based on EpCAM (epithelial cell adhesion molecule) positivity. While some background EpCAM staining was detected in non-tumor bearing ($PyMT^-$) bone marrow (Fig. 12), a significant decrease in the number of $EpCAM^+$ cells was detected in the bone marrow from $Hif1\alpha^{-/-}$ $PyMT^+$ mice compared to $Hif1\alpha^{f/f}$ $PyMT^+$ mice when normalized to total tumor weight at endpoint (Fig. 13A, Fig. 14A). Second, the tumor-specific *Pymt* transcript was quantified from femur and spine homogenate RNA as a marker of tumor burden (Fig. 13B, C, Fig. 14B, C). No significant difference in tumor burden was detected in the femur and spine of $Hif1\alpha^{-/-}$ $PyMT^+$ mice using this method. Taken together, these results suggest that *Hif1α* in the primary tumor promotes tumor cell dissemination to the bone.

In addition to quantifying tumor burden in bone sites, we quantified tumor burden in the lung by histological inspection in order to confirm that $Hif1\alpha^{-/-}$ $PyMT^+$ mice had decreased tumor burden, as reported previously [94]. Surprisingly, $Hif1\alpha^{-/-}$ $PyMT^+$ mice had a significant

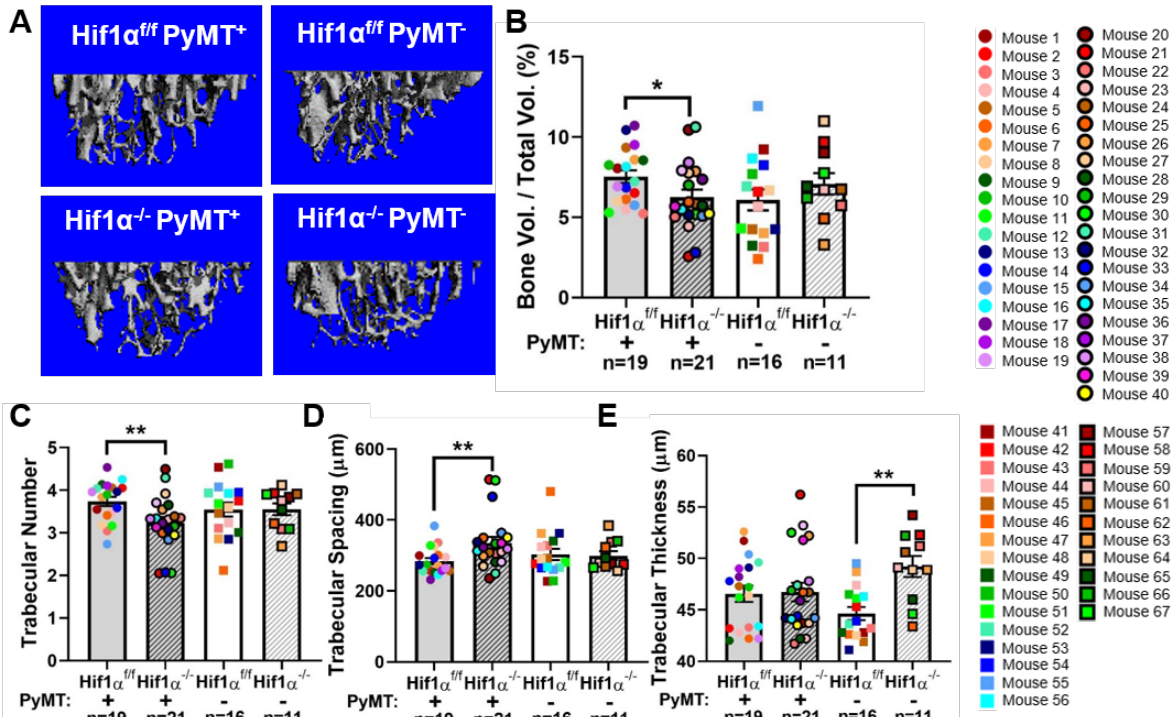
A
Hif1α^f/f PyMT+
Hif1α^f/f PyMT-
Hif1α-/- PyMT+
Hif1α-/- PyMT-
B
Bone Vol. / Total Vol. (%)
PyMT:
n=19
n=21
n=16
n=11
C
Trabecular Number
D
Trabecular Spacing (µm)
E
Trabecular Thickness (µm)
Mouse 1
Mouse 2
Mouse 3
Mouse 4
Mouse 5
Mouse 6
Mouse 7
Mouse 8
Mouse 9
Mouse 10
Mouse 11
Mouse 12
Mouse 13
Mouse 14
Mouse 15
Mouse 16
Mouse 17
Mouse 18
Mouse 19
Mouse 20
Mouse 21
Mouse 22
Mouse 23
Mouse 24
Mouse 25
Mouse 26
Mouse 27
Mouse 28
Mouse 29
Mouse 30
Mouse 31
Mouse 32
Mouse 33
Mouse 34
Mouse 35
Mouse 36
Mouse 37
Mouse 38
Mouse 39
Mouse 40
Mouse 41
Mouse 42
Mouse 43
Mouse 44
Mouse 45
Mouse 46
Mouse 47
Mouse 48
Mouse 49
Mouse 50
Mouse 51
Mouse 52
Mouse 53
Mouse 54
Mouse 55
Mouse 56
Mouse 57
Mouse 58
Mouse 59
Mouse 60
Mouse 61
Mouse 62
Mouse 63
Mouse 64
Mouse 65
Mouse 66
Mouse 67
F
Hif1α^f/f PyMT+
Hif1α-/- PyMT+
Hif1α^f/f PyMT-
Hif1α-/- PyMT-
i
ii
iii
iv
v
vi
vii
viii
G
Mouse 27
i
ii
iii
T
T

Figure 11. Deletion of *Hif1α* in the mammary fat pad reduces trabecular bone volume. (A) Representative 3D renderings of microCT scans of the proximal metaphysis of the right tibia. (**B-E)** Quantification of bone volume as a percentage of total volume, trabecular number, trabecular spacing, and trabecular thickness. Two-tailed Mann-Whitney test against corresponding f/f control. **(F)** Representative H&E stained images of the proximal metaphysis of the tibia taken with 4x and 20x objectives. The 20x field is denoted with a dashed box in the 4x view. **(G)** H&E stained images of the one histologically detectable bone metastatic lesion, identified in the distal region of the tibia from Mouse 27. Lower magnification images taken with 4x (i), 20x (ii) objectives, while highest magnification image (iii) is taken at 600X magnification. Area of higher magnification is indicated in lower magnification images with a dashed box. Tumor area labeled T and indicated by dashed circle. Atypical cells denoted with arrowheads. Graphs represent mean per group and error bars represent s.e.m. *$P < 0.05$, **$P < 0.01$.

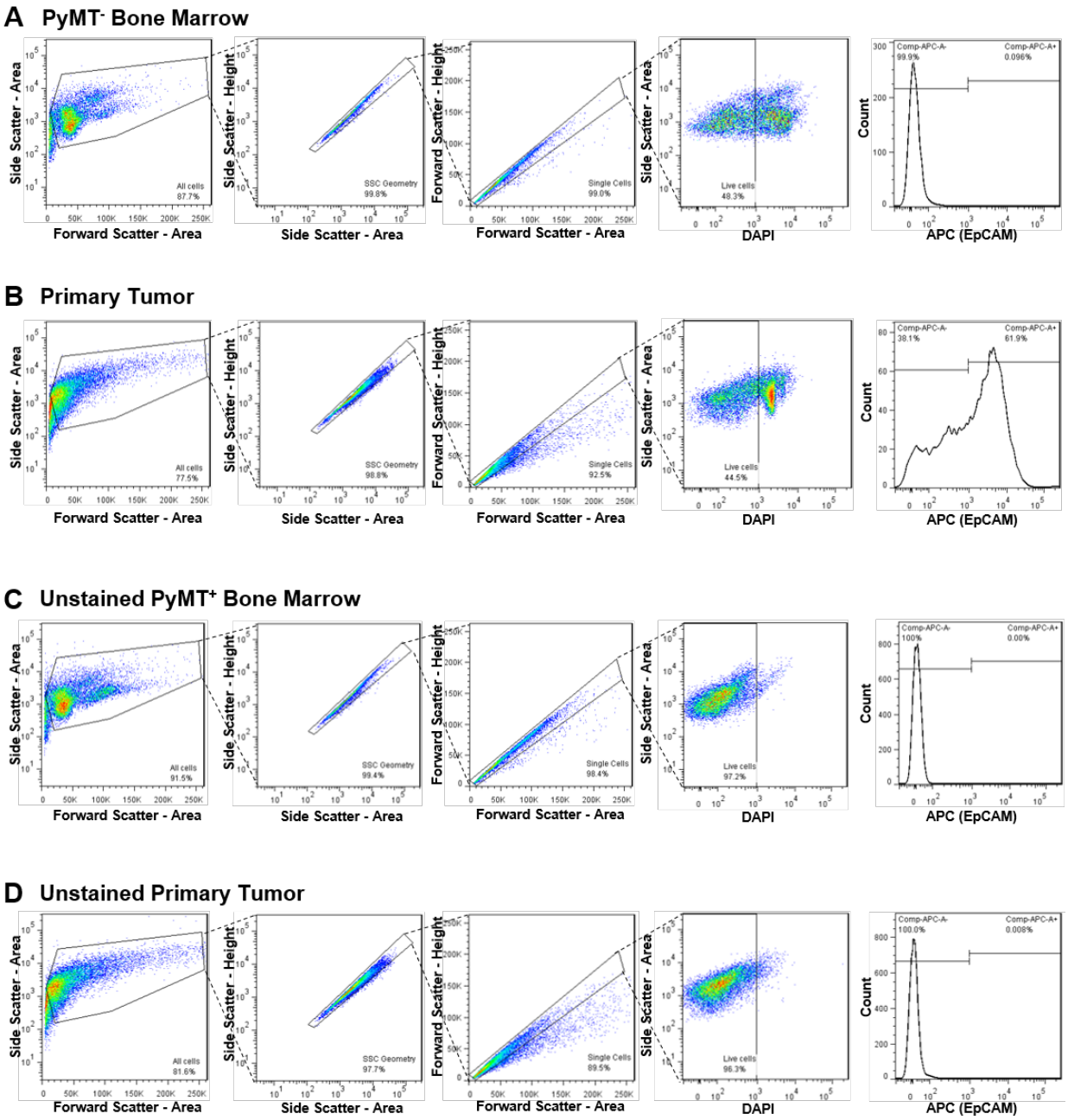

Figure 12. Flow cytometry gating strategy. (A) Gating of PyMT$^-$ (non-tumor bearing) bone marrow that acts as a negative control. **(B)** Gating of mechanically digested primary tumor cells that act as a positive control. **(C)** Gating of unstained PyMT$^+$ bone marrow. **(D)** Gating of unstained primary tumor cells. In each case, cells were first gated based on forward and side scatter to gate out very small events that are likely debris. These events are next gated on side and forward scatter geometry to identify single cells. These single cell events are next gated on DAPI intensity as a live-dead stain. DAPI$^-$ cells are then gated based on APC (EpCAM) intensity to detect tumor cells.

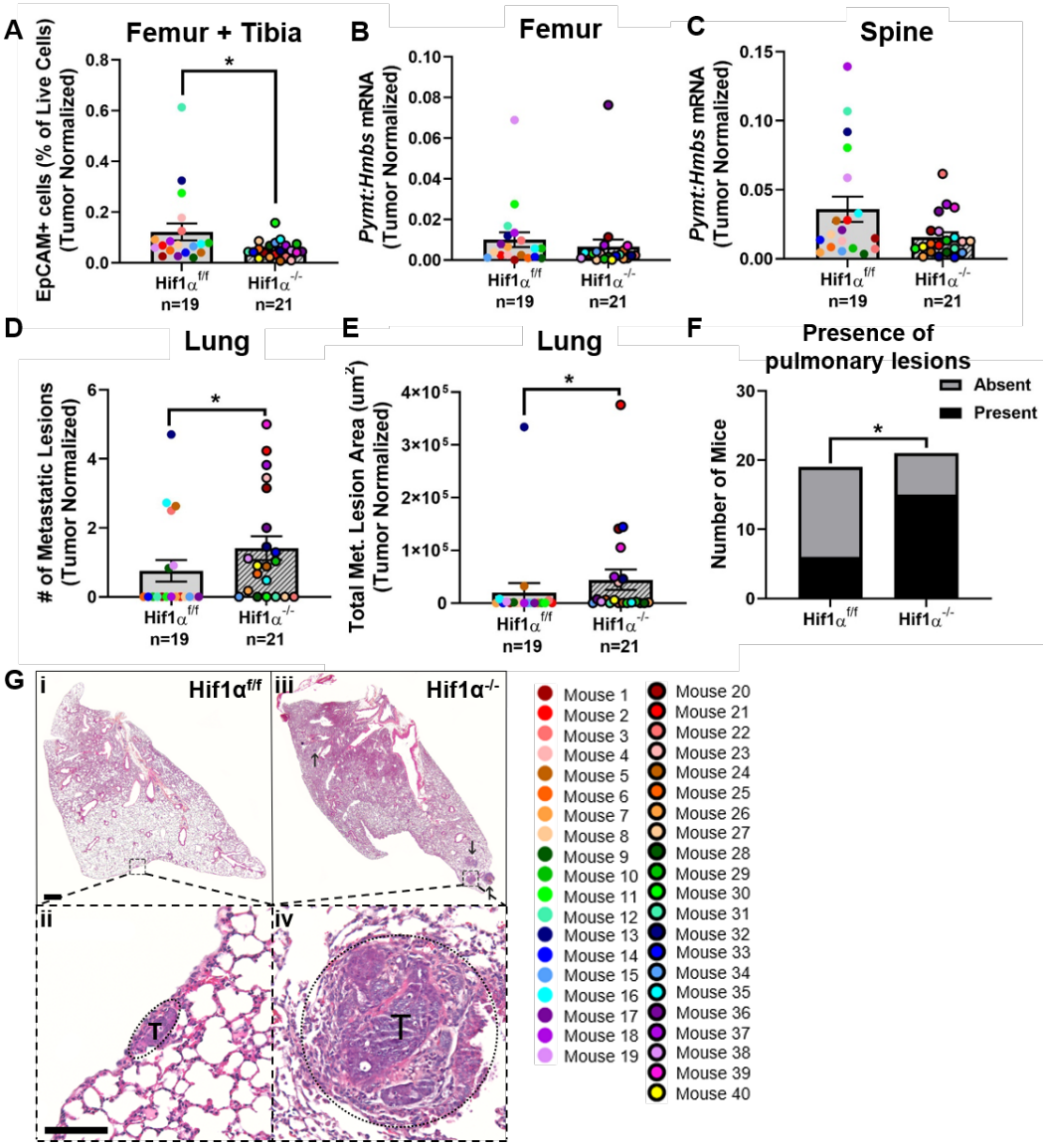

Figure 13. Deletion of *Hif1α* decreases bone dissemination while increasing lung metastasis. **(A)** The percentage of EpCAM$^+$ cells, out of the total number of live cells, detected by flow cytometry analysis of left hindlimb bone marrow. Numbers are normalized to the total tumor weight of each mouse. Two-tailed Mann-Whitney test. **(B, C)** Quantitative PCR analysis of *Pymt* transcript compared to *Hmbs* from right femur or spinal midsection, respectively. *Pymt* expression was then normalized to the total tumor weight of each mouse. Two-tailed Mann-Whitney test. **(D, E)** Metastatic lesion number or area detected by histological analysis of H&E stained sections from the left lung. Numbers are normalized to the total tumor weight of each mouse. Two-tailed Mann-Whitney test. **(F)** Comparison of the proportion of mice from each group that had any detectable pulmonary lesions. Fisher's exact test. **(G)** Representative images of H&E stained lung sections. Scale bar in sub-gross photomicrographs is 500 μm. Scale bar in high-power micrographs is 100 μm. The high-power image field is denoted with a dashed box in the sub-gross view. Tumor area is denoted with a dashed oval in the high-power images (labeled T). Additional metastatic lesions in the sub-gross view are denoted with arrows. Graphs represent mean per group and error bars represent s.e.m. *P < 0.05.

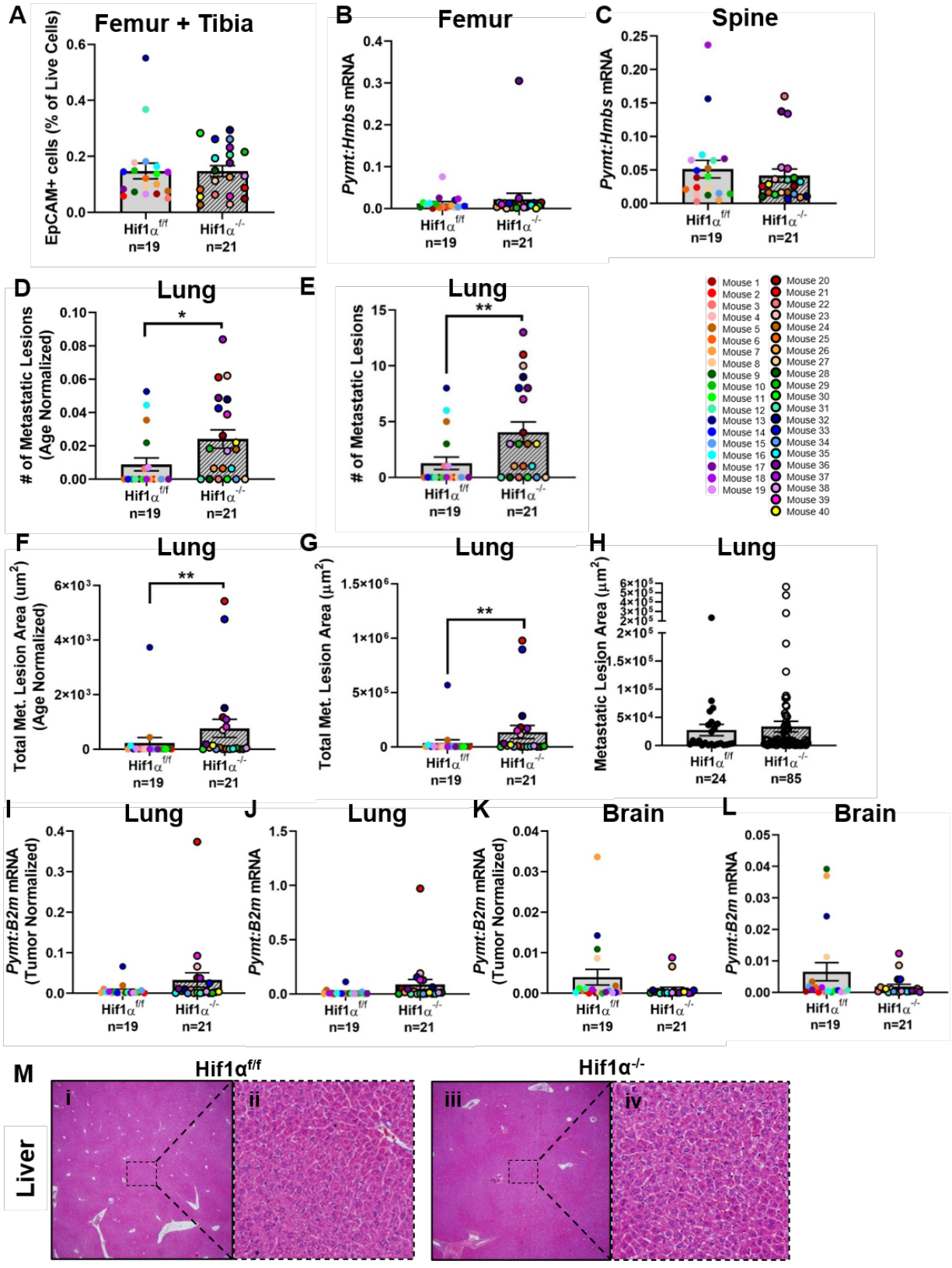
A
Femur + Tibia
EpCAM+ cells (% of Live Cells)
Hif1α f/f n=19
Hif1α -/- n=21
B
Femur
Pymt:Hmbs mRNA
C
Spine
D
Lung
# of Metastatic Lesions (Age Normalized)
E
Lung
# of Metastatic Lesions
Mouse 1
Mouse 2
Mouse 3
Mouse 4
Mouse 5
Mouse 6
Mouse 7
Mouse 8
Mouse 9
Mouse 10
Mouse 11
Mouse 12
Mouse 13
Mouse 14
Mouse 15
Mouse 16
Mouse 17
Mouse 18
Mouse 19
Mouse 20
Mouse 21
Mouse 22
Mouse 23
Mouse 24
Mouse 25
Mouse 26
Mouse 27
Mouse 28
Mouse 29
Mouse 30
Mouse 31
Mouse 32
Mouse 33
Mouse 34
Mouse 35
Mouse 36
Mouse 37
Mouse 38
Mouse 39
Mouse 40
F
Lung
Total Met. Lesion Area (um2) (Age Normalized)
G
Lung
Total Met. Lesion Area (µm2)
H
Lung
Metastatic Lesion Area (µm2)
Hif1α f/f n=24
Hif1α -/- n=85
I
Lung
Pymt:B2m mRNA (Tumor Normalized)
J
Lung
Pymt:B2m mRNA
K
Brain
Pymt:B2m mRNA (Tumor Normalized)
L
Brain
Pymt:B2m mRNA
M
Hif1α f/f
Hif1α -/-
Liver
i
ii
iii
iv

Figure 14. Alternate normalization of tumor burden in bone and soft tissue sites from *Hif1α* knockout mice. (A) The percentage of $EpCAM^+$ cells, out of the total number of live cells, detected by flow cytometry analysis of left hindlimb bone marrow. Two-tailed Mann-Whitney test. **(B, C)** Quantitative PCR analysis of *Pymt* transcript compared to *Hmbs* from right femur or spinal midsection, respectively. Two-tailed Mann-Whitney test. **(D-G)** Total metastatic lesion number or area detected by histological analysis of H&E stained sections from the left lung. Numbers are normalized to the mouse's age at sacrifice (D, F) or left un-normalized (E, G). Two-tailed Mann-Whitney test. **(H)** Comparison of individual lesion areas detected from histological inspection of left lung sections. Two-tailed Mann-Whitney test. **(I-L)** Quantitative PCR analysis of *Pymt* transcript compared to *B2m* from right lung or brain. Numbers are normalized to total tumor weight (I, K) or left un-normalized (J, L). Two-tailed Mann-Whitney test. **(M)** Representative H&E stained images of the liver taken with 4x and 40x objectives. The 40x field is denoted with a dashed box in the 4x view. Graphs represents mean per group and error bars represent s.e.m. $*P < 0.05$, $**P < 0.01$.

increase in the number of metastatic lesions in the lung (Fig. 13D, Fig. 14D, E) and total metastatic lesion area (Fig. 13E, Fig. 14F, G), regardless of whether the data were normalized to total tumor weight at endpoint, the mouse age at sacrifice, or left un-normalized. Individual lesion size was not significantly different between the two groups (Fig. 14H), indicating that the increase in total tumor area is driven by the greater number of lesions. Hif1α$^{-/-}$ PyMT^{+} mice also had significantly greater incidence of pulmonary lesions compared to Hif1α$^{f/f}$ PyMT^{+} mice (Fig. 13F). A non-significant trend in increased tumor burden was observed in the contralateral lung of Hif1α$^{-/-}$ PyMT^{+} mice by *Pymt* transcript levels (Fig. 14I, J). To determine whether the increased tumor burden in the lung was indicative of a global metastatic increase in soft tissue sites, tumor burden was also measured in the brain and liver. There was a non-significant trend toward a reduction in tumor burden in the brain by *Pymt* transcript levels in Hif1α$^{-/-}$ PyMT^{+} mice (Fig. 14K, L), and no liver lesions were detected by histological analysis by a certified veterinary pathologist (Fig. 14M). Thus, *Hif1a* deletion in the primary tumor reduces bone dissemination, but also specifically promotes lung metastasis.

There was no difference in expression of general breast cancer metastasis-associated genes (Fig. 15A), nor in EMT markers (Fig. 15B), between primary tumors from the Hif1α$^{f/f}$ PyMT^{+} and Hif1α$^{-/-}$ PyMT^{+} mice. This is consistent with site-specific differences in tumor burden, rather than a global increase or decrease in dissemination to all the distant sites measured. We also measured the expression of a panel of autophagy markers, since previous reports have shown that hypoxia-induced autophagy can affect pulmonary tumor burden. Inhibition of autophagy in hypoxic breast cancer cells has been shown to promote pulmonary metastasis [351], while autophagy has also been shown to promote the survival of dormant breast cancer cells and promote metastatic tumor recurrence [352]. However, we saw no differences between Hif1α$^{f/f}$ and Hif1α$^{-/-}$ tumors in any of the autophagy markers tested (Fig. 15C).

We therefore examined gene expression data from The Cancer Genome Atlas (TCGA) Invasive Breast Carcinoma patient dataset to determine whether hypoxia differentially induced gene expression profiles associated with site-specific metastasis to bone or lung. We found that a 42-gene hypoxia signature identified by Ye *et al.* [322] significantly and positively correlated with the bone metastasis signature established by Kang *et al.* [305] (Fig. 15D). Thus, hypoxia appears to drive a large transcriptomic program that promotes bone dissemination. However, a similar trend was observed for the lung metastasis signature from Minn *et al.* [323] (Fig. 15E).

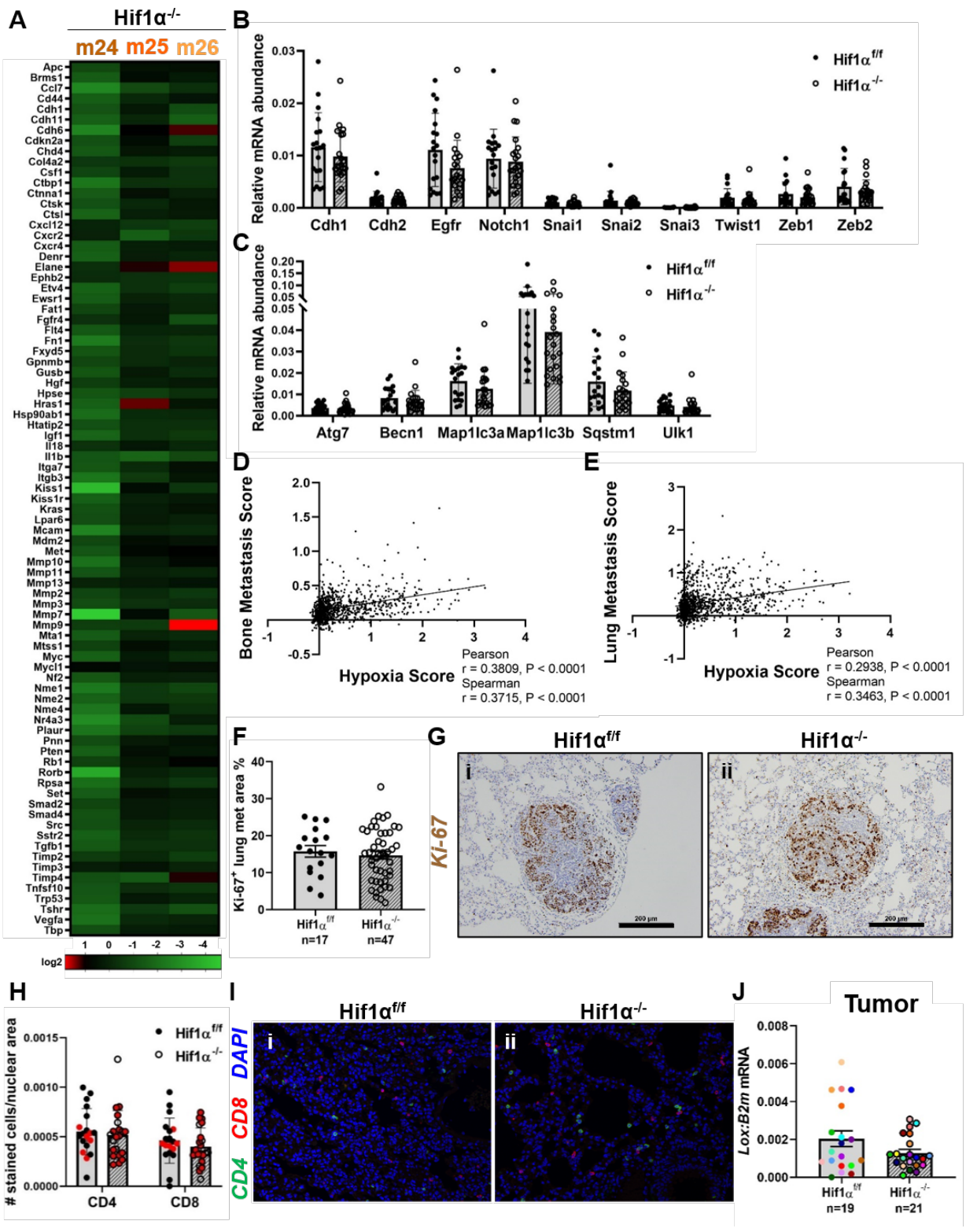
A
Hif1α-/-
m24 m25 m26
Apc
Brms1
Ccl7
Cd44
Cdh1
Cdh11
Cdh6
Cdkn2a
Chd4
Col4a2
Csf1
Ctbp1
Ctnna1
Ctsk
Ctsl
Cxcl12
Cxcr2
Cxcr4
Denr
Elane
Ephb2
Etv4
Ewsr1
Fat1
Fgfr4
Flt4
Fn1
Fxyd5
Gpnmb
Gusb
Hgf
Hpse
Hras1
Hsp90ab1
Htatip2
Igf1
Il18
Il1b
Itga7
Itgb3
Kiss1
Kiss1r
Kras
Lpar6
Mcam
Mdm2
Met
Mmp10
Mmp11
Mmp13
Mmp2
Mmp3
Mmp7
Mmp9
Mta1
Mtss1
Myc
Mycl1
Nf2
Nme1
Nme2
Nme4
Nr4a3
Plaur
Pnn
Pten
Rb1
Rorb
Rpsa
Set
Smad2
Smad4
Src
Sstr2
Tgfb1
Timp2
Timp3
Timp4
Tnfsf10
Trp53
Tshr
Vegfa
Tbp
1 0 -1 -2 -3 -4
log2
B
Relative mRNA abundance
0.03
0.02
0.01
0.00
Hif1α f/f
Hif1α -/-
Cdh1 Cdh2 Egfr Notch1 Snai1 Snai2 Snai3 Twist1 Zeb1 Zeb2
C
Relative mRNA abundance
0.20
0.15
0.10
0.05
0.05
0.04
0.03
0.02
0.01
0.00
Hif1α f/f
Hif1α -/-
Atg7 Becn1 Map1lc3a Map1lc3b Sqstm1 Ulk1
D
Bone Metastasis Score
2.0
1.5
1.0
0.5
-0.5
-1 1 2 3 4
Hypoxia Score
Pearson
r = 0.3809, P < 0.0001
Spearman
r = 0.3715, P < 0.0001
E
Lung Metastasis Score
3
2
1
-1
-1 1 2 3 4
Hypoxia Score
Pearson
r = 0.2938, P < 0.0001
Spearman
r = 0.3463, P < 0.0001
F
Ki-67+ lung met area %
40
30
20
10
0
Hif1α f/f
n=17
Hif1α -/-
n=47
G
Hif1α f/f
Hif1α -/-
Ki-67
i
ii
200 µm
200 µm
H
stained cells/nuclear area
0.0015
0.0010
0.0005
0.0000
Hif1α f/f
Hif1α -/-
CD4 CD8
I
Hif1α f/f
Hif1α -/-
i
ii
DAPI
CD8
CD4
J
Tumor
Lox:B2m mRNA
0.008
0.006
0.004
0.002
0.000
Hif1α f/f
n=19
Hif1α -/-
n=21

Figure 15. Hypoxia correlates with pro-metastatic transcription signatures. (A) Heatmap depiction of the expression of a panel of metastasis-associated gene from three Hif1α$^{-/-}$ tumors compared to the average expression of three Hif1α$^{f/f}$ tumors. The difference in expression of each gene between the three Hif1α$^{f/f}$ and three Hif1α$^{-/-}$ tumors was compared using the Mann-Whitney test. (**B)** Expression of a panel of EMT-related genes (*Cdh1, Cdh2, Egfr, Notch1, Snai1, Snai2, Snai3, Twist1, Zeb1, Zeb2*) compared to *B2m*, measured by qPCR. Two-tailed Mann-Whitney test against corresponding f/f control. **(C)** Expression of a panel of autophagy-related genes (*Atg7, Becn1, Map1lc3a, Map1lc3b, Sqstm1, Ulk1*) compared to *B2m*, measured by qPCR. Two-tailed Mann-Whitney test against corresponding f/f control. **(D, E)** Correlation of Ye *et al.* hypoxia gene signature [322] with mRNA levels of genes in the Kang *et al.* bone metastasis signature [305] or the Minn *et al.* lung metastasis signature [323], respectively, in TCGA Invasive Breast Carcinoma patient dataset. Pearson and Spearman correlation. **(F)** Quantification of Ki-67^{+} area as a percentage of the lesion area. Two-tailed Mann-Whitney test. **(G)** Representative images of Ki-67 stained lung metastatic lesions, taken with 20x objective. Scale bars represent 200 μm. **(H)** Quantification of the average number of CD4^{+} and CD8^{+} cells normalized to the total nuclear area for the image. Data points in red denote mice that had detectable lung tumor burden. Two-tailed Mann-Whitney test against corresponding f/f control. **(I)** Representative images of immunofluorescent staining of CD4 and CD8, taken with 20x objective. **(J)** Quantitative PCR analysis of *Lox* transcript compared to *B2m* from primary tumor homogenate RNA. Two-tailed Mann-Whitney test. Graph represents mean per group and error bars represent s.e.m.

Taken together, it appears that hypoxia upregulates tumor dissemination in general at the transcriptomic level, suggesting that the increase in lung tumor burden may be due to altered Hif1α$^{-/-}$ tumor cell response to signals from the lung microenvironment.

Proliferation and immune markers are unaltered in lung metastatic Hif1α$^{-/-}$ lesions. To reconcile the divergent role of *Hif1α* in tumor cell dissemination to bone and lung, we therefore sought to identify factors that may specifically be driving outgrowth of tumor cells in the lung. Since there is evidence that hypoxia promotes tumor dormancy specifically in the lung [353], we investigated whether the increased lung tumor burden in Hif1α$^{-/-}$ PyMT^{+} mice was due to dormancy escape by the lung-disseminated tumor cells. First, we confirmed that there was no significant difference in pimonidazole-positive lung lesion area, indicating Hif1α$^{f/f}$ and Hif1α$^{-/-}$ tumor cells experience similar levels of hypoxia in the lung (Fig. 16A, B). There was, however, no difference in Ki-67^{+} lung lesion area between the groups, indicating that *Hif1α* expression does not alter the proliferative capacity of the disseminated cells once they exit dormancy (Fig. 15F, G). We next measured the abundance of CD4^{+} and CD8^{+} cells in the lungs, since altered immune cell numbers in the lung tissue may indicate differences in immune-mediated tumor cell clearance. However, there was no difference in CD4^{+} or CD8^{+} T cell infiltration in the lungs of Hif1α$^{f/f}$ PyMT^{+} and Hif1α$^{-/-}$ PyMT^{+} mice (Fig. 15H, I). Immune cell numbers were not significantly different between tumor bearing lungs of Hif1α$^{f/f}$ PyMT^{+} and Hif1α$^{-/-}$ PyMT^{+} mice, either (red points, Fig. 15H). To investigate whether pre-metastatic niche development could be driving the outgrowth of lung-disseminated tumor cells, we measured the expression of lysyl oxidase (LOX), a hypoxia-dependent tumor secreted factor known to drive pre-metastatic niche development [126]. However, there was no change in *Lox* expression between Hif1α$^{f/f}$ and Hif1α$^{-/-}$ tumors (Fig. 15J).

Deletion of Hif2α decreases tumor dissemination to bone but not lung. While Hif1α and Hif2α have some redundant functions, they have unique and sometimes opposing effects [354]. To determine whether the dissemination patterns observed in the Hif1α$^{-/-}$ PyMT^{+} mice were due to a general decrease in HIF signaling activity, or due to Hif1α-specific effects, we generated Hif2α$^{f/f}$ PyMT^{+} and Hif2α$^{-/-}$ PyMT^{+} mice using the same breeding strategy as the Hif1α$^{-/-}$ PyMT^{+} mice. We observed no difference between the Hif2α$^{f/f}$ PyMT^{+} and Hif2α$^{-/-}$ PyMT^{+} mice in the time it

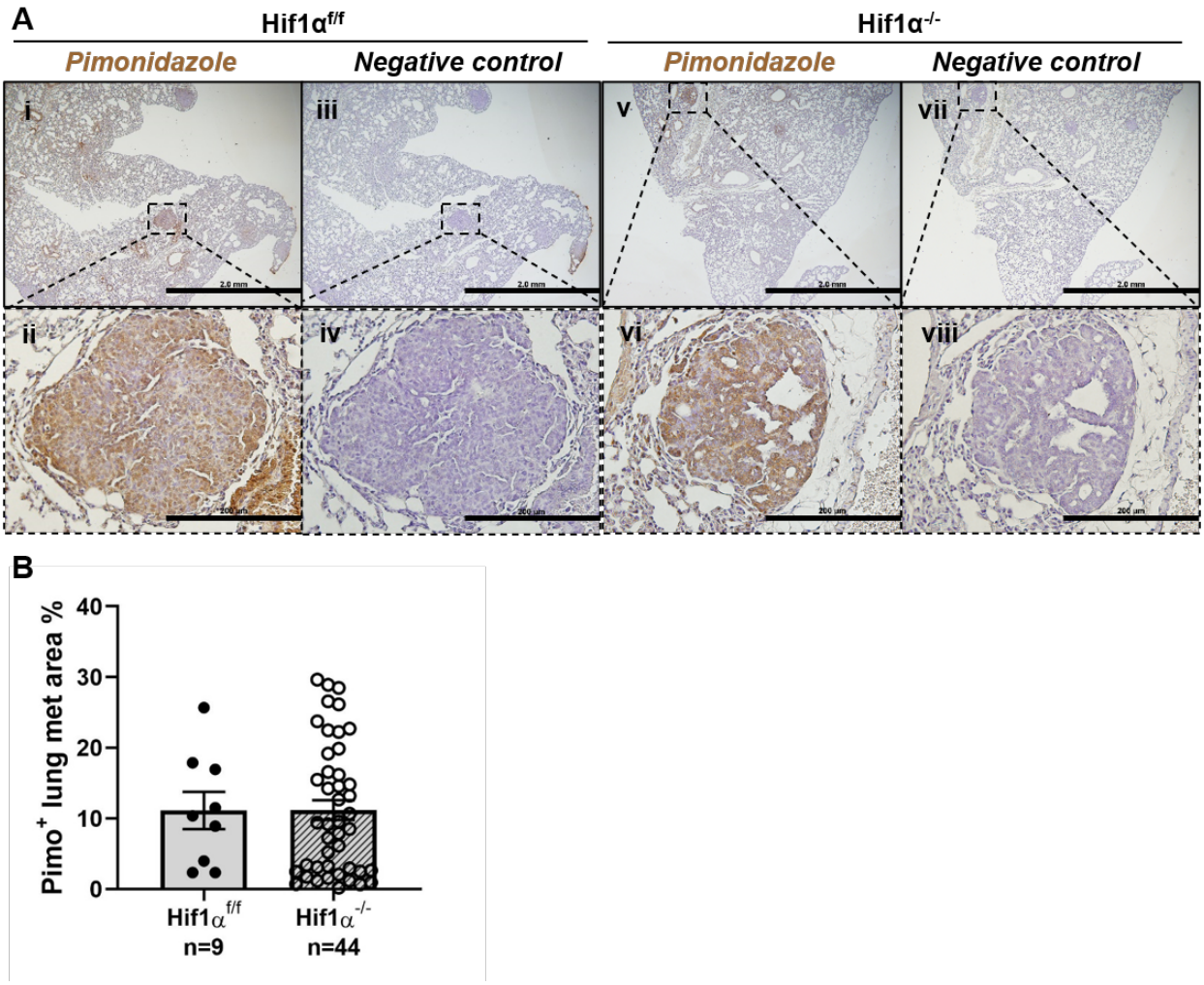

Figure 16. *Hif1α* deletion does not alter hypoxia of lung metastatic foci. (A) Representative images of pimonidazole staining, taken with 4x and 40x objectives. The 40x field is denoted with a dashed box in the 10x view. Scale bars represent 2 mm in 4x fields, and 200 μm in 40x fields. Negative controls lacked the primary antibody incubation step. **(B)** Quantification of pimonidazole-positive area as a percentage of the lesion area. Two-tailed Mann-Whitney test. Graphs represent mean per group and error bars represent s.e.m.

took tumors to reach collection size (Fig. 17A, B), the total tumor weight upon sacrifice (Fig. 17C), or the number of tumors (Fig. 17D). We confirmed a significant reduction in *Hif2α* transcript levels from whole tumor homogenate RNA of Hif2α$^{-/-}$ PyMT^{+} mice (Fig. 17E) and no difference in *Hif1α* transcript levels (Fig. 17F). *Hif2α* deletion did not significantly reduce *Vegfa* expression in the primary tumor (Fig. 17G).

While microCT analysis of Hif2α$^{-/-}$ PyMT^{+} mice did not reveal any differences in trabecular bone parameters (Fig. 17H-L), flow cytometry analysis of hindlimb bone marrow from Hif2α$^{-/-}$ PyMT^{+} mice revealed a significant reduction in the percentage of EpCAM^{+} tumor cells (Fig. 18A). However, there was no significant difference in the *Pymt* transcript abundance in the femur or spine (Fig. 18B, C). Unlike the Hif1α$^{-/-}$ PyMT^{+} mice, lung metastatic tumor burden in Hif2α$^{-/-}$ PyMT^{+} mice was not significantly different than Hif2α$^{f/f}$ PyMT^{+} mice, as measured by lesion number, total lesion area, individual lesion area, or incidence of lung metastases (Fig. 18D-G). Similarly, there was no significant difference in *Pymt* transcript abundance in the lungs or brains of Hif2α$^{-/-}$ PyMT^{+} mice (Fig. 18H, I). Metastatic tumor burden data for Hif2α$^{-/-}$ PyMT^{+} mice were un-normalized since there was no significant difference in tumor weight or age at sacrifice. Taken together, these results suggest that *Hif2α* in the primary tumor drives tumor cell dissemination to the bone but is dispensable for dissemination to the lung.

Deletion of Vhl increases tumor dissemination to bone but not lung. To determine the effect of Hif1α and Hif2α activation, rather than deletion, we generated a third transgenic mouse strain in which we could model constitutive HIF signaling activation through deletion of Vhl, a negative regulator of HIF signaling. Vhl$^{f/f}$ PyMT^{+} and Vhl$^{-/-}$ PyMT^{+} mice were generated using the same strategy as the other transgenic strains. Vhl$^{-/-}$ tumors took a significantly longer time to reach collection size compared to Vhl$^{f/f}$ controls (Fig. 19A, B), but had a significant reduction in total tumor weight upon sacrifice (Fig. 19C). The average number of tumors was not significantly different between Vhl$^{f/f}$ PyMT^{+} and Vhl$^{-/-}$ PyMT^{+} mice (Fig. 19D). While we were unable to detect a decrease in *Vhl* transcript in whole tumor RNA from Vhl$^{-/-}$ PyMT^{+} mice (Fig. 19E), we confirmed recombination of the *Vhl* locus at the genomic level (Fig. 19F) and observed a significant increase in expression of vascular endothelial growth factor A (*Vegfa*), phosphoglycerate kinase 1 (*Pgk1*), glucose transporter type 1 (*Glut1*), TEK receptor tyrosine

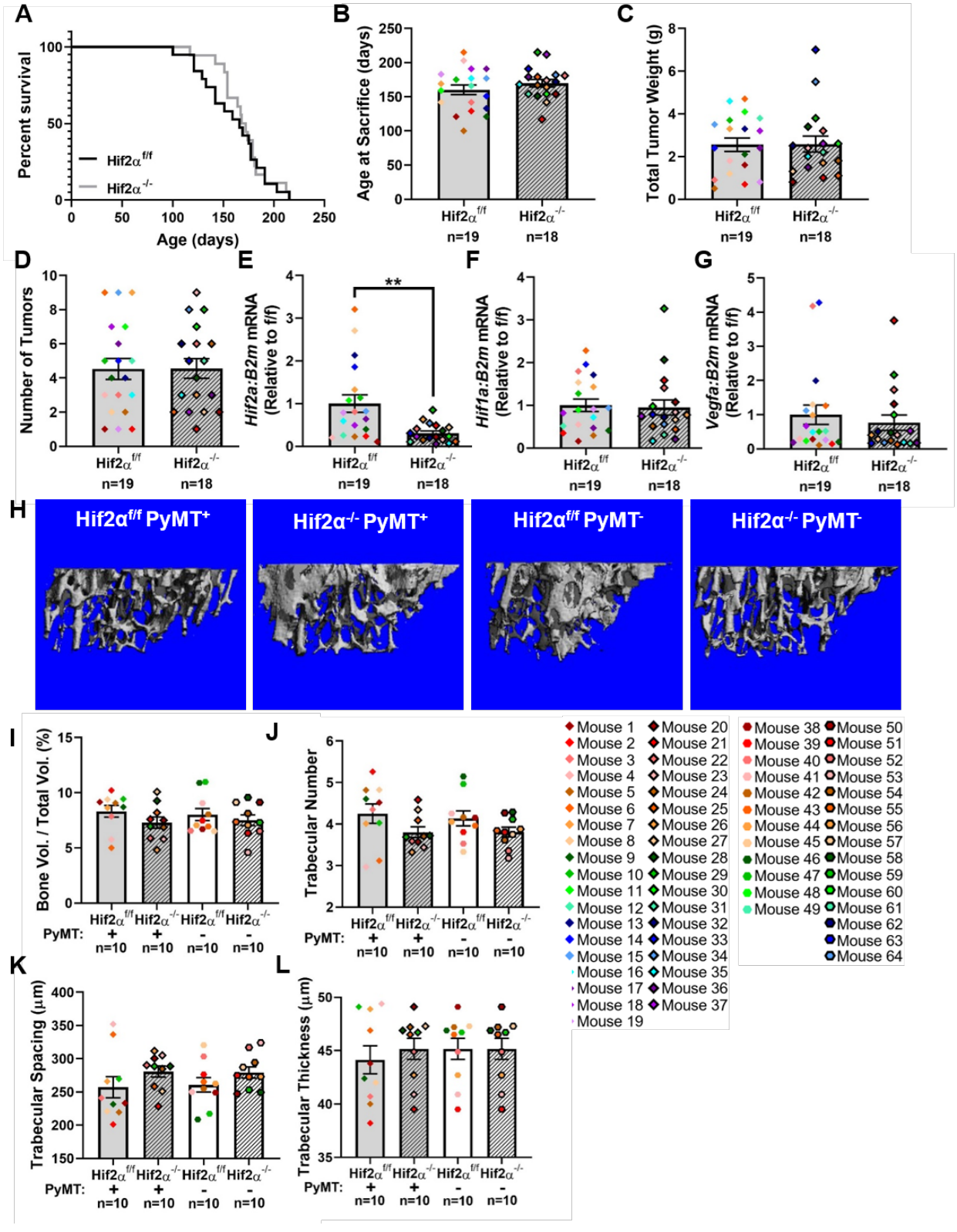
A
Percent survival
Hif2α f/f
Hif2α -/-
Age (days)
B
Age at Sacrifice (days)
C
Total Tumor Weight (g)
n=19
n=18
D
Number of Tumors
E
Hif2a:B2m mRNA (Relative to f/f)
**
F
Hif1a:B2m mRNA (Relative to f/f)
G
Vegfa:B2m mRNA (Relative to f/f)
H
Hif2α f/f PyMT+
Hif2α -/- PyMT+
Hif2α f/f PyMT-
Hif2α -/- PyMT-
I
Bone Vol. / Total Vol. (%)
J
Trabecular Number
PyMT:
n=10
K
Trabecular Spacing (µm)
L
Trabecular Thickness (µm)
Mouse 1
Mouse 2
Mouse 3
Mouse 4
Mouse 5
Mouse 6
Mouse 7
Mouse 8
Mouse 9
Mouse 10
Mouse 11
Mouse 12
Mouse 13
Mouse 14
Mouse 15
Mouse 16
Mouse 17
Mouse 18
Mouse 19
Mouse 20
Mouse 21
Mouse 22
Mouse 23
Mouse 24
Mouse 25
Mouse 26
Mouse 27
Mouse 28
Mouse 29
Mouse 30
Mouse 31
Mouse 32
Mouse 33
Mouse 34
Mouse 35
Mouse 36
Mouse 37
Mouse 38
Mouse 39
Mouse 40
Mouse 41
Mouse 42
Mouse 43
Mouse 44
Mouse 45
Mouse 46
Mouse 47
Mouse 48
Mouse 49
Mouse 50
Mouse 51
Mouse 52
Mouse 53
Mouse 54
Mouse 55
Mouse 56
Mouse 57
Mouse 58
Mouse 59
Mouse 60
Mouse 61
Mouse 62
Mouse 63
Mouse 64

Figure 17. Deletion of *Hif2α* does not alter total tumor burden, tumor growth kinetics, or trabecular bone parameters. (A) Survival analysis of Hif2α$^{f/f}$ PyMT^{+} and Hif2α$^{-/-}$ PyMT^{+} mice where endpoint represents sacrifice due to tumor size reaching collection threshold. Log-rank test. **(B-D)** Comparison of the age at sacrifice, total burden at sacrifice, and number of tumors collected per mouse. Two-tailed Mann-Whitney test. (**E-G)** Quantitative PCR analysis of *Hif2α, Hif1α,* and *Vegfa* expression compared to *B2m* from whole tumor homogenate RNA. Expression is normalized to the mean of the f/f control group. Two-tailed Mann-Whitney test. **(H)** Representative 3D renderings of microCT scans of the proximal metaphysis of the right tibia. (**I-L)** Quantification of bone volume as a percentage of total volume, trabecular number, trabecular spacing, and trabecular thickness. Two-tailed Mann-Whitney test against corresponding f/f control. Graphs represent mean per group and error bars represent s.e.m. **P < 0.01.

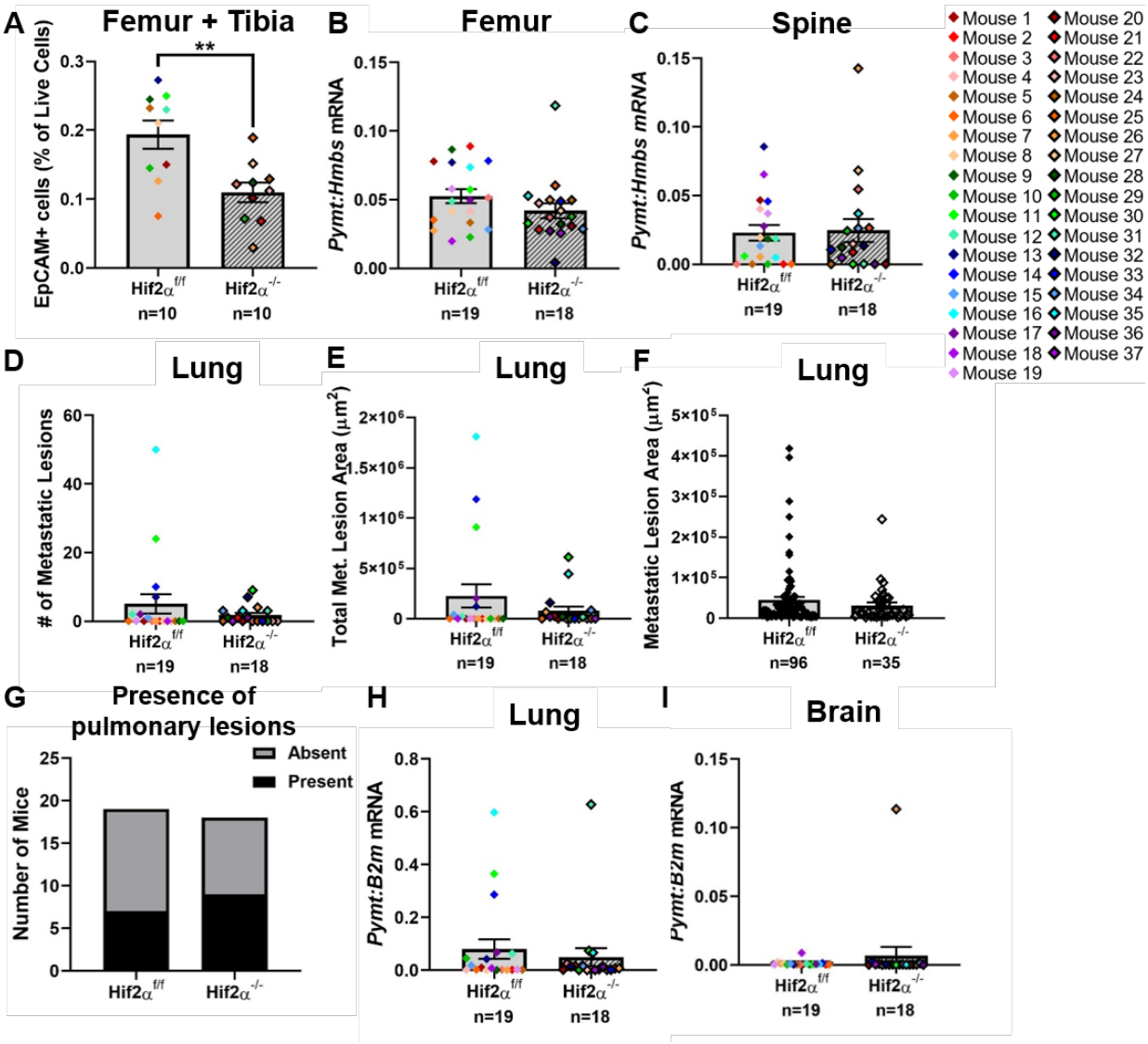

Figure 18. Deletion of *Hif2α* decreases tumor dissemination to bone but not lung. (A) The percentage of EpCAM$^+$ cells, out of the total number of live cells, detected by flow cytometry analysis of left hindlimb bone marrow. Two-tailed Mann-Whitney test. **(B, C)** Quantitative PCR analysis of *Pymt* transcript compared to *Hmbs* from right femur or spinal midsection, respectively. Two-tailed Mann-Whitney test. **(D, E)** Metastatic lesion number or area detected by histological analysis of H&E stained sections from the left lung. Two-tailed Mann-Whitney test. **(F)** Comparison of individual lesion areas detected from histological inspection of left lung sections. Two-tailed Mann-Whitney test. **(G)** Comparison of the proportion of mice from each group that had any detectable pulmonary lesions. Fisher's exact test. **(H, I)** Quantitative PCR analysis of *Pymt* transcript compared to *B2m* from right lung or brain, respectively. Two-tailed Mann-Whitney test. Graphs represent mean per group and error bars represent s.e.m. **P < 0.01.

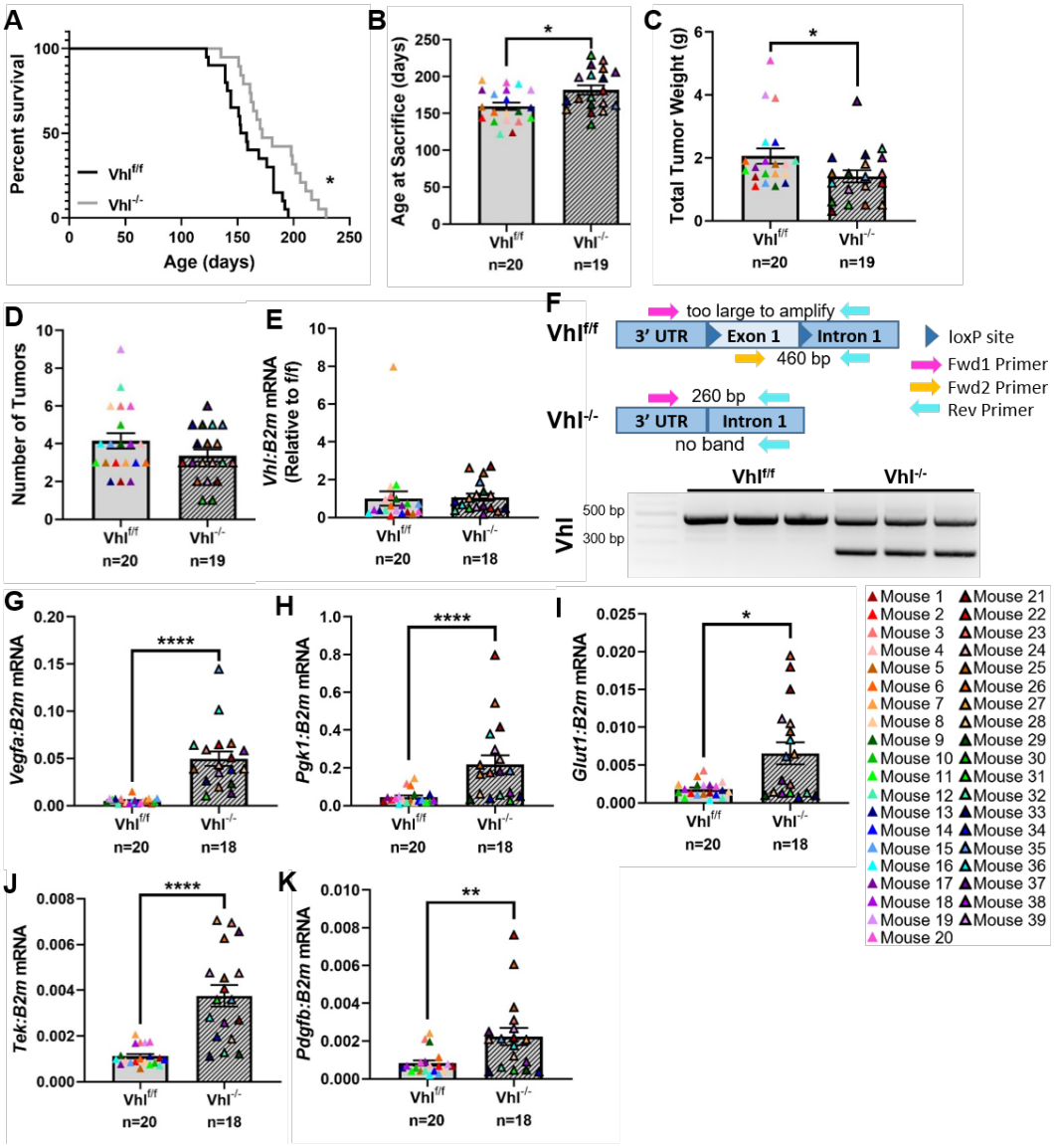

Figure 19. Deletion of *Vhl* slows primary tumor growth and decreases total tumor burden but does not alter trabecular bone parameters. (A) Survival analysis of $Vhl^{f/f}$ and $Vhl^{-/-}$ $PyMT^{+}$ mice where endpoint represents sacrifice due to tumor size reaching collection threshold. Log-rank test. **(B-D)** Comparison of the age at sacrifice, total burden at sacrifice, and number of tumors collected per mouse. Two-tailed Mann-Whitney test. **(E)** Quantitative PCR analysis of *Vhl* expression compared to *B2m* from whole tumor homogenate RNA. Expression is normalized to the mean of the f/f control group. Two-tailed Mann-Whitney test. **(F)** Schematic of PCR-based validation of *Vhl* locus recombination using a three-primer PCR reaction. Genomic DNA was used as the input material. DNA electrophoresis gel represents the PCR products from the reactions depicted in the schematic diagram. The lower molecular weight of the band in the $Vhl^{-/-}$ lanes indicate successful recombination. The residual band in the $Vhl^{-/-}$ lanes are likely from non-recombined stromal cells present in the tumor. **(G-K)** Quantitative PCR analysis of HIF target genes (*Vegfa, Pgk1, Glut1, Tek, Pdgfb)* compared to *B2m* from whole tumor homogenate RNA. Two-tailed Mann-Whitney test. Graphs represent mean per group and error bars represent s.e.m. *P < 0.05, **P < 0.01, ***P < 0.001, ****P < 0.0001.

kinase (*Tek,* also known as Tie2)*,* and platelet derived growth factor subunit B (*Pdgfb*) (Fig. 19G-K), indicating that HIF downstream signaling is elevated with *Vhl* deletion. Despite unaltered trabecular bone parameters (Fig. 20A, B, Fig. 21A-C), *Vhl* deletion increased the number of tumor cells detected in the bone marrow by flow cytometry when normalized to tumor weight (Fig. 20C, Fig. 21D). No significant differences were observed in the *Pymt* transcript abundance in the femur or spine (Fig. 20D, E, Fig. 21E, F). From histological analysis of the lung, no significant differences were observed in total metastatic lesion number or area between $Vhl^{f/f}$ $PyMT^{+}$ and $Vhl^{-/-}$ $PyMT^{+}$ mice, regardless of normalization to total primary tumor weight (Fig. 20F, G, Fig. 21G, H). In addition, the incidence of lung metastases was no different between the two groups (Fig. 20H). There was a slight increase in the average individual lung lesion size in the $Vhl^{-/-}$ $PyMT^{+}$ mice (Fig. 21I), but this difference was not sufficient to drive an increase in the overall lung tumor burden. Additionally, there were no significant differences in *Pymt* transcript abundance in the lungs or brains of $Vhl^{-/-}$ $PyMT^{+}$ mice (Fig. 20I, J, Fig. 21J, K).

While *Hif1α* deletion was not found to alter the expression of genes involved in specific metastasis-related signaling pathways (Fig. 15), *Vhl* deletion was found to increase, although not significantly, the expression of *Pthlh* in the primary tumor (Fig. 22A). *PTHLH* and its gene product PTHrP are known to promote breast tumor progression and metastasis [355] and are key drivers of tumor induced bone disease [165, 356, 357]. Additionally, *PTHLH* is a direct target of HIF2α [167]. Accordingly, we observed that *Hif2α*, but not *Hif1α*, deletion drove a noticeable decrease in *Pthlh* expression (Fig. 22B, C). *Vhl* deletion also modestly increased the expression of *Cxcr4* (Fig. 22D), a gene known to drive breast cancer cell metastasis to bone [136, 358]. *Hif1α* deletion did not result in a reciprocal decrease in *Cxcr4* expression, but *Hif2α* deletion yielded a non-significant decrease in *Cxcr4* (Fig. 22E, F). Taken together, these results suggest that active HIF-signaling in the primary tumor drives tumor cell dissemination to the bone through HIF-induced expression of key metastasis-associated genes (Fig. 22G).

Discussion

While our main analysis was focused on dissemination patterns and quantifying tumor burden in various distant sites, we observed surprising patterns in primary tumor growth. The slower tumor progression we observed in the $Hif1\alpha^{-/-}$ tumors has been reported previously in this mode [94],

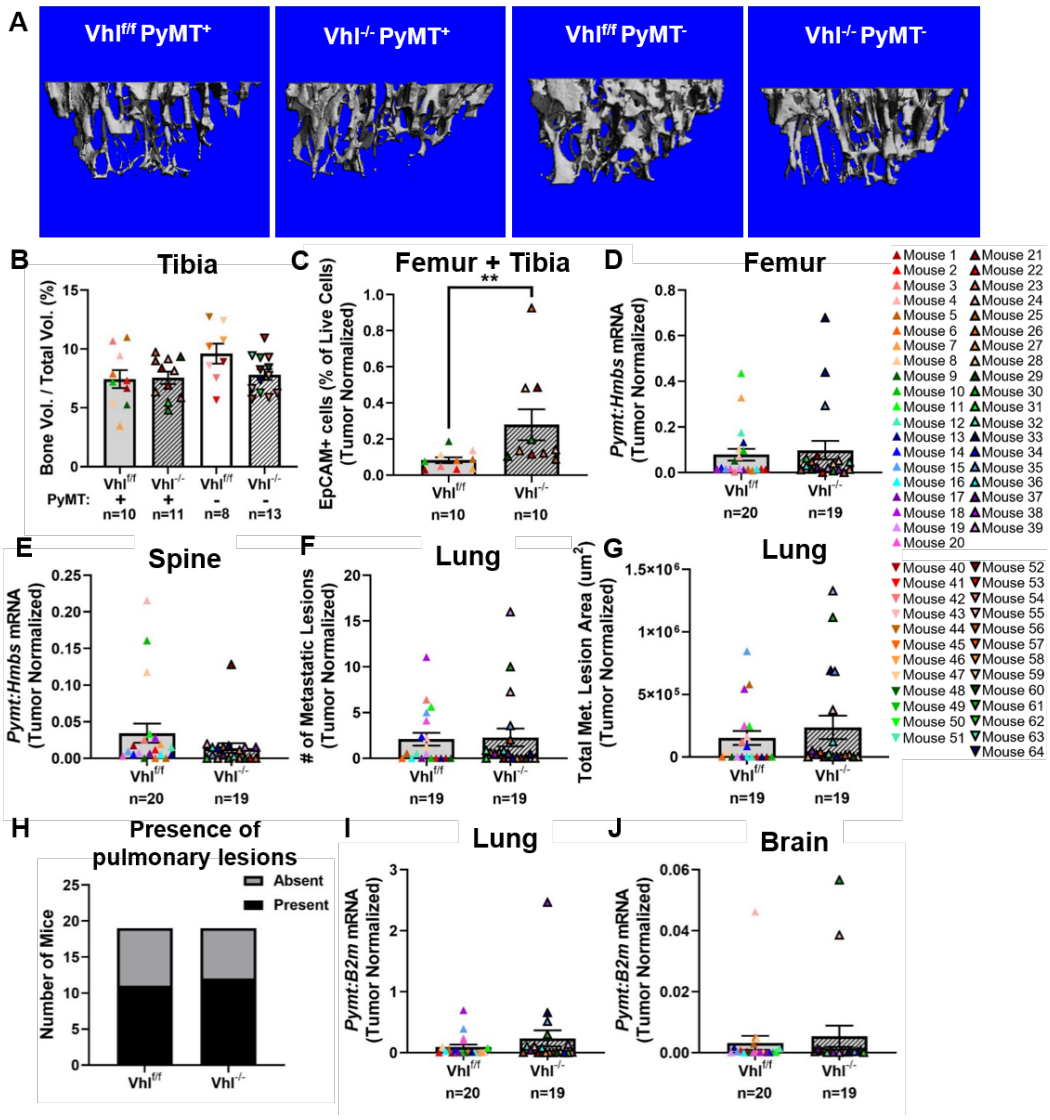

Figure 20. Deletion of *Vhl* increases tumor dissemination to bone but not lung. (A) Representative 3D renderings of microCT scans of the proximal metaphysis of the right tibia. **(B)** Quantification of bone volume from microCT analysis as a percentage of total volume. Two-tailed Mann-Whitney test against corresponding f/f control. **(C)** The percentage of EpCAM^{+} cells, out of the total number of live cells, detected by flow cytometry analysis of left hindlimb bone marrow. Values have been normalized to the total tumor burden at end point of each mouse. Two-tailed Mann-Whitney test. **(D, E)** Quantitative PCR analysis of *Pymt* transcript compared to *Hmbs* from right femur or spinal midsection, respectively. Values have been normalized to the total tumor burden at end point of each mouse. Two-tailed Mann-Whitney test. **(F, G)** Metastatic lesion number or area detected by histological analysis of H&E stained sections from the left lung. Values have been normalized to the total tumor burden at end point of each mouse. Two-tailed Mann-Whitney test. **(H)** Comparison of the proportion of mice from each group that had any detectable pulmonary lesions. Fisher's exact test. **(I, J)** Quantitative PCR analysis of *Pymt* transcript compared to *B2m* from right lung or brain, respectively. Values have been normalized to the total tumor burden at end point of each mouse. Two-tailed Mann-Whitney test. Graphs represent mean per group and error bars represent s.e.m. **P < 0.01.

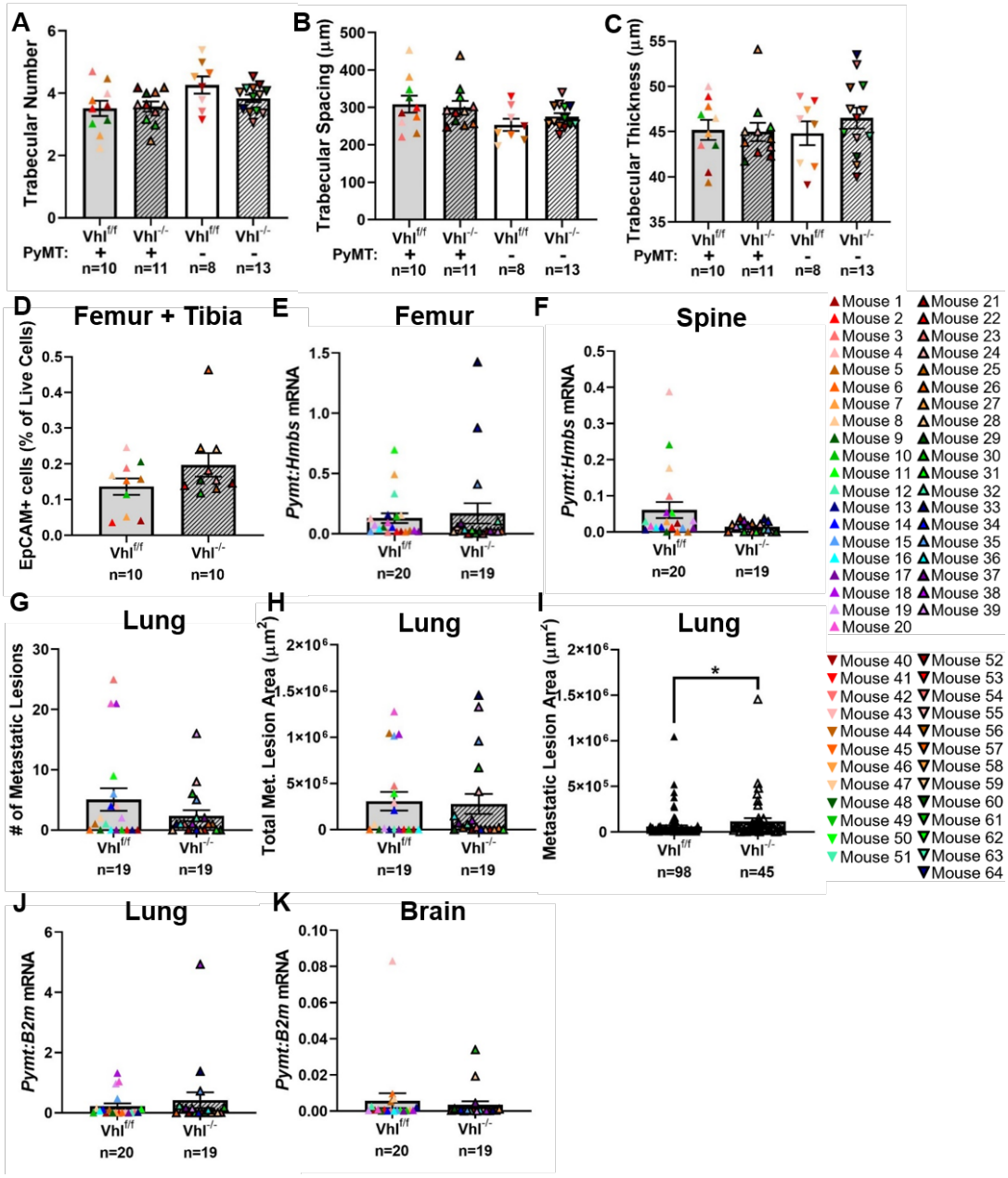

Figure 21. Un-normalized tumor burden in bone and soft tissue sites from *Vhl* knockout mice. (A-C) Quantification of trabecular number, trabecular spacing, and trabecular thickness from microCT analysis of proximal tibia. Two-tailed Mann-Whitney test against corresponding f/f control. **(D)** The percentage of EpCAM$^+$ cells, out of the total number of live cells, detected by flow cytometry analysis of left hindlimb bone marrow. Two-tailed Mann-Whitney test. **(E, F)** Quantitative PCR analysis of *Pymt* transcript compared to *Hmbs* from right femur or spinal midsection, respectively. Two-tailed Mann-Whitney test. **(G, H)** Total metastatic lesion number or area detected by histological analysis of H&E stained sections from the left lung. Two-tailed Mann-Whitney test. **(I)** Comparison of individual lesion areas detected from histological inspection of left lung sections. Two-tailed Mann-Whitney test. **(J, K)** Quantitative PCR analysis of *Pymt* transcript compared to *B2m* from right lung or brain, respectively. Two-tailed Mann-Whitney test. Graphs represent mean per group and error bars represent s.e.m.

and has been attributed to delayed microvessel growth in the mammary fat pad due to insufficient HIF-signaling. Interestingly, while tumor progression is delayed, total tumor weight was higher on average in Hif1α$^{-/-}$ PyMT^{+} mice than Hif1α$^{f/f}$ PyMT^{+} mice. However, in the previous study using this model [94], no significant difference in tumor weight at end point was noted. In contrast to *Hif1α*, our data indicate that *Hif2α* deletion does not significantly alter tumor progression, suggesting that HIF1α and HIF2α target distinct pathways that regulate tumor growth. Interestingly, while we expected *Vhl* deletion to yield the opposite tumor growth pattern from *Hif1α* deletion and cause tumors to grow more rapidly, *Vhl* deleted tumors in fact progressed more slowly. VHL deletion has been reported to increase immune infiltration in mammary tumors [359], which may contribute to increased tumor cell clearance and the slower tumor growth and decreased total tumor weight observed in the Vhl$^{-/-}$ PyMT^{+} mice.

Our finding that bone metastasis was significantly lower with *Hif1α* or *Hif2α* deletion are highly consistent with previous studies demonstrating that hypoxic signaling promotes tumor cell dissemination to the bone. HIF1α expression in breast cancer cells promotes bone colonization and osteolysis following intracardiac or orthotopic inoculation of MDA-MB-231 human breast cancer cells [93, 96, 97], and hypoxic transcriptomic signatures in breast cancer cells has been associated with bone metastasis [92, 143].

It is important to note that our lung metastasis findings, which indicate Hif1α inhibits lung metastasis while Hif2α has no effect, contradicts a large body of work that demonstrates both Hif1α and Hif2α promote lung metastasis. A prior study using the genetic MMTV-PyMT mouse model with mammary-specific deletion of Hif1α indicated that Hif1α expression promoted lung metastasis [94]. The reason for the differences in our findings from previous studies are likely multifaceted. We used similar methodology, and we had a board-certified, blinded veterinary pathologist perform the lung tumor analysis. It is possible that the differences may be due to differences in genetic strain, since the combination of these mice is on a mixed genetic background. Our colony is therefore genetically distinct from the previous study. Significant differences have also been noted in microbiome composition of genetically engineered mice with the same genotype housed at different facilities [360]. The commensal microbiota can significantly impact both local (gut) and systemic immunity [361, 362] and thus could also influence the clearance or growth of disseminated tumor cells. Minor variations in

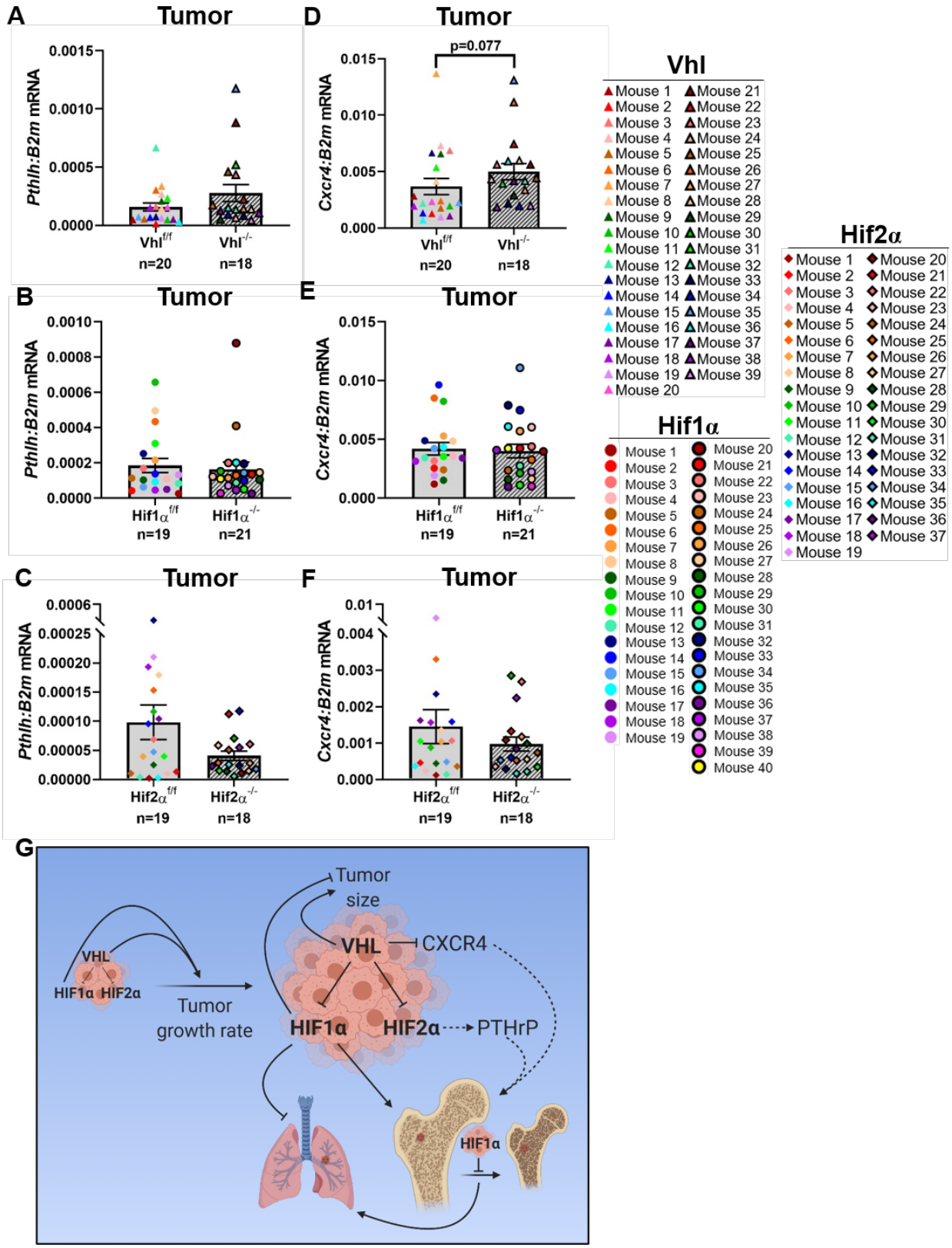
A
Tumor
Pthlh:B2m mRNA
0.0015
0.0010
0.0005
0.0000
Vhl f/f
Vhl -/-
n=20
n=18
D
Tumor
p=0.077
Cxcr4:B2m mRNA
0.015
0.010
0.005
0.000
Vhl f/f
Vhl -/-
n=20
n=18
Vhl
Mouse 1
Mouse 2
Mouse 3
Mouse 4
Mouse 5
Mouse 6
Mouse 7
Mouse 8
Mouse 9
Mouse 10
Mouse 11
Mouse 12
Mouse 13
Mouse 14
Mouse 15
Mouse 16
Mouse 17
Mouse 18
Mouse 19
Mouse 20
Mouse 21
Mouse 22
Mouse 23
Mouse 24
Mouse 25
Mouse 26
Mouse 27
Mouse 28
Mouse 29
Mouse 30
Mouse 31
Mouse 32
Mouse 33
Mouse 34
Mouse 35
Mouse 36
Mouse 37
Mouse 38
Mouse 39
B
Tumor
Pthlh:B2m mRNA
0.0010
0.0008
0.0006
0.0004
0.0002
0.0000
Hif1α f/f
Hif1α -/-
n=19
n=21
E
Tumor
Cxcr4:B2m mRNA
0.015
0.010
0.005
0.000
Hif1α f/f
Hif1α -/-
n=19
n=21
Hif1α
Mouse 1
Mouse 2
Mouse 3
Mouse 4
Mouse 5
Mouse 6
Mouse 7
Mouse 8
Mouse 9
Mouse 10
Mouse 11
Mouse 12
Mouse 13
Mouse 14
Mouse 15
Mouse 16
Mouse 17
Mouse 18
Mouse 19
Mouse 20
Mouse 21
Mouse 22
Mouse 23
Mouse 24
Mouse 25
Mouse 26
Mouse 27
Mouse 28
Mouse 29
Mouse 30
Mouse 31
Mouse 32
Mouse 33
Mouse 34
Mouse 35
Mouse 36
Mouse 37
Mouse 38
Mouse 39
Mouse 40
C
Tumor
Pthlh:B2m mRNA
0.0006
0.00025
0.00020
0.00015
0.00010
0.00005
0.00000
Hif2α f/f
Hif2α -/-
n=19
n=18
F
Tumor
Cxcr4:B2m mRNA
0.01
0.004
0.003
0.002
0.001
0.000
Hif2α f/f
Hif2α -/-
n=19
n=18
Hif2α
Mouse 1
Mouse 2
Mouse 3
Mouse 4
Mouse 5
Mouse 6
Mouse 7
Mouse 8
Mouse 9
Mouse 10
Mouse 11
Mouse 12
Mouse 13
Mouse 14
Mouse 15
Mouse 16
Mouse 17
Mouse 18
Mouse 19
Mouse 20
Mouse 21
Mouse 22
Mouse 23
Mouse 24
Mouse 25
Mouse 26
Mouse 27
Mouse 28
Mouse 29
Mouse 30
Mouse 31
Mouse 32
Mouse 33
Mouse 34
Mouse 35
Mouse 36
Mouse 37
G
Tumor size
VHL
CXCR4
HIF1α HIF2α
Tumor growth rate
HIF1α
HIF2α
PTHrP
HIF1α

Figure 22. VHL and HIF signaling drives *Cxcr4* and *Pthlh* in the primary tumor. (A-C) Quantitative PCR analysis of *Cxcr4* transcript compared to *B2m* in primary tumor with deletion of *Vhl*, *Hif1α,* or *Hif2α*, respectively. Two-tailed Mann-Whitney test. **(D-F)** Quantitative PCR analysis of *Pthlh* transcript compared to *B2m* in primary tumor with deletion of *Vhl*, *Hif1α,* or *Hif2α*, respectively. Two-tailed Mann-Whitney test. **(G)** Summary of findings. VHL and HIF1α expression in the primary tumor drive tumor growth, and VHL expressing tumors are larger, while HIF1α expressing tumors are smaller on average. VHL in the primary tumor inhibits CXCR4 expression, inhibiting bone metastasis. HIF2α drives the expression of PTHrP, which promotes tumor dissemination to bone. HIF1α expression in the primary tumor also disrupts bone homeostasis, leading to decreased bone volume. This disruption of the bone inhibits tumor cell dissemination to bone, while likely promoting tumor cells dissemination and outgrowth in the lung. Dashed arrows represent proposed or potential mechanisms. Graphs represent mean per group and error bars represent s.e.m.

animal handling and housing conditions, such as cage density and diet, have also been shown to affect biochemical, hematological, metabolic, and endocrine parameters [363].

Additional studies similarly indicate that increased HIF signaling increases metastasis, including a 45-gene hypoxia response gene signature that was predictive of breast cancer patients' risk of developing lung metastases [93]. Several studies using MDA-MB-231 human breast cancer cells or EMT6 murine mammary carcinoma cells have also demonstrated that inhibition of HIF1α or HIF2α significantly diminishes metastasis to the lung [93, 364, 365]. HIF signaling has been shown to facilitate tumor cell extravasation by driving the expression of genes that increase breast cancer cell adhesion to endothelial cells, such as L1 cell adhesion molecule (L1CAM), as well as genes that decrease adhesion between endothelial cells, such as angiopoietin-like 4 (ANGPTL4) [364]. Specific downstream effectors of HIF signaling that prepare the lung microenvironment for metastatic colonization, such as LOX and LOX like proteins (LOXL2 and LOXL4), have also been identified [50, 366]. A potential explanation for the difference in findings from these prior studies may be due to our use of a spontaneous tumor formation and dissemination model since the majority of the previous studies utilized xenograft or syngeneic injection models, or may be due to differences between PyMT tumor cells and the tumor lines utilized in the other studies. It is possible that since the PyMT-driven spontaneous mammary cancer model has such a robust lung metastasis phenotype, contributions of HIF signaling may be negligible. This would explain why we do not see changes in lung tumor burden in the Hif2α- or Vhl-deletion models, and could point to a yet unidentified mechanism at play in the Hif1α-deletion strain that exhibited increased lung metastasis.

Thus far we have not been able to identify a molecular driver for the increased lung metastasis observed with *Hif1α* deletion, and have eliminated a significant number of potential mechanisms. We demonstrated that *Hif1α* expression does not alter the proliferative capacity of macroscopic lung lesions, but due to the collection time point we were not able to detect single disseminated tumor cells in these mice. As we collected mice relatively late in disease progression in order to maximize the amount of disseminated cells, the lung lesions were already well developed. Thus, we could not determine whether the proliferative capacity of these disseminated tumor cells was altered by *Hif1α* expression prior to their development into histologically detectable lesions. We cannot rule out that disseminated tumor cells that had not yet grown into macroscopic lesions are detectable in mice collected earlier in disease progression

and there may be differences in Ki-67 staining at that time point. Given the subtlety of our model and the large mouse numbers necessary for robust statistical analysis at earlier time points, it would be difficult to assess these differences earlier in the model. Importantly, normalizing lung tumor burden to age at sacrifice did not change our finding that *Hif1α* deletion increased lung metastasis, indicating that our data is likely not an artifact of the difference in collection age.

Additionally, this difference in outgrowth of disseminated tumor cells could be due to tumor cell intrinsic properties driven by *Hif1α* expression, or due to microenvironmental changes in the lung that result from *Hif1α* expression in the primary tumor. First, alterations in immune cell populations in the lung may alter the outgrowth of lung-metastatic cells due to immune-mediated tumor cell clearance [367]. We measured the presence of $CD4^+$ and $CD8^+$ cells in the lungs of $Hif1\alpha^{f/f}$ $PyMT^+$ and $Hif1\alpha^{-/-}$ $PyMT^+$ mice but observed no differences. However, other immune cell types are also involved in tumor cell clearance. Modulating the activity or polarization of immune cells is also known to create microenvironments that oppose or support tumor growth. For example, T cell inactivation is known to create a permissive microenvironment for tumor growth [368], and tumor-associated macrophages can promote tumor progression through many pathways, such as inducing tissue remodeling and fibrosis, taming of adaptive immunity, and providing protective niches for cancer stem cells [369]. Some immune cell types, especially $CD11b^+$ cells, have been implicated in the establishment of the pre-metastatic niche [126, 370] that fosters tumor cell growth. Thus, a more extensive immune cell profiling of the lung may reveal differences that would explain the difference in tumor cell outgrowth. Second, primary tumor secreted factors have been shown to affect the establishment of a pre-metastatic niche. Hypoxia-induced LOX secretion from breast cancer cells is a driver of pre-metastatic niche development in the lung [126] as well as osteolytic lesion development in the bone [142, 143]. While we did not observe a difference in *Lox* expression that would explain the increased lung tumor burden and decreased bone volume observed in $Hif1\alpha^{-/-}$ $PyMT^+$ mice, this is not the only factor that regulates pre-metastatic niche development. In prostate cancer, exosomes released from hypoxic cancer cells have been shown to promote matrix metalloproteinase activity at pre-metastatic sites [371]. The mechanisms that govern pre-metastatic niche development at various anatomical sites is not yet well characterized, and the impact of hypoxia on this process warrants further investigation.

Interestingly, a change in lung tumor burden was only observed in the *Hif1α* deleted mice, and not in the *Hif2α* or *Vhl* deleted mice. Of note, a decrease in tibial bone volume was observed in the Hif1α$^{-/-}$ PyMT^{+} mice, but not in the *Hif2α* or *Vhl* deleted mice. The osteogenic niche is key to the establishment and growth of disseminated tumor cells in the bone marrow, as the interaction of tumor cells with osteoblast lineage cells through heterotypic adherens junctions activates pro-proliferation pathways [253]. However, osteoblast-secreted factors have also been shown to induce dormancy and quiescence in prostate cancer cells [372, 373], indicating that the osteogenic niche can promote quiescence of tumor cells that engraft in these regions of the bone. Since the osteogenic niche is reduced in the Hif1α$^{-/-}$ PyMT^{+} mice, as indicated by the reduction in bone volume, the shrinkage of suitable niches available for tumor cell engraftment in bone may cause a larger portion of the metastatic tumor cells to engraft in the lung instead. This may explain why we do not observe a difference in lung tumor burden in *Hif2α* or *Vhl* deleted mice. The mechanism behind the decreased bone volume in Hif1α$^{-/-}$ PyMT^{+} mice remains unclear; however, it is important to note that there was no difference in bone volume between Hif1α$^{f/f}$ and Hif1α$^{-/-}$ PyMT^{-} mice, suggesting that the reduction in bone volume is not due to deletion of *Hif1α* in off-target cell lineages, but rather due to the presence of tumor.

While a loss of the osteogenic niche could explain the reduction in bone dissemination and increase in lung metastasis observed in the Hif1α$^{-/-}$ PyMT^{+} mice, other mechanisms must be involved in the bone dissemination phenotypes we observed in Hif2α$^{-/-}$ PyMT^{+} and Vhl$^{-/-}$ PyMT^{+} mice. Our data suggest that reduced expression of PTHrP in the primary tumor may mediate the decreased bone dissemination in Hif2α$^{-/-}$ PyMT^{+} mice, while increased CXCR4 expression may regulate bone dissemination in Vhl$^{-/-}$ PyMT^{+} mice. PTHrP (gene name *PTHLH*), is a key driver of osteolysis in bone-disseminated breast cancer, but its role in the primary tumor is more nuanced [374]. Previous work using the MMTV-PyMT model demonstrated that PTHrP deletion in the mammary epithelium delays primary tumor initiation, inhibits tumor progression, and reduces metastasis to distal sites [355]. Loss of primary tumor PTHrP expression in a MMTV-*nue* model of breast cancer, however, showed the opposite outcome, with PTHrP loss resulting in higher tumor incidence [375]. Clinical studies have also shown that patients with PTHrP-positive primary tumors have significantly improved survival and fewer metastases to distant sites including the bone [376, 377]. PTHrP is known to be expressed in a HIF2α, but not HIF1α, dependent manner [167]. In accordance with the decreased *Pthlh* expression we observe in

Hif2α$^{-/-}$ tumors, the increased *Pthlh* expression in Vhl$^{-/-}$ tumors is likely due to Hif2α activation rather than Hif1α. CXCR4 is known to drive breast cancer metastasis to bone through engagement with its cognate ligand, CXCL12, which is highly expressed on mesenchymal stromal cells in the bone marrow [136, 358]. Interestingly, although CXCR4 expression is known to be HIF1α-dependent [97], we did not observe a decrease in *Cxcr4* transcript in response to *Hif1α* deletion. There is also evidence that HIF2α is required for CXCR4 expression in renal cancer cell lines [378], but we did not observe a difference in *Cxcr4* expression in response to *Hif2α* deletion. This suggests that in our model, deletion of either of the HIFα factors on their own was not sufficient to decrease *Cxcr4*, but the combined stabilization of Hif1α and Hif2α may have been sufficient to drive *Cxcr4* expression. Alternatively, the increase in *Cxcr4* in response to *Vhl* deletion could be mediated by HIF-independent pathways. While VHL functions to regulate HIF signaling activity by modulating degradation of HIF1α and HIF2α, VHL also possesses HIF-independent functions [379, 380]. For example, VHL has been shown to degrade or inhibit the catalytic activity of certain kinases, including some PKC isoforms [381-383], AKT1, and AKT2 [384]. These kinases are involved in signaling pathways that regulate metabolism, angiogenesis, proliferation, differentiation, cell survival, tumor initiation, and metastasis [385-387]. Thus, it is possible that phenotypes observed in the Vhl$^{-/-}$ PyMT^{+} mice may be due, in part, to these HIF-independent pathways. To definitively address whether the phenotype and potential mechanisms observed in the Vhl$^{-/-}$ mice are specific for Hif1α or Hif2α, loss-of-function *Vhl/Hif1α* and *Vhl/Hif2α* double knockout mice will need to be investigated in future studies.

Our findings present important considerations for the development of clinical HIF inhibitors. While targeted inhibition of HIF1α or HIF2α could be beneficial in preventing bone metastasis, HIF1α inhibition may promote the outgrowth of lung-disseminated breast cancer cells. Thus, the site-specific effects of tumor cell HIF signaling must be considered. Furthermore, our results suggest that patients with high levels of HIF1α or HIF2α expression in their primary tumor may be at an increased risk of bone metastasis development. Thus, these markers may have prognostic value and patients with high expression may benefit from bone-focused clinical follow-up over time.

CHAPTER VI

CONCLUSIONS AND FUTURE DIRECTIONS

Conclusions

Hypoxia is a common pathological feature in tumors and a physiological feature of the bone. HIF signaling causes a host of adaptive changes in the primary tumor that drive invasion and metastasis to distant organs, including the bone. While the understanding of tumor dormancy is still evolving, it is clear that hypoxia plays an important role in this process that has significant implications for the long-term care of cancer survivors. The work presented in this dissertation has sought to shed further light on the role of hypoxia in tumor progression, metastasis, and dormancy.

While previous work demonstrated that LIFR promotes dormancy in bone-disseminated MCF7 human breast cancer cells [195], the gene networks regulated downstream of LIFR were not well characterized. In an effort to identify novel dormancy regulators, found a highly interconnected cluster of ECM-related genes downstream of LIFR in ER+ breast cancer cells. Though our *in vitro* characterization of one of these genes, COL14A1, did not strongly support our original hypothesis that it would act as a dormancy promoting factor, the discovery that ECM-related pathways are significantly altered by LIFR signaling points to the possibility that ECM regulation may play a role in the dormancy promoting functions of LIFR.

In addition to investigating how disseminated tumor cells maintain a dormant state, we sought to identify what factors regulate breast cancer cell dissemination to the bone marrow. In particular, we sought to understand whether HIF signaling in primary tumor cells drives tumor cell dissemination to the bone and whether this pro-metastatic effect is organ-specific. Consistent with previous reports [92, 93, 96, 97, 143], we found that HIF signaling promotes dissemination to the bone. It is important to note, however, that the contribution of HIF signaling to bone dissemination appears to be relatively mild, and no overt bone metastases were observed when HIF signaling was activated by *Vhl* deletion. Thus, while it is clear that primary tumor hypoxia increases the risk of bone metastasis, targeting HIF is not the silver bullet in preventing bone lesion development.

We were surprised to find that *Hif1α* deletion resulted in a significant increase in lung tumor burden, as previous work using the same mouse model had shown that deletion of *Hif1α* decreased tumor burden [94]. While we have not been able to identify a mechanism that would explain this discrepancy, it suggests HIF1α expressed in the primary tumor may control additional mechanisms that can impact dissemination to the lung, such as through regulation of the osteogenic niche. In addition, the finding that deletion of *Hif2α* or *Vhl* did not alter metastatic tumor burden in the lung was unexpected, since previous work had demonstrated a pro-lung metastatic role of both HIF1α and HIF2α [93, 364, 365]. It is possible that the lack of an observable impact on lung metastasis in the *Hif2α* or *Vhl* deletion mice may be an artifact of the PyMT mouse system, which has a strong lung-metastasis phenotype and the effect of *Hif2α* or *Vhl* deletion may have been too subtle to observe. Taken together with previous research, this again suggests that while HIF signaling is an important factor driving metastasis, there are other factors that supersede HIF in controlling dissemination. The work presented here also raises additional questions and avenues for further research.

Future directions

Does LIFR signaling alter ECM composition to promote dormancy in bone? While we focused on characterizing COL14A1 in breast cancer cells and investigating its effects on proliferation, COL14A1 is not the only LIFR-regulated gene. Indeed, we found that a large network of ECM-related genes were differentially expressed depending on LIFR expression. Thus, it is possible that LIFR signaling regulates ECM composition in the niche within which breast cancer cells reside. The initial RNAseq analysis that identified this connection between LIFR and ECM genes was performed on cells grown *in vitro*. Due to the challenges inherent in studying ECM regulation, in vivo studies will likely be required to answer whether LIFR expression alters ECM composition and whether this has an impact on breast cancer cell proliferation or dormancy. Growth on a 3D matrix and the activation of integrin signaling has been shown to promote cellular quiescence in some breast cancer cell lines [281]. Thus, the modulation of ECM may prove to be a key mechanism of LIFR-regulated dormancy maintenance or escape. Furthermore, the impact that hypoxia has on the potential LIFR regulation of ECM should be investigated as well, as this could further shed light on the mechanism by which hypoxia alters the dormant state of disseminated cells.

How does HIF1α expression in the primary tumor alter bone volume? An unexpected finding from our work was that deletion of *Hif1α* in the primary tumor cells decreased trabecular bone volume in the tibia, despite a lack of detectable macroscopic tumors in the bone and appropriate controls demonstrating this bone loss does not occur in tumor naïve transgenic animals. *Hif1α* deletion decreased the frequency of disseminated tumor cells in the bone marrow, making it unlikely that the decreased bone volume is the result of greater tumor-induced osteolysis. Thus, the question remains as to what mechanism is underlying this change in bone volume. The altered HIF signaling could be driving the expression of distantly acting factors that we have thus far been unable to identify. These factors could also be altering the bone microenvironment to set up a premetastatic niche, which could explain the altered bone volume we observed. We may not have been able to observe colonization of this niche due to the low levels of bone metastasis in the PyMT mice. Thus, a more robust model of bone metastasis may need to be employed to study premetastatic niche formation. This is an important question to answer, as the connection between primary tumor signaling and bone quality could have significant implications for the clinical treatment of breast cancer patients.

How does HIF signaling drive dissemination in a site-specific manner? *Hif1α* deletion had the most distinct difference in metastasis to different organs, where the number of disseminated tumor cells in the bone was decreased but the metastatic tumor burden in the lung was increased. However, site-specific dissemination effects were seen with *Hif2α* and *Vhl* deletion as well, where dissemination to the bone was decreased or increased, respectively, while lung tumor burden was unaltered. It is unclear which HIF-driven factors are mediating these patterns of metastasis. It is also difficult to determine whether these patterns are an artifact of the model system selected. The PyMT-driven spontaneous mammary carcinoma model has the advantage of being a more physiologically relevant model in terms of disease course but has a strong lung metastasis phenotype and very low level of baseline bone metastasis, which does not completely replicate the metastasis patterns observed in human patients. Measuring lung and bone metastasis following orthotopic injection of Hif1α-, Hif2α-, or Vhl-knockout breast cancer cells could help shed light on this issue. These studies would have to be performed in multiple cell lines, however, in order to minimize the risk of drawing conclusions that are obscured by possible inherent organotropic properties of a given cell line.

Would anti-HIF therapies prevent metastasis in breast cancer patients? Since hypoxia is a common feature among many cancer types, HIF signaling has logically attracted much attention as a potential clinical target. Active HIF signaling in tumor cells is known to drive many pro-metastatic factors and is linked to more aggressive disease [49-51, 63-66, 364, 366]. Thus, inhibiting HIF signaling has the potential to benefit patients, prevent or decrease metastasis, and improve long-term outcomes. Several clinical trials have taken place recently or are currently underway to investigate the efficacy of HIF-targeting drugs. The finding presented here, however, suggest that HIF inhibition could have potential deleterious effects such as adversely affecting bone volume or quality. In addition, judging from the moderate decrease in bone dissemination when *Hif1α* or *Hif2α* were deleted, it is possible that HIF inhibition may not have a robust enough impact on bone metastasis to warrant clinical use. Furthermore, any anti-metastatic effects that these drugs may have will need to be closely assessed to determine whether they are site-specific, as we have observed in mouse models.

Concluding remarks

The work presented in this dissertation provides insights into the nuanced effects of hypoxia on metastasis and the potential significance of ECM regulation in tumor dormancy. The insights gained on the differential effects of HIF1α and HIF2α on primary tumor progression and lung and bone metastasis in particular highlight the fact that these are distinct factors that require individual analysis in future studies. The identification of candidate LIFR regulated genes provides opportunities to further characterize the effects of these individual factors and build a more complete picture of the mechanisms behind LIFR-mediated tumor dormancy. Further understanding the factors that control metastatic dissemination to the bone may help to develop more detailed metastasis risk biomarkers that inform decisions of personalized long-term clinical follow-up regimens. In addition, a better understanding of tumor dormancy may result in the development of dormancy maintenance therapies. Together, further investigation of these aspects of breast cancer biology has the potential to significantly impact the clinical care and outcome of breast cancer patients.

REFERENCES

1. Siegel, R.L., K.D. Miller, and A. Jemal, *Cancer statistics, 2020.* CA Cancer J Clin, 2020. **70**(1): p. 7-30.

2. Husemann, Y., et al., *Systemic spread is an early step in breast cancer.* Cancer Cell, 2008. **13**(1): p. 58-68.

3. Hosseini, H., et al., *Early dissemination seeds metastasis in breast cancer.* Nature, 2016. **540**(7634): p. 552-558.

4. Roodman, G.D., *Mechanisms of bone metastasis.* N Engl J Med, 2004. **350**(16): p. 1655-64.

5. Coleman, R.E. and R.D. Rubens, *The clinical course of bone metastases from breast cancer.* Br J Cancer, 1987. **55**(1): p. 61-6.

6. Guise, T.A., *Molecular mechanisms of osteolytic bone metastases.* Cancer, 2000. **88**(12 Suppl): p. 2892-8.

7. Wu, Q., et al., *Breast cancer subtypes predict the preferential site of distant metastases: a SEER based study.* Oncotarget, 2017. **8**(17): p. 27990-27996.

8. Johnson, R.W., E. Schipani, and A.J. Giaccia, *HIF targets in bone remodeling and metastatic disease.* Pharmacol Ther, 2015. **150**: p. 169-77.

9. Azzi, S., J.K. Hebda, and J. Gavard, *Vascular permeability and drug delivery in cancers.* Front Oncol, 2013. **3**: p. 211.

10. Vaupel, P., M. Hockel, and A. Mayer, *Detection and characterization of tumor hypoxia using pO2 histography.* Antioxid Redox Signal, 2007. **9**(8): p. 1221-35.

11. Spencer, J.A., et al., *Direct measurement of local oxygen concentration in the bone marrow of live animals.* Nature, 2014. **508**(7495): p. 269-73.

12. Semenza, G.L. and G.L. Wang, *A nuclear factor induced by hypoxia via de novo protein synthesis binds to the human erythropoietin gene enhancer at a site required for transcriptional activation.* Mol Cell Biol, 1992. **12**(12): p. 5447-54.

13. Wang, G.L., et al., *Hypoxia-inducible factor 1 is a basic-helix-loop-helix-PAS heterodimer regulated by cellular O2 tension.* Proc Natl Acad Sci U S A, 1995. **92**(12): p. 5510-4.

14. Tian, H., S.L. McKnight, and D.W. Russell, *Endothelial PAS domain protein 1 (EPAS1), a transcription factor selectively expressed in endothelial cells.* Genes Dev, 1997. **11**(1): p. 72-82.

15. Gu, Y.Z., et al., *Molecular characterization and chromosomal localization of a third alpha-class hypoxia inducible factor subunit, HIF3alpha.* Gene Expr, 1998. **7**(3): p. 205-13.

16. Makino, Y., et al., *Inhibitory PAS domain protein (IPAS) is a hypoxia-inducible splicing variant of the hypoxia-inducible factor-3alpha locus.* J Biol Chem, 2002. **277**(36): p. 32405-8.

17. Maynard, M.A., et al., *Multiple splice variants of the human HIF-3 alpha locus are targets of the von Hippel-Lindau E3 ubiquitin ligase complex.* J Biol Chem, 2003. **278**(13): p. 11032-40.

18. Pasanen, A., et al., *Hypoxia-inducible factor (HIF)-3alpha is subject to extensive alternative splicing in human tissues and cancer cells and is regulated by HIF-1 but not HIF-2.* Int J Biochem Cell Biol, 2010. **42**(7): p. 1189-200.

19. Heikkila, M., et al., *Roles of the human hypoxia-inducible factor (HIF)-3alpha variants in the hypoxia response.* Cell Mol Life Sci, 2011. **68**(23): p. 3885-901.

20. Hara, S., et al., *Expression and characterization of hypoxia-inducible factor (HIF)-3alpha in human kidney: suppression of HIF-mediated gene expression by HIF-3alpha.* Biochem Biophys Res Commun, 2001. **287**(4): p. 808-13.

21. Dengler, V.L., M. Galbraith, and J.M. Espinosa, *Transcriptional regulation by hypoxia inducible factors.* Crit Rev Biochem Mol Biol, 2014. **49**(1): p. 1-15.

22. Huang, L.E., et al., *Regulation of hypoxia-inducible factor 1alpha is mediated by an O2-dependent degradation domain via the ubiquitin-proteasome pathway.* Proc Natl Acad Sci U S A, 1998. **95**(14): p. 7987-92.

23. Ohh, M., et al., *Ubiquitination of hypoxia-inducible factor requires direct binding to the beta-domain of the von Hippel-Lindau protein.* Nat Cell Biol, 2000. **2**(7): p. 423-7.

24. Tanimoto, K., et al., *Mechanism of regulation of the hypoxia-inducible factor-1 alpha by the von Hippel-Lindau tumor suppressor protein.* EMBO J, 2000. **19**(16): p. 4298-309.

25. Hon, W.C., et al., *Structural basis for the recognition of hydroxyproline in HIF-1 alpha by pVHL.* Nature, 2002. **417**(6892): p. 975-8.

26. Min, J.H., et al., *Structure of an HIF-1alpha -pVHL complex: hydroxyproline recognition in signaling.* Science, 2002. **296**(5574): p. 1886-9.

27. Duan, D.R., et al., *Inhibition of transcription elongation by the VHL tumor suppressor protein.* Science, 1995. **269**(5229): p. 1402-6.

28. Kibel, A., et al., *Binding of the von Hippel-Lindau tumor suppressor protein to Elongin B and C.* Science, 1995. **269**(5229): p. 1444-6.

29. Kishida, T., et al., *Cellular proteins that bind the von Hippel-Lindau disease gene product: mapping of binding domains and the effect of missense mutations.* Cancer Res, 1995. **55**(20): p. 4544-8.

30. Bruick, R.K. and S.L. McKnight, *A conserved family of prolyl-4-hydroxylases that modify HIF.* Science, 2001. **294**(5545): p. 1337-40.

31. Ivan, M., et al., *HIFalpha targeted for VHL-mediated destruction by proline hydroxylation: implications for O2 sensing.* Science, 2001. **292**(5516): p. 464-8.

32. Jaakkola, P., et al., *Targeting of HIF-alpha to the von Hippel-Lindau ubiquitylation complex by O2-regulated prolyl hydroxylation.* Science, 2001. **292**(5516): p. 468-72.

33. Yu, F., et al., *HIF-1alpha binding to VHL is regulated by stimulus-sensitive proline hydroxylation.* Proc Natl Acad Sci U S A, 2001. **98**(17): p. 9630-5.

34. Schodel, J., et al., *High-resolution genome-wide mapping of HIF-binding sites by ChIP-seq.* Blood, 2011. **117**(23): p. e207-17.

35. Mole, D.R., et al., *Genome-wide association of hypoxia-inducible factor (HIF)-1alpha and HIF-2alpha DNA binding with expression profiling of hypoxia-inducible transcripts.* J Biol Chem, 2009. **284**(25): p. 16767-75.

36. Xia, X. and A.L. Kung, *Preferential binding of HIF-1 to transcriptionally active loci determines cell-type specific response to hypoxia.* Genome Biol, 2009. **10**(10): p. R113.

37. Takeda, N., et al., *Endothelial PAS domain protein 1 gene promotes angiogenesis through the transactivation of both vascular endothelial growth factor and its receptor, Flt-1.* Circ Res, 2004. **95**(2): p. 146-53.

38. Benita, Y., et al., *An integrative genomics approach identifies Hypoxia Inducible Factor-1 (HIF-1)-target genes that form the core response to hypoxia.* Nucleic Acids Res, 2009. **37**(14): p. 4587-602.

39. Semenza, G.L., *Hypoxia-inducible factors: mediators of cancer progression and targets for cancer therapy.* Trends Pharmacol Sci, 2012. **33**(4): p. 207-14.

40. Shweiki, D., et al., *Vascular endothelial growth factor induced by hypoxia may mediate hypoxia-initiated angiogenesis.* Nature, 1992. **359**(6398): p. 843-5.

41. Tsuzuki, Y., et al., *Vascular endothelial growth factor (VEGF) modulation by targeting hypoxia-inducible factor-1alpha--> hypoxia response element--> VEGF cascade differentially regulates vascular response and growth rate in tumors.* Cancer Res, 2000. **60**(22): p. 6248-52.

42. Firth, J.D., B.L. Ebert, and P.J. Ratcliffe, *Hypoxic regulation of lactate dehydrogenase A. Interaction between hypoxia-inducible factor 1 and cAMP response elements.* J Biol Chem, 1995. **270**(36): p. 21021-7.

43. Gleadle, J.M. and P.J. Ratcliffe, *Induction of hypoxia-inducible factor-1, erythropoietin, vascular endothelial growth factor, and glucose transporter-1 by hypoxia: evidence against a regulatory role for Src kinase.* Blood, 1997. **89**(2): p. 503-9.

44. Firth, J.D., et al., *Oxygen-regulated control elements in the phosphoglycerate kinase 1 and lactate dehydrogenase A genes: similarities with the erythropoietin 3' enhancer.* Proc Natl Acad Sci U S A, 1994. **91**(14): p. 6496-500.

45. Ebert, B.L., J.D. Firth, and P.J. Ratcliffe, *Hypoxia and mitochondrial inhibitors regulate expression of glucose transporter-1 via distinct Cis-acting sequences.* J Biol Chem, 1995. **270**(49): p. 29083-9.

46. Gossage, L., T. Eisen, and E.R. Maher, *VHL, the story of a tumour suppressor gene.* Nat Rev Cancer, 2015. **15**(1): p. 55-64.

47. Semenza, G.L., *Heritable disorders of oxygen sensing.* Am J Med Genet A, 2021. **185**(8): p. 2576-2581.

48. Sourvinos, G., et al., *Von Hippel-Lindau tumour suppressor gene is not involved in sporadic human breast cancer.* Tumour Biol, 2001. **22**(3): p. 131-6.

49. Petrella, B.L., J. Lohi, and C.E. Brinckerhoff, *Identification of membrane type-1 matrix metalloproteinase as a target of hypoxia-inducible factor-2 alpha in von Hippel-Lindau renal cell carcinoma.* Oncogene, 2005. **24**(6): p. 1043-52.

50. Erler, J.T., et al., *Lysyl oxidase is essential for hypoxia-induced metastasis.* Nature, 2006. **440**(7088): p. 1222-6.

51. Yang, M.H., et al., *Direct regulation of TWIST by HIF-1alpha promotes metastasis.* Nat Cell Biol, 2008. **10**(3): p. 295-305.

52. Munoz-Najar, U.M., et al., *Hypoxia stimulates breast carcinoma cell invasion through MT1-MMP and MMP-2 activation.* Oncogene, 2006. **25**(16): p. 2379-92.

53. Choi, J.Y., et al., *Overexpression of MMP-9 and HIF-1alpha in Breast Cancer Cells under Hypoxic Conditions.* J Breast Cancer, 2011. **14**(2): p. 88-95.

54. Krishnamachary, B., et al., *Regulation of colon carcinoma cell invasion by hypoxia-inducible factor 1.* Cancer Res, 2003. **63**(5): p. 1138-43.

55. Aro, E., et al., *Hypoxia-inducible factor-1 (HIF-1) but not HIF-2 is essential for hypoxic induction of collagen prolyl 4-hydroxylases in primary newborn mouse epiphyseal growth plate chondrocytes.* J Biol Chem, 2012. **287**(44): p. 37134-44.

56. Acevedo-Jake, A.M., D.H. Ngo, and J.D. Hartgerink, *Control of Collagen Triple Helix Stability by Phosphorylation.* Biomacromolecules, 2017. **18**(4): p. 1157-1161.

57. Gilkes, D.M., G.L. Semenza, and D. Wirtz, *Hypoxia and the extracellular matrix: drivers of tumour metastasis.* Nat Rev Cancer, 2014. **14**(6): p. 430-9.

58. Gilkes, D.M., et al., *Collagen prolyl hydroxylases are essential for breast cancer metastasis.* Cancer Res, 2013. **73**(11): p. 3285-96.

59. Xiong, G., et al., *Prolyl-4-hydroxylase alpha subunit 2 promotes breast cancer progression and metastasis by regulating collagen deposition.* BMC Cancer, 2014. **14**: p. 1.

60. Eisinger-Mathason, T.S., et al., *Hypoxia-dependent modification of collagen networks promotes sarcoma metastasis.* Cancer Discov, 2013. **3**(10): p. 1190-205.

61. van der Slot, A.J., et al., *Elevated formation of pyridinoline cross-links by profibrotic cytokines is associated with enhanced lysyl hydroxylase 2b levels.* Biochim Biophys Acta, 2005. **1741**(1-2): p. 95-102.

62. Levental, K.R., et al., *Matrix crosslinking forces tumor progression by enhancing integrin signaling.* Cell, 2009. **139**(5): p. 891-906.

63. Schindl, M., et al., *Overexpression of hypoxia-inducible factor 1alpha is associated with an unfavorable prognosis in lymph node-positive breast cancer.* Clin Cancer Res, 2002. **8**(6): p. 1831-7.

64. Dales, J.P., et al., *Overexpression of hypoxia-inducible factor HIF-1alpha predicts early relapse in breast cancer: retrospective study in a series of 745 patients.* Int J Cancer, 2005. **116**(5): p. 734-9.

65. Bos, R., et al., *Levels of hypoxia-inducible factor-1alpha independently predict prognosis in patients with lymph node negative breast carcinoma.* Cancer, 2003. **97**(6): p. 1573-81.

66. Generali, D., et al., *Hypoxia-inducible factor-1alpha expression predicts a poor response to primary chemoendocrine therapy and disease-free survival in primary human breast cancer.* Clin Cancer Res, 2006. **12**(15): p. 4562-8.

67. Hung, J.J., et al., *Prognostic significance of hypoxia-inducible factor-1alpha, TWIST1 and Snail expression in resectable non-small cell lung cancer.* Thorax, 2009. **64**(12): p. 1082-9.

68. Aebersold, D.M., et al., *Expression of hypoxia-inducible factor-1alpha: a novel predictive and prognostic parameter in the radiotherapy of oropharyngeal cancer.* Cancer Res, 2001. **61**(7): p. 2911-6.

69. Zhou, J., et al., *Clinical and prognostic significance of HIF-1alpha overexpression in oral squamous cell carcinoma: a meta-analysis.* World J Surg Oncol, 2017. **15**(1): p. 104.

70. Birner, P., et al., *Expression of hypoxia-inducible factor-1 alpha in oligodendrogliomas: its impact on prognosis and on neoangiogenesis.* Cancer, 2001. **92**(1): p. 165-71.

71. Birner, P., et al., *Expression of hypoxia-inducible factor 1alpha in epithelial ovarian tumors: its impact on prognosis and on response to chemotherapy.* Clin Cancer Res, 2001. **7**(6): p. 1661-8.

72. Birner, P., et al., *Overexpression of hypoxia-inducible factor 1alpha is a marker for an unfavorable prognosis in early-stage invasive cervical cancer.* Cancer Res, 2000. **60**(17): p. 4693-6.

73. Moreno Roig, E., et al., *Prognostic Role of Hypoxia-Inducible Factor-2alpha Tumor Cell Expression in Cancer Patients: A Meta-Analysis.* Front Oncol, 2018. **8**: p. 224.

74. Asosingh, K., et al., *Role of the hypoxic bone marrow microenvironment in 5T2MM murine myeloma tumor progression.* Haematologica, 2005. **90**(6): p. 810-7.

75. Jensen, P.O., et al., *Increased cellular hypoxia and reduced proliferation of both normal and leukaemic cells during progression of acute myeloid leukaemia in rats.* Cell Prolif, 2000. **33**(6): p. 381-95.

76. Konopleva, M., et al., *Phase I/II study of the hypoxia-activated prodrug PR104 in refractory/relapsed acute myeloid leukemia and acute lymphoblastic leukemia.* Haematologica, 2015. **100**(7): p. 927-34.

77. Irigoyen, M., J.C. Garcia-Ruiz, and E. Berra, *The hypoxia signalling pathway in haematological malignancies.* Oncotarget, 2017. **8**(22): p. 36832-36844.

78. Petit, C., et al., *Hypoxia promotes chemoresistance in acute lymphoblastic leukemia cell lines by modulating death signaling pathways.* BMC Cancer, 2016. **16**(1): p. 746.

79. Deeb, G., et al., *Hypoxia-inducible factor-1alpha protein expression is associated with poor survival in normal karyotype adult acute myeloid leukemia.* Leuk Res, 2011. **35**(5): p. 579-84.

80. Rankin, E.B., et al., *The HIF signaling pathway in osteoblasts directly modulates erythropoiesis through the production of EPO.* Cell, 2012. **149**(1): p. 63-74.

81. Wu, C., et al., *Oxygen-sensing PHDs regulate bone homeostasis through the modulation of osteoprotegerin.* Genes Dev, 2015. **29**(8): p. 817-31.

82. Crock, H.V., *A Revision of the Anatomy of the Arteries Supplying the Upper End of the Human Femur.* J Anat, 1965. **99**: p. 77-88.

83. Trueta, J. and M.H. Harrison, *The normal vascular anatomy of the femoral head in adult man.* J Bone Joint Surg Br, 1953. **35-B**(3): p. 442-61.

84. Trueta, J. and J.D. Morgan, *The vascular contribution to osteogenesis. I. Studies by the injection method.* J Bone Joint Surg Br, 1960. **42-B**: p. 97-109.

85. Branemark, P., *Experimental Investigation of Microcirculation in Bone Marrow.* Angiology, 1961. **12**(7): p. 293-&.

86. Kusumbe, A.P., S.K. Ramasamy, and R.H. Adams, *Coupling of angiogenesis and osteogenesis by a specific vessel subtype in bone.* Nature, 2014. **507**(7492): p. 323-328.

87. Sivaraj, K.K. and R.H. Adams, *Blood vessel formation and function in bone.* Development, 2016. **143**(15): p. 2706-15.

88. Gruneboom, A., et al., *A network of trans-cortical capillaries as mainstay for blood circulation in long bones.* Nat Metab, 2019. **1**(2): p. 236-250.

89. Chow, D.C., et al., *Modeling pO(2) distributions in the bone marrow hematopoietic compartment. I. Krogh's model.* Biophys J, 2001. **81**(2): p. 675-84.

90. Chow, D.C., et al., *Modeling pO(2) distributions in the bone marrow hematopoietic compartment. II. Modified Kroghian models.* Biophys J, 2001. **81**(2): p. 685-96.

91. Zahm, A.M., et al., *Numerical modeling of oxygen distributions in cortical and cancellous bone: oxygen availability governs osteonal and trabecular dimensions.* Am J Physiol Cell Physiol, 2010. **299**(5): p. C922-9.

92. Woelfle, U., et al., *Molecular signature associated with bone marrow micrometastasis in human breast cancer.* Cancer Res, 2003. **63**(18): p. 5679-84.

93. Lu, X., et al., *In vivo dynamics and distinct functions of hypoxia in primary tumor growth and organotropic metastasis of breast cancer.* Cancer Res, 2010. **70**(10): p. 3905-14.

94. Liao, D., et al., *Hypoxia-inducible factor-1alpha is a key regulator of metastasis in a transgenic model of cancer initiation and progression.* Cancer Res, 2007. **67**(2): p. 563-72.

95. Niu, Y., et al., *HIF-2-induced long non-coding RNA RAB11B-AS1 promotes hypoxia-mediated angiogenesis and breast cancer metastasis.* Cancer Res, 2020.

96. Hiraga, T., et al., *Hypoxia and hypoxia-inducible factor-1 expression enhance osteolytic bone metastases of breast cancer.* Cancer Res, 2007. **67**(9): p. 4157-63.

97. Dunn, L.K., et al., *Hypoxia and TGF-beta drive breast cancer bone metastases through parallel signaling pathways in tumor cells and the bone microenvironment.* PLoS One, 2009. **4**(9): p. e6896.

98. Xiang, L. and D.M. Gilkes, *The Contribution of the Immune System in Bone Metastasis Pathogenesis.* Int J Mol Sci, 2019. **20**(4).

99. Lee, H.W., et al., *Recruitment of monocytes/macrophages in different tumor microenvironments.* Biochim Biophys Acta, 2013. **1835**(2): p. 170-9.

100. Karnevi, E., R. Andersson, and A.H. Rosendahl, *Tumour-educated macrophages display a mixed polarisation and enhance pancreatic cancer cell invasion.* Immunol Cell Biol, 2014. **92**(6): p. 543-52.

101. Sinder, B.P., A.R. Pettit, and L.K. McCauley, *Macrophages: Their Emerging Roles in Bone.* J Bone Miner Res, 2015. **30**(12): p. 2140-9.

102. Bates, G.J., et al., *Quantification of regulatory T cells enables the identification of high-risk breast cancer patients and those at risk of late relapse.* J Clin Oncol, 2006. **24**(34): p. 5373-80.

103. Zhao, E., et al., *Regulatory T cells in the bone marrow microenvironment in patients with prostate cancer.* Oncoimmunology, 2012. **1**(2): p. 152-161.

104. Tan, W., et al., *Tumour-infiltrating regulatory T cells stimulate mammary cancer metastasis through RANKL-RANK signalling.* Nature, 2011. **470**(7335): p. 548-53.

105. Thomas, D.A. and J. Massague, *TGF-beta directly targets cytotoxic T cell functions during tumor evasion of immune surveillance.* Cancer Cell, 2005. **8**(5): p. 369-80.

106. Fournier, P.G., J.M. Chirgwin, and T.A. Guise, *New insights into the role of T cells in the vicious cycle of bone metastases.* Curr Opin Rheumatol, 2006. **18**(4): p. 396-404.

107. Palumbo, J.S., et al., *Platelets and fibrin(ogen) increase metastatic potential by impeding natural killer cell-mediated elimination of tumor cells.* Blood, 2005. **105**(1): p. 178-85.

108. Bidwell, B.N., et al., *Silencing of Irf7 pathways in breast cancer cells promotes bone metastasis through immune escape.* Nat Med, 2012. **18**(8): p. 1224-31.

109. Wright, L.E., et al., *Murine models of breast cancer bone metastasis.* Bonekey Rep, 2016. **5**: p. 804.

110. Maletzki, C., et al., *NSG mice as hosts for oncological precision medicine.* Lab Invest, 2020. **100**(1): p. 27-37.

111. Clambey, E.T., et al., *Hypoxia-inducible factor-1 alpha-dependent induction of FoxP3 drives regulatory T-cell abundance and function during inflammatory hypoxia of the mucosa.* Proc Natl Acad Sci U S A, 2012. **109**(41): p. E2784-93.

112. Noman, M.Z., et al., *PD-L1 is a novel direct target of HIF-1alpha, and its blockade under hypoxia enhanced MDSC-mediated T cell activation.* J Exp Med, 2014. **211**(5): p. 781-90.

113. Calcinotto, A., et al., *Modulation of microenvironment acidity reverses anergy in human and murine tumor-infiltrating T lymphocytes.* Cancer Res, 2012. **72**(11): p. 2746-56.

114. Takeda, N., et al., *Differential activation and antagonistic function of HIF-{alpha} isoforms in macrophages are essential for NO homeostasis.* Genes Dev, 2010. **24**(5): p. 491-501.

115. Schaefer, E., et al., *Intermittent hypoxia is a proinflammatory stimulus resulting in IL-6 expression and M1 macrophage polarization.* Hepatol Commun, 2017. **1**(4): p. 326-337.

116. Zhou, J., et al., *Intermittent Hypoxia Enhances THP-1 Monocyte Adhesion and Chemotaxis and Promotes M1 Macrophage Polarization via RAGE.* Biomed Res Int, 2018. **2018**: p. 1650456.

117. Michiels, C., C. Tellier, and O. Feron, *Cycling hypoxia: A key feature of the tumor microenvironment.* Biochim Biophys Acta, 2016. **1866**(1): p. 76-86.

118. Harrison, H., et al., *HIF1-alpha expressing cells induce a hypoxic-like response in neighbouring cancer cells.* BMC Cancer, 2018. **18**(1): p. 674.

119. Patton, M.C., et al., *Hypoxia alters the release and size distribution of extracellular vesicles in pancreatic cancer cells to support their adaptive survival.* J Cell Biochem, 2020. **121**(1): p. 828-839.

120. Wang, T., et al., *Hypoxia-inducible factors and RAB22A mediate formation of microvesicles that stimulate breast cancer invasion and metastasis.* Proc Natl Acad Sci U S A, 2014. **111**(31): p. E3234-42.

121. Peinado, H., et al., *Melanoma exosomes educate bone marrow progenitor cells toward a pro-metastatic phenotype through MET.* Nat Med, 2012. **18**(6): p. 883-91.

122. Rossi, M., et al., *The Role of Extracellular Vesicles in Bone Metastasis.* Int J Mol Sci, 2018. **19**(4).

123. Taverna, S., et al., *Amphiregulin contained in NSCLC-exosomes induces osteoclast differentiation through the activation of EGFR pathway.* Sci Rep, 2017. **7**(1): p. 3170.

124. Faict, S., et al., *Exosomes play a role in multiple myeloma bone disease and tumor development by targeting osteoclasts and osteoblasts.* Blood Cancer J, 2018. **8**(11): p. 105.

125. Dai, J., et al., *Primary prostate cancer educates bone stroma through exosomal pyruvate kinase M2 to promote bone metastasis.* J Exp Med, 2019. **216**(12): p. 2883-2899.

126. Erler, J.T., et al., *Hypoxia-induced lysyl oxidase is a critical mediator of bone marrow cell recruitment to form the premetastatic niche.* Cancer Cell, 2009. **15**(1): p. 35-44.

127. Liu, Y. and X. Cao, *Characteristics and Significance of the Pre-metastatic Niche.* Cancer Cell, 2016. **30**(5): p. 668-681.

128. Peinado, H., et al., *Pre-metastatic niches: organ-specific homes for metastases.* Nat Rev Cancer, 2017. **17**(5): p. 302-317.

129. Kaplan, R.N., et al., *VEGFR1-positive haematopoietic bone marrow progenitors initiate the pre-metastatic niche.* Nature, 2005. **438**(7069): p. 820-7.

130. Murgai, M., et al., *KLF4-dependent perivascular cell plasticity mediates pre-metastatic niche formation and metastasis.* Nat Med, 2017. **23**(10): p. 1176-1190.

131. Devignes, C.S., et al., *HIF signaling in osteoblast-lineage cells promotes systemic breast cancer growth and metastasis in mice.* Proc Natl Acad Sci U S A, 2018. **115**(5): p. E992-E1001.

132. Ceradini, D.J., et al., *Progenitor cell trafficking is regulated by hypoxic gradients through HIF-1 induction of SDF-1.* Nat Med, 2004. **10**(8): p. 858-64.

133. Du, R., et al., *HIF1alpha induces the recruitment of bone marrow-derived vascular modulatory cells to regulate tumor angiogenesis and invasion.* Cancer Cell, 2008. **13**(3): p. 206-20.

134. Hitchon, C., et al., *Hypoxia-induced production of stromal cell-derived factor 1 (CXCL12) and vascular endothelial growth factor by synovial fibroblasts.* Arthritis Rheum, 2002. **46**(10): p. 2587-97.

135. Zou, D., et al., *Blood vessel formation in the tissue-engineered bone with the constitutively active form of HIF-1alpha mediated BMSCs.* Biomaterials, 2012. **33**(7): p. 2097-108.

136. Guo, F., et al., *CXCL12/CXCR4: a symbiotic bridge linking cancer cells and their stromal neighbors in oncogenic communication networks.* Oncogene, 2016. **35**(7): p. 816-26.

137. Barker, H.E., et al., *LOXL2-mediated matrix remodeling in metastasis and mammary gland involution.* Cancer Res, 2011. **71**(5): p. 1561-72.

138. Barker, H.E., T.R. Cox, and J.T. Erler, *The rationale for targeting the LOX family in cancer.* Nat Rev Cancer, 2012. **12**(8): p. 540-52.

139. Pez, F., et al., *The HIF-1-inducible lysyl oxidase activates HIF-1 via the Akt pathway in a positive regulation loop and synergizes with HIF-1 in promoting tumor cell growth.* Cancer Res, 2011. **71**(5): p. 1647-57.

140. Baker, A.M., et al., *Lysyl oxidase enzymatic function increases stiffness to drive colorectal cancer progression through FAK.* Oncogene, 2013. **32**(14): p. 1863-8.

141. Cox, T.R., et al., *LOX-mediated collagen crosslinking is responsible for fibrosis-enhanced metastasis.* Cancer Res, 2013. **73**(6): p. 1721-32.

142. Reynaud, C., et al., *Lysyl Oxidase Is a Strong Determinant of Tumor Cell Colonization in Bone.* Cancer Res, 2017. **77**(2): p. 268-278.

143. Cox, T.R., et al., *The hypoxic cancer secretome induces pre-metastatic bone lesions through lysyl oxidase.* Nature, 2015. **522**(7554): p. 106-110.

144. Mundy, G.R., *Mechanisms of bone metastasis.* Cancer, 1997. **80**(8 Suppl): p. 1546-56.

145. Kohart, N.A., et al., *Parathyroid hormone-related protein promotes bone loss in T-cell leukemia as well as in solid tumors.* Leuk Lymphoma, 2020. **61**(2): p. 409-419.

146. Powell, G.J., et al., *Localization of parathyroid hormone-related protein in breast cancer metastases: increased incidence in bone compared with other sites.* Cancer Res, 1991. **51**(11): p. 3059-61.

147. Vargas, S.J., et al., *Localization of parathyroid hormone-related protein mRNA expression in breast cancer and metastatic lesions by in situ hybridization.* J Bone Miner Res, 1992. **7**(8): p. 971-9.

148. Kohno, N., et al., *Parathyroid Hormone-related Protein in Breast Cancer Tissues: Relationship between Primary and Metastatic Sites.* Breast Cancer, 1994. **1**(1): p. 43-49.

149. Johnson, R.W., et al., *Wnt signaling induces gene expression of factors associated with bone destruction in lung and breast cancer.* Clin Exp Metastasis, 2014. **31**(8): p. 945-59.

150. Kuo, P.L., et al., *MicroRNA-33a functions as a bone metastasis suppressor in lung cancer by targeting parathyroid hormone related protein.* Biochim Biophys Acta, 2013. **1830**(6): p. 3756-66.

151. Poole, K.E. and J. Reeve, *Parathyroid hormone - a bone anabolic and catabolic agent.* Curr Opin Pharmacol, 2005. **5**(6): p. 612-7.

152. Abou-Samra, A.B., et al., *Expression cloning of a common receptor for parathyroid hormone and parathyroid hormone-related peptide from rat osteoblast-like cells: a single receptor stimulates intracellular accumulation of both cAMP and inositol trisphosphates and increases intracellular free calcium.* Proc Natl Acad Sci U S A, 1992. **89**(7): p. 2732-6.

153. Juppner, H., et al., *A G protein-linked receptor for parathyroid hormone and parathyroid hormone-related peptide.* Science, 1991. **254**(5034): p. 1024-6.

154. Pioszak, A.A., et al., *Structural basis for parathyroid hormone-related protein binding to the parathyroid hormone receptor and design of conformation-selective peptides.* J Biol Chem, 2009. **284**(41): p. 28382-91.

155. Halladay, D.L., et al., *Identification of signal transduction pathways and promoter sequences that mediate parathyroid hormone 1-38 inhibition of osteoprotegerin gene expression.* J Cell Biochem, 2001. **84**(1): p. 1-11.

156. Udagawa, N., et al., *Osteoblasts/stromal cells stimulate osteoclast activation through expression of osteoclast differentiation factor/RANKL but not macrophage colony-stimulating factor: receptor activator of NF-kappa B ligand.* Bone, 1999. **25**(5): p. 517-23.

157. Hsu, H., et al., *Tumor necrosis factor receptor family member RANK mediates osteoclast differentiation and activation induced by osteoprotegerin ligand.* Proc Natl Acad Sci U S A, 1999. **96**(7): p. 3540-5.

158. Jansen, I.D., et al., *Osteoclast fusion and fission.* Calcif Tissue Int, 2012. **90**(6): p. 515-22.

159. Lacey, D.L., et al., *Osteoprotegerin ligand is a cytokine that regulates osteoclast differentiation and activation.* Cell, 1998. **93**(2): p. 165-76.

160. Hauschka, P.V., et al., *Growth factors in bone matrix. Isolation of multiple types by affinity chromatography on heparin-Sepharose.* J Biol Chem, 1986. **261**(27): p. 12665-74.

161. Hiraga, T., et al., *Bone-derived IGF mediates crosstalk between bone and breast cancer cells in bony metastases.* Cancer Res, 2012. **72**(16): p. 4238-49.

162. Frolik, C.A., L.F. Ellis, and D.C. Williams, *Isolation and characterization of insulin-like growth factor-II from human bone.* Biochem Biophys Res Commun, 1988. **151**(3): p. 1011-8.

163. Seyedin, S.M., et al., *Cartilage-inducing factor-A. Apparent identity to transforming growth factor-beta.* J Biol Chem, 1986. **261**(13): p. 5693-5.

164. Bonewald, L.F. and G.R. Mundy, *Role of transforming growth factor-beta in bone remodeling.* Clin Orthop Relat Res, 1990(250): p. 261-76.

165. Sterling, J.A., et al., *Advances in the biology of bone metastasis: how the skeleton affects tumor behavior.* Bone, 2011. **48**(1): p. 6-15.

166. Mundy, G.R., *Metastasis to bone: causes, consequences and therapeutic opportunities.* Nat Rev Cancer, 2002. **2**(8): p. 584-93.

167. Manisterski, M., et al., *Hypoxia induces PTHrP gene transcription in human cancer cells through the HIF-2alpha.* Cell Cycle, 2010. **9**(18): p. 3723-9.

168. Browe, D.C., et al., *Hypoxia Activates the PTHrP -MEF2C Pathway to Attenuate Hypertrophy in Mesenchymal Stem Cell Derived Cartilage.* Sci Rep, 2019. **9**(1): p. 13274.

169. Pelosi, M., et al., *Parathyroid hormone-related protein is induced by hypoxia and promotes expression of the differentiated phenotype of human articular chondrocytes.* Clin Sci (Lond), 2013. **125**(10): p. 461-70.

170. Tang, Z.N., et al., *Hypoxia induces RANK and RANKL expression by activating HIF-1alpha in breast cancer cells.* Biochem Biophys Res Commun, 2011. **408**(3): p. 411-6.

171. Dandajena, T.C., et al., *Hypoxia triggers a HIF-mediated differentiation of peripheral blood mononuclear cells into osteoclasts.* Orthod Craniofac Res, 2012. **15**(1): p. 1-9.

172. Knowles, H.J. and N.A. Athanasou, *Hypoxia-inducible factor is expressed in giant cell tumour of bone and mediates paracrine effects of hypoxia on monocyte-osteoclast differentiation via induction of VEGF.* J Pathol, 2008. **215**(1): p. 56-66.

173. Fukuoka, H., et al., *Hypoxic stress enhances osteoclast differentiation via increasing IGF2 production by non-osteoclastic cells.* Biochem Biophys Res Commun, 2005. **328**(4): p. 885-94.

174. Hinoi, E., et al., *Positive regulation of osteoclastic differentiation by growth differentiation factor 15 upregulated in osteocytic cells under hypoxia.* J Bone Miner Res, 2012. **27**(4): p. 938-49.

175. Shao, J., et al., *HIF-1alpha disturbs osteoblasts and osteoclasts coupling in bone remodeling by up-regulating OPG expression.* In Vitro Cell Dev Biol Anim, 2015. **51**(8): p. 808-14.

176. Lee, S.Y., et al., *Controlling hypoxia-inducible factor-2alpha is critical for maintaining bone homeostasis in mice.* Bone Res, 2019. **7**: p. 14.

177. Wang, Y., et al., *The hypoxia-inducible factor alpha pathway couples angiogenesis to osteogenesis during skeletal development.* J Clin Invest, 2007. **117**(6): p. 1616-26.

178. Arnett, T.R., et al., *Hypoxia is a major stimulator of osteoclast formation and bone resorption.* J Cell Physiol, 2003. **196**(1): p. 2-8.

179. Knowles, H.J. and N.A. Athanasou, *Acute hypoxia and osteoclast activity: a balance between enhanced resorption and increased apoptosis.* J Pathol, 2009. **218**(2): p. 256-64.

180. Ma, Z., et al., *Constant hypoxia inhibits osteoclast differentiation and bone resorption by regulating phosphorylation of JNK and IkappaBalpha.* Inflamm Res, 2019. **68**(2): p. 157-166.

181. Leger, A.J., et al., *Inhibition of osteoclastogenesis by prolyl hydroxylase inhibitor dimethyloxallyl glycine.* J Bone Miner Metab, 2010. **28**(5): p. 510-9.

182. Hulley, P.A., et al., *Hypoxia-inducible factor 1-alpha does not regulate osteoclastogenesis but enhances bone resorption activity via prolyl-4-hydroxylase 2.* J Pathol, 2017. **242**(3): p. 322-333.

183. Kang, H., et al., *Osteoblast Hypoxia-Inducible Factor-1alpha Pathway Activation Restrains Osteoclastogenesis via the Interleukin-33-MicroRNA-34a-Notch1 Pathway.* Front Immunol, 2017. **8**: p. 1312.

184. Takemori, T., et al., *Transcutaneous carbon dioxide application suppresses bone destruction caused by breast cancer metastasis.* Oncol Rep, 2018. **40**(4): p. 2079-2087.

185. Jeong, W., et al., *Pilot trial of EZN-2968, an antisense oligonucleotide inhibitor of hypoxia-inducible factor-1 alpha (HIF-1alpha), in patients with refractory solid tumors.* Cancer Chemother Pharmacol, 2014. **73**(2): p. 343-8.

186. Johnson, R.W. and L.J. Suva, *Hallmarks of Bone Metastasis.* Calcif Tissue Int, 2018. **102**(2): p. 141-151.

187. David Roodman, G. and R. Silbermann, *Mechanisms of osteolytic and osteoblastic skeletal lesions.* Bonekey Rep, 2015. **4**: p. 753.

188. Gomis, R.R. and S. Gawrzak, *Tumor cell dormancy.* Mol Oncol, 2016.

189. Naumov, G.N., et al., *Persistence of solitary mammary carcinoma cells in a secondary site: A possible contributor to dormancy.* Cancer Research, 2002. **62**(7): p. 2162-2168.

190. Ghiso, J.A.A., K. Kovalski, and L. Ossowski, *Tumor dormancy induced by downregulation of urokinase receptor in human carcinoma involves integrin and MAPK signaling.* Journal of Cell Biology, 1999. **147**(1): p. 89-103.

191. Naumov, G.N., L.A. Akslen, and J. Folkman, *Role of angiogenesis in human tumor dormancy: animal models of the angiogenic switch.* Cell Cycle, 2006. **5**(16): p. 1779-87.

192. Ghajar, C.M., et al., *The perivascular niche regulates breast tumour dormancy.* Nat Cell Biol, 2013. **15**(7): p. 807-17.

193. Iorns, E., et al., *Whole genome in vivo RNAi screening identifies the leukemia inhibitory factor receptor as a novel breast tumor suppressor.* Breast Cancer Res Treat, 2012. **135**(1): p. 79-91.

194. Chen, D., et al., *LIFR is a breast cancer metastasis suppressor upstream of the Hippo-YAP pathway and a prognostic marker.* Nat Med, 2012. **18**(10): p. 1511-7.

195. Johnson, R.W., et al., *Induction of LIFR confers a dormancy phenotype in breast cancer cells disseminated to the bone marrow.* Nat Cell Biol, 2016. **18**(10): p. 1078-1089.

196. Johnson, R.W., et al., *Parathyroid Hormone-Related Protein Negatively Regulates Tumor Cell Dormancy Genes in a PTHR1/Cyclic AMP-Independent Manner.* Front Endocrinol (Lausanne), 2018. **9**: p. 241.

197. Sosa, M.S., et al., *NR2F1 controls tumour cell dormancy via SOX9- and RARbeta-driven quiescence programmes.* Nat Commun, 2015. **6**: p. 6170.

198. Thompson, V.C., et al., *A gene signature identified using a mouse model of androgen receptor-dependent prostate cancer predicts biochemical relapse in human disease.* Int J Cancer, 2012. **131**(3): p. 662-72.

199. Montagner, M., et al., *SHARP1 suppresses breast cancer metastasis by promoting degradation of hypoxia-inducible factors.* Nature, 2012. **487**(7407): p. 380-4.

200. Fluegen, G., et al., *Phenotypic heterogeneity of disseminated tumour cells is preset by primary tumour hypoxic microenvironments.* Nature Cell Biology, 2017. **19**(2): p. 120-132.

201. Aguirre-Ghiso, J.A., *Models, mechanisms and clinical evidence for cancer dormancy.* Nat Rev Cancer, 2007. **7**(11): p. 834-46.

202. Lan, J., et al., *Hypoxia-inducible factor 1-dependent expression of adenosine receptor 2B promotes breast cancer stem cell enrichment.* Proc Natl Acad Sci U S A, 2018. **115**(41): p. E9640-E9648.

203. Lee, G., et al., *Dedifferentiation of Glioma Cells to Glioma Stem-like Cells By Therapeutic Stress-induced HIF Signaling in the Recurrent GBM Model.* Mol Cancer Ther, 2016. **15**(12): p. 3064-3076.

204. Thomas, S., et al., *CD24 is an effector of HIF-1-driven primary tumor growth and metastasis.* Cancer Res, 2012. **72**(21): p. 5600-12.

205. Kim, J.M., et al., *Osteoblast-Osteoclast Communication and Bone Homeostasis.* Cells, 2020. **9**(9).

206. Susa, M., et al., *Human primary osteoclasts: in vitro generation and applications as pharmacological and clinical assay.* J Transl Med, 2004. **2**(1): p. 6.

207. Rumpler, M., et al., *Osteoclasts on bone and dentin in vitro: mechanism of trail formation and comparison of resorption behavior.* Calcif Tissue Int, 2013. **93**(6): p. 526-39.

208. Dadwal, U.C., et al., *3D Bone Morphology Alters Gene Expression, Motility, and Drug Responses in Bone Metastatic Tumor Cells.* Int J Mol Sci, 2020. **21**(18).

209. Guo, R., et al., *Fabrication of 3D Scaffolds with Precisely Controlled Substrate Modulus and Pore Size by Templated-Fused Deposition Modeling to Direct Osteogenic Differentiation.* Adv Healthc Mater, 2015. **4**(12): p. 1826-32.

210. Vanderburgh, J.P., et al., *Fabrication of Trabecular Bone-Templated Tissue-Engineered Constructs by 3D Inkjet Printing.* Adv Healthc Mater, 2017. **6**(22).

211. Denry, I. and L.T. Kuhn, *Design and characterization of calcium phosphate ceramic scaffolds for bone tissue engineering.* Dent Mater, 2016. **32**(1): p. 43-53.

212. Melke, J., et al., *Silk fibroin as biomaterial for bone tissue engineering.* Acta Biomater, 2016. **31**: p. 1-16.

213. Matziolis, G., et al., *Simulation of cell differentiation in fracture healing: mechanically loaded composite scaffolds in a novel bioreactor system.* Tissue Eng, 2006. **12**(1): p. 201-8.

214. Mitra, D., et al., *Bioreactor culture duration of engineered constructs influences bone formation by mesenchymal stem cells.* Biomaterials, 2017. **146**: p. 29-39.

215. Peroglio, M., et al., *Relevance of bioreactors and whole tissue cultures for the translation of new therapies to humans.* J Orthop Res, 2018. **36**(1): p. 10-21.

216. Liu, B., et al., *Perfusion applied to a 3D model of bone metastasis results in uniformly dispersed mechanical stimuli.* Biotechnol Bioeng, 2018. **115**(4): p. 1076-1085.

217. Lynch, M.E., et al., *In vivo tibial compression decreases osteolysis and tumor formation in a human metastatic breast cancer model.* J Bone Miner Res, 2013. **28**(11): p. 2357-67.

218. Villasante, A., et al., *Tissue-Engineered Model of Human Osteolytic Bone Tumor.* Tissue Eng Part C Methods, 2017. **23**(2): p. 98-107.

219. Reinisch, A., et al., *Generation and use of a humanized bone-marrow-ossicle niche for hematopoietic xenotransplantation into mice.* Nat Protoc, 2017. **12**(10): p. 2169-2188.

220. Reinisch, A., et al., *A humanized bone marrow ossicle xenotransplantation model enables improved engraftment of healthy and leukemic human hematopoietic cells.* Nat Med, 2016. **22**(7): p. 812-21.

221. Attalla, S., et al., *Insights from transgenic mouse models of PyMT-induced breast cancer: recapitulating human breast cancer progression in vivo.* Oncogene, 2021. **40**(3): p. 475-491.

222. Welm, A.L., et al., *The macrophage-stimulating protein pathway promotes metastasis in a mouse model for breast cancer and predicts poor prognosis in humans.* Proc Natl Acad Sci U S A, 2007. **104**(18): p. 7570-5.

223. Ahmed, F., et al., *GFP expression in the mammary gland for imaging of mammary tumor cells in transgenic mice.* Cancer Res, 2002. **62**(24): p. 7166-9.

224. Guy, C.T., R.D. Cardiff, and W.J. Muller, *Induction of mammary tumors by expression of polyomavirus middle T oncogene: a transgenic mouse model for metastatic disease.* Mol Cell Biol, 1992. **12**(3): p. 954-61.

225. Valkenburg, K.C., et al., *A simple selection-free method for detecting disseminated tumor cells (DTCs) in murine bone marrow.* Oncotarget, 2016. **7**(43): p. 69794-69803.

226. Hyun, K.A., et al., *Epithelial-to-mesenchymal transition leads to loss of EpCAM and different physical properties in circulating tumor cells from metastatic breast cancer.* Oncotarget, 2016. **7**(17): p. 24677-87.

227. Davie, S.A., et al., *Effects of FVB/NJ and C57Bl/6J strain backgrounds on mammary tumor phenotype in inducible nitric oxide synthase deficient mice.* Transgenic Res, 2007. **16**(2): p. 193-201.

228. Bolen, J.B., et al., *Enhancement of cellular src gene product associated tyrosyl kinase activity following polyoma virus infection and transformation.* Cell, 1984. **38**(3): p. 767-77.

229. Cheng, S.H., et al., *Peptide antibodies to the human c-fyn gene product demonstrate pp59c-fyn is capable of complex formation with the middle-T antigen of polyomavirus.* EMBO J, 1988. **7**(12): p. 3845-55.

230. Courtneidge, S.A. and A.E. Smith, *Polyoma virus transforming protein associates with the product of the c-src cellular gene.* Nature, 1983. **303**(5916): p. 435-9.

231. Kornbluth, S., M. Sudol, and H. Hanafusa, *Association of the polyomavirus middle-T antigen with c-yes protein.* Nature, 1987. **325**(7000): p. 171-3.

232. Kypta, R.M., A. Hemming, and S.A. Courtneidge, *Identification and characterization of p59fyn (a src-like protein tyrosine kinase) in normal and polyoma virus transformed cells.* EMBO J, 1988. **7**(12): p. 3837-44.

233. Courtneidge, S.A. and A. Heber, *An 81 kd protein complexed with middle T antigen and pp60c-src: a possible phosphatidylinositol kinase.* Cell, 1987. **50**(7): p. 1031-7.

234. Whitman, M., et al., *Association of phosphatidylinositol kinase activity with polyoma middle-T competent for transformation.* Nature, 1985. **315**(6016): p. 239-42.

235. Otten, A.D., M.M. Sanders, and G.S. McKnight, *The MMTV LTR promoter is induced by progesterone and dihydrotestosterone but not by estrogen.* Mol Endocrinol, 1988. **2**(2): p. 143-7.

236. Lin, E.Y., et al., *Progression to malignancy in the polyoma middle T oncoprotein mouse breast cancer model provides a reliable model for human diseases.* Am J Pathol, 2003. **163**(5): p. 2113-26.

237. Guy, C.T., et al., *Expression of the neu protooncogene in the mammary epithelium of transgenic mice induces metastatic disease.* Proc Natl Acad Sci U S A, 1992. **89**(22): p. 10578-82.

238. Muller, W.J., et al., *Synergistic interaction of the Neu proto-oncogene product and transforming growth factor alpha in the mammary epithelium of transgenic mice.* Mol Cell Biol, 1996. **16**(10): p. 5726-36.

239. Moasser, M.M., *The oncogene HER2: its signaling and transforming functions and its role in human cancer pathogenesis.* Oncogene, 2007. **26**(45): p. 6469-87.

240. Andrechek, E.R., et al., *Gene expression profiling of neu-induced mammary tumors from transgenic mice reveals genetic and morphological similarities to ErbB2-expressing human breast cancers.* Cancer Res, 2003. **63**(16): p. 4920-6.

241. Zhang, G.L., et al., *Orthotopic Injection of Breast Cancer Cells into the Mice Mammary Fat Pad.* J Vis Exp, 2019(143).

242. Kocaturk, B. and H.H. Versteeg, *Orthotopic injection of breast cancer cells into the mammary fat pad of mice to study tumor growth.* J Vis Exp, 2015(96).

243. Tavera-Mendoza, L.E. and M. Brown, *A less invasive method for orthotopic injection of breast cancer cells into the mouse mammary gland.* Lab Anim, 2017. **51**(1): p. 85-88.

244. Krall, J.A., et al., *The systemic response to surgery triggers the outgrowth of distant immune-controlled tumors in mouse models of dormancy.* Sci Transl Med, 2018. **10**(436).

245. Fridman, R., et al., *Enhanced tumor growth of both primary and established human and murine tumor cells in athymic mice after coinjection with Matrigel.* J Natl Cancer Inst, 1991. **83**(11): p. 769-74.

246. Bao, L., et al., *Effects of inoculation site and Matrigel on growth and metastasis of human breast cancer cells.* Br J Cancer, 1994. **70**(2): p. 228-32.

247. Goodale, D., et al., *Characterization of tumor cell dissemination patterns in preclinical models of cancer metastasis using flow cytometry and laser scanning cytometry.* Cytometry A, 2009. **75**(4): p. 344-55.

248. Esposito, M., et al., *Bone vascular niche E-selectin induces mesenchymal-epithelial transition and Wnt activation in cancer cells to promote bone metastasis.* Nat Cell Biol, 2019. **21**(5): p. 627-639.

249. Campbell, J.P., et al., *Models of bone metastasis.* J Vis Exp, 2012(67): p. e4260.

250. Thies, K.A., et al., *Pathological Analysis of Lung Metastasis Following Lateral Tail-Vein Injection of Tumor Cells.* J Vis Exp, 2020(159).

251. Kuchimaru, T., et al., *A reliable murine model of bone metastasis by injecting cancer cells through caudal arteries.* Nat Commun, 2018. **9**(1): p. 2981.

252. Yu, C., et al., *Intra-iliac Artery Injection for Efficient and Selective Modeling of Microscopic Bone Metastasis.* J Vis Exp, 2016(115).

253. Wang, H., et al., *The osteogenic niche promotes early-stage bone colonization of disseminated breast cancer cells.* Cancer Cell, 2015. **27**(2): p. 193-210.

254. Wang, H., et al., *The Osteogenic Niche Is a Calcium Reservoir of Bone Micrometastases and Confers Unexpected Therapeutic Vulnerability.* Cancer Cell, 2018. **34**(5): p. 823-839 e7.

255. Bado, I.L., et al., *The bone microenvironment increases phenotypic plasticity of ER(+) breast cancer cells.* Dev Cell, 2021. **56**(8): p. 1100-1117 e9.

256. Vanderburgh, J.P., et al., *Systemic delivery of a Gli inhibitor via polymeric nanocarriers inhibits tumor-induced bone disease.* J Control Release, 2019. **311-312**: p. 257-272.

257. Chen, X., et al., *Remodelling of the bone marrow microenvironment by stromal hyaluronan modulates the malignancy of breast cancer cells.* Cell Commun Signal, 2020. **18**(1): p. 89.

258. Raheem, O., et al., *A novel patient-derived intra-femoral xenograft model of bone metastatic prostate cancer that recapitulates mixed osteolytic and osteoblastic lesions.* J Transl Med, 2011. **9**: p. 185.

259. Holen, I. and M.A. Lawson, *In vivo Models Used in Studies of Bone Metastases*, in *Bone Cancer*, D. Heymann, Editor. 2010, Academic Press. p. Pages 347-363.

260. Johnson, L.C., et al., *Longitudinal live animal micro-CT allows for quantitative analysis of tumor-induced bone destruction.* Bone, 2011. **48**(1): p. 141-51.

261. Sowder, M.E. and R.W. Johnson, *Enrichment and detection of bone disseminated tumor cells in models of low tumor burden.* Sci Rep, 2018. **8**(1): p. 14299.

262. Stripecke, R., et al., *Immune response to green fluorescent protein: implications for gene therapy.* Gene Ther, 1999. **6**(7): p. 1305-12.

263. Gambotto, A., et al., *Immunogenicity of enhanced green fluorescent protein (EGFP) in BALB/c mice: identification of an H2-Kd-restricted CTL epitope.* Gene Ther, 2000. **7**(23): p. 2036-40.

264. Han, W.G., W.W. Unger, and M.H. Wauben, *Identification of the immunodominant CTL epitope of EGFP in C57BL/6 mice.* Gene Ther, 2008. **15**(9): p. 700-1.

265. Limberis, M.P., C.L. Bell, and J.M. Wilson, *Identification of the murine firefly luciferase-specific CD8 T-cell epitopes.* Gene Ther, 2009. **16**(3): p. 441-7.

266. Baklaushev, V.P., et al., *Luciferase Expression Allows Bioluminescence Imaging But Imposes Limitations on the Orthotopic Mouse (4T1) Model of Breast Cancer.* Sci Rep, 2017. **7**(1): p. 7715.

267. Subik, K., et al., *The Expression Patterns of ER, PR, HER2, CK5/6, EGFR, Ki-67 and AR by Immunohistochemical Analysis in Breast Cancer Cell Lines.* Breast Cancer (Auckl), 2010. **4**: p. 35-41.

268. Mota, A.L., et al., *Molecular characterization of breast cancer cell lines by clinical immunohistochemical markers.* Oncol Lett, 2017. **13**(6): p. 4708-4712.

269. Grigoriadis, A., et al., *Molecular characterisation of cell line models for triple-negative breast cancers.* BMC Genomics, 2012. **13**: p. 619.

270. Barnabas, N. and D. Cohen, *Phenotypic and Molecular Characterization of MCF10DCIS and SUM Breast Cancer Cell Lines.* Int J Breast Cancer, 2013. **2013**: p. 872743.

271. Prunier, C., et al., *Breast cancer dormancy is associated with a 4NG1 state and not senescence.* bioRxiv, 2020: p. 2020.11.20.367698.

272. Kaur, P., et al., *A mouse model for triple-negative breast cancer tumor-initiating cells (TNBC-TICs) exhibits similar aggressive phenotype to the human disease.* BMC Cancer, 2012. **12**: p. 120.

273. Le Naour, A., et al., *EO771, the first luminal B mammary cancer cell line from C57BL/6 mice.* Cancer Cell Int, 2020. **20**: p. 328.

274. Le Naour, A., A. Rossary, and M.P. Vasson, *EO771, is it a well-characterized cell line for mouse mammary cancer model? Limit and uncertainty.* Cancer Med, 2020. **9**(21): p. 8074-8085.

275. Chan, S.R., et al., *STAT1-deficient mice spontaneously develop estrogen receptor alpha-positive luminal mammary carcinomas.* Breast Cancer Res, 2012. **14**(1): p. R16.

276. Soule, H.D., et al., *A human cell line from a pleural effusion derived from a breast carcinoma.* J Natl Cancer Inst, 1973. **51**(5): p. 1409-16.

277. Brooks, S.C., E.R. Locke, and H.D. Soule, *Estrogen receptor in a human cell line (MCF-7) from breast carcinoma.* J Biol Chem, 1973. **248**(17): p. 6251-3.

278. Fazzari, A., et al., *The control of progesterone receptor expression in MCF-7 breast cancer cells: effects of estradiol and sex hormone-binding globulin (SHBG).* Mol Cell Endocrinol, 2001. **172**(1-2): p. 31-6.

279. Horwitz, K.B., M.E. Costlow, and W.L. McGuire, *MCF-7; a human breast cancer cell line with estrogen, androgen, progesterone, and glucocorticoid receptors.* Steroids, 1975. **26**(6): p. 785-95.

280. Keydar, I., et al., *Establishment and characterization of a cell line of human breast carcinoma origin.* Eur J Cancer, 1979. **15**(5): p. 659-70.

281. Barkan, D., et al., *Inhibition of metastatic outgrowth from single dormant tumor cells by targeting the cytoskeleton.* Cancer Res, 2008. **68**(15): p. 6241-50.

282. Kim, R.S., et al., *Dormancy signatures and metastasis in estrogen receptor positive and negative breast cancer.* PLoS One, 2012. **7**(4): p. e35569.

283. Ovadia, E.M., et al., *Understanding ER+ Breast Cancer Dormancy Using Bioinspired Synthetic Matrices for Long-Term 3D Culture and Insights into Late Recurrence.* Adv Biosyst, 2020. **4**(9): p. e2000119.

284. Carlson, P., et al., *Targeting the perivascular niche sensitizes disseminated tumour cells to chemotherapy.* Nature Cell Biology, 2019. **21**(2): p. 238-+.

285. Dall, G., et al., *Low Dose, Low Cost Estradiol Pellets Can Support MCF-7 Tumour Growth in Nude Mice without Bladder Symptoms.* J Cancer, 2015. **6**(12): p. 1331-6.

286. Ogba, N., et al., *Luminal breast cancer metastases and tumor arousal from dormancy are promoted by direct actions of estradiol and progesterone on the malignant cells.* Breast Cancer Res, 2014. **16**(6): p. 489.

287. Gottardis, M.M., S.P. Robinson, and V.C. Jordan, *Estradiol-stimulated growth of MCF-7 tumors implanted in athymic mice: a model to study the tumoristatic action of tamoxifen.* J Steroid Biochem, 1988. **30**(1-6): p. 311-4.

288. Shafie, S.M. and L.A. Liotta, *Formation of metastasis by human breast carcinoma cells (MCF-7) in nude mice.* Cancer Lett, 1980. **11**(2): p. 81-7.

289. Gustafsson, K.L., et al., *The role of membrane ERalpha signaling in bone and other major estrogen responsive tissues.* Sci Rep, 2016. **6**: p. 29473.

290. Cheng, J.N., et al., *Skeletal impact of 17beta-estradiol in T cell-deficient mice: age-dependent bone effects and osteosarcoma formation.* Clin Exp Metastasis, 2020. **37**(2): p. 269-281.

291. Lawson, D.A., et al., *Single-cell analysis reveals a stem-cell program in human metastatic breast cancer cells.* Nature, 2015. **526**(7571): p. 131-5.

292. Flanagan, L., et al., *SUM-159PT cells: a novel estrogen independent human breast cancer model system.* Breast Cancer Res Treat, 1999. **58**(3): p. 193-204.

293. Ithimakin, S., et al., *HER2 drives luminal breast cancer stem cells in the absence of HER2 amplification: implications for efficacy of adjuvant trastuzumab.* Cancer Res, 2013. **73**(5): p. 1635-46.

294. Clements, M.E. and R.W. Johnson, *PREX1 drives spontaneous bone dissemination of ER+ breast cancer cells.* Oncogene, 2020. **39**(6): p. 1318-1334.

295. Fidler, I.J., *Rationale and methods for the use of nude mice to study the biology and therapy of human cancer metastasis.* Cancer Metastasis Rev, 1986. **5**(1): p. 29-49.

296. Morris, V.L., et al., *Tumor progression and metastasis in murine D2 hyperplastic alveolar nodule mammary tumor cell lines.* Clin Exp Metastasis, 1993. **11**(1): p. 103-12.

297. Barkan, D., et al., *Metastatic growth from dormant cells induced by a col-I-enriched fibrotic environment.* Cancer Res, 2010. **70**(14): p. 5706-16.

298. Naumov, G.N., et al., *Persistence of solitary mammary carcinoma cells in a secondary site: a possible contributor to dormancy.* Cancer Res, 2002. **62**(7): p. 2162-8.

299. Capietto, A.H., et al., *Novel ERalpha positive breast cancer model with estrogen independent growth in the bone microenvironment.* Oncotarget, 2016. **7**(31): p. 49751-49764.

300. Weichselbaum, R.R., et al., *An interferon-related gene signature for DNA damage resistance is a predictive marker for chemotherapy and radiation for breast cancer.* Proc Natl Acad Sci U S A, 2008. **105**(47): p. 18490-5.

301. Widschwendter, A., et al., *Prognostic significance of signal transducer and activator of transcription 1 activation in breast cancer.* Clin Cancer Res, 2002. **8**(10): p. 3065-74.

302. Sheen-Chen, S.M., et al., *Signal transducer and activator of transcription 1 in breast cancer: analysis with tissue microarray.* Anticancer Res, 2007. **27**(4B): p. 2481-6.

303. Tymoszuk, P., et al., *High STAT1 mRNA levels but not its tyrosine phosphorylation are associated with macrophage infiltration and bad prognosis in breast cancer.* BMC Cancer, 2014. **14**: p. 257.

304. Cailleau, R., et al., *Breast tumor cell lines from pleural effusions.* J Natl Cancer Inst, 1974. **53**(3): p. 661-74.

305. Kang, Y., et al., *A multigenic program mediating breast cancer metastasis to bone.* Cancer Cell, 2003. **3**(6): p. 537-49.

306. Minn, A.J., et al., *Distinct organ-specific metastatic potential of individual breast cancer cells and primary tumors.* J Clin Invest, 2005. **115**(1): p. 44-55.

307. Peyruchaud, O., et al., *Early detection of bone metastases in a murine model using fluorescent human breast cancer cells: application to the use of the bisphosphonate zoledronic acid in the treatment of osteolytic lesions.* J Bone Miner Res, 2001. **16**(11): p. 2027-34.

308. Yoneda, T., et al., *A bone-seeking clone exhibits different biological properties from the MDA-MB-231 parental human breast cancer cells and a brain-seeking clone in vivo and in vitro.* J Bone Miner Res, 2001. **16**(8): p. 1486-95.

309. Aslakson, C.J. and F.R. Miller, *Selective events in the metastatic process defined by analysis of the sequential dissemination of subpopulations of a mouse mammary tumor.* Cancer Res, 1992. **52**(6): p. 1399-405.

310. Casey, A.E., W.R. Laster, Jr., and G.L. Ross, *Sustained enhanced growth of carcinoma EO771 in C57 black mice.* Proc Soc Exp Biol Med, 1951. **77**(2): p. 358-62.

311. Lelekakis, M., et al., *A novel orthotopic model of breast cancer metastasis to bone.* Clin Exp Metastasis, 1999. **17**(2): p. 163-70.

312. Monteran, L., et al., *Bone metastasis is associated with acquisition of mesenchymal phenotype and immune suppression in a model of spontaneous breast cancer metastasis.* Sci Rep, 2020. **10**(1): p. 13838.

313. Swami, S., et al., *Prevention of breast cancer skeletal metastases with parathyroid hormone.* JCI Insight, 2017. **2**(17).

314. Bolin, C., et al., *Oncostatin m promotes mammary tumor metastasis to bone and osteolytic bone degradation.* Genes Cancer, 2012. **3**(2): p. 117-30.

315. Hiraga, T. and T. Ninomiya, *Establishment and characterization of a C57BL/6 mouse model of bone metastasis of breast cancer.* J Bone Miner Metab, 2019. **37**(2): p. 235-242.

316. Johnson, R.W., et al., *TGF-beta promotion of Gli2-induced expression of parathyroid hormone-related protein, an important osteolytic factor in bone metastasis, is independent of canonical Hedgehog signaling.* Cancer Res, 2011. **71**(3): p. 822-31.

317. Guise, T.A., et al., *Evidence for a causal role of parathyroid hormone-related protein in the pathogenesis of human breast cancer-mediated osteolysis.* J Clin Invest, 1996. **98**(7): p. 1544-9.

318. Kusuma, N., et al., *Integrin-dependent response to laminin-511 regulates breast tumor cell invasion and metastasis.* Int J Cancer, 2012. **130**(3): p. 555-66.

319. Smith, B.A., et al., *Targeting the PyMT Oncogene to Diverse Mammary Cell Populations Enhances Tumor Heterogeneity and Generates Rare Breast Cancer Subtypes.* Genes Cancer, 2012. **3**(9-10): p. 550-63.

320. Johnson, R.W., et al., *The primary function of gp130 signaling in osteoblasts is to maintain bone formation and strength, rather than promote osteoclast formation.* J Bone Miner Res, 2014. **29**(6): p. 1492-505.

321. Cancer Genome Atlas, N., *Comprehensive molecular portraits of human breast tumours.* Nature, 2012. **490**(7418): p. 61-70.

322. Ye, I.C., et al., *Molecular Portrait of Hypoxia in Breast Cancer: A Prognostic Signature and Novel HIF-Regulated Genes.* Mol Cancer Res, 2018. **16**(12): p. 1889-1901.

323. Minn, A.J., et al., *Genes that mediate breast cancer metastasis to lung.* Nature, 2005. **436**(7050): p. 518-24.

324. Li, B., et al., *Fructose-1,6-bisphosphatase opposes renal carcinoma progression.* Nature, 2014. **513**(7517): p. 251-5.

325. Ryan, H.E., et al., *Hypoxia-inducible factor-1alpha is a positive factor in solid tumor growth.* Cancer Res, 2000. **60**(15): p. 4010-5.

326. Wagner, K.U., et al., *Cre-mediated gene deletion in the mammary gland.* Nucleic Acids Res, 1997. **25**(21): p. 4323-30.

327. Gruber, M., et al., *Acute postnatal ablation of Hif-2alpha results in anemia.* Proc Natl Acad Sci U S A, 2007. **104**(7): p. 2301-6.

328. Haase, V.H., et al., *Vascular tumors in livers with targeted inactivation of the von Hippel-Lindau tumor suppressor.* Proc Natl Acad Sci U S A, 2001. **98**(4): p. 1583-8.

329. Biju, M.P., et al., *Vhlh gene deletion induces Hif-1-mediated cell death in thymocytes.* Mol Cell Biol, 2004. **24**(20): p. 9038-47.

330. Rankin, E.B., et al., *Inactivation of the arylhydrocarbon receptor nuclear translocator (Arnt) suppresses von Hippel-Lindau disease-associated vascular tumors in mice.* Mol Cell Biol, 2005. **25**(8): p. 3163-72.

331. Zhang, X.H., et al., *Metastasis dormancy in estrogen receptor-positive breast cancer.* Clin Cancer Res, 2013. **19**(23): p. 6389-97.

332. Omokehinde, T. and R.W. Johnson, *GP130 Cytokines in Breast Cancer and Bone.* Cancers (Basel), 2020. **12**(2).

333. Ruehl, M., et al., *The elongated first fibronectin type III domain of collagen XIV is an inducer of quiescence and differentiation in fibroblasts and preadipocytes.* J Biol Chem, 2005. **280**(46): p. 38537-43.

334. Goto, R., et al., *Quantitative LC-MS/MS Analysis of Proteins Involved in Metastasis of Breast Cancer.* PLoS One, 2015. **10**(7): p. e0130760.

335. Kamalakaran, S., et al., *DNA methylation patterns in luminal breast cancers differ from non-luminal subtypes and can identify relapse risk independent of other clinical variables.* Mol Oncol, 2011. **5**(1): p. 77-92.

336. Morris, M.R., et al., *Identification of candidate tumour suppressor genes frequently methylated in renal cell carcinoma.* Oncogene, 2010. **29**(14): p. 2104-17.

337. Paschalis, E.P., et al., *Distribution of collagen cross-links in normal human trabecular bone.* J Bone Miner Res, 2003. **18**(11): p. 1942-6.

338. Wu, T.J., et al., *Studies on the microspheres comprised of reconstituted collagen and hydroxyapatite.* Biomaterials, 2004. **25**(4): p. 651-8.

339. Midura, R.J., et al., *Calcospherulites isolated from the mineralization front of bone induce the mineralization of type I collagen.* Bone, 2007. **41**(6): p. 1005-16.

340. Ansorge, H.L., et al., *Type XIV Collagen Regulates Fibrillogenesis: PREMATURE COLLAGEN FIBRIL GROWTH AND TISSUE DYSFUNCTION IN NULL MICE.* J Biol Chem, 2009. **284**(13): p. 8427-38.

341. Ma, J.H., L. Qin, and X. Li, *Role of STAT3 signaling pathway in breast cancer.* Cell Commun Signal, 2020. **18**(1): p. 33.

342. Song, M., et al., *AKT as a Therapeutic Target for Cancer.* Cancer Res, 2019. **79**(6): p. 1019-1031.

343. McCubrey, J.A., et al., *Roles of the Raf/MEK/ERK pathway in cell growth, malignant transformation and drug resistance.* Biochim Biophys Acta, 2007. **1773**(8): p. 1263-84.

344. Ruppender, N.S., et al., *Matrix rigidity induces osteolytic gene expression of metastatic breast cancer cells.* PLoS One, 2010. **5**(11): p. e15451.

345. Barkan, D., J.E. Green, and A.F. Chambers, *Extracellular matrix: a gatekeeper in the transition from dormancy to metastatic growth.* Eur J Cancer, 2010. **46**(7): p. 1181-8.

346. Nakazawa, M.S., B. Keith, and M.C. Simon, *Oxygen availability and metabolic adaptations.* Nat Rev Cancer, 2016. **16**(10): p. 663-73.

347. Courtnay, R., et al., *Cancer metabolism and the Warburg effect: the role of HIF-1 and PI3K.* Mol Biol Rep, 2015. **42**(4): p. 841-51.

348. Fallah, J. and B.I. Rini, *HIF Inhibitors: Status of Current Clinical Development.* Curr Oncol Rep, 2019. **21**(1): p. 6.

349. Jin, L., et al., *Breast cancer lung metastasis: Molecular biology and therapeutic implications.* Cancer Biol Ther, 2018. **19**(10): p. 858-868.

350. Fantozzi, A. and G. Christofori, *Mouse models of breast cancer metastasis.* Breast Cancer Res, 2006. **8**(4): p. 212.

351. Dower, C.M., et al., *Selective Reversible Inhibition of Autophagy in Hypoxic Breast Cancer Cells Promotes Pulmonary Metastasis.* Cancer Res, 2017. **77**(3): p. 646-657.

352. Vera-Ramirez, L., et al., *Autophagy promotes the survival of dormant breast cancer cells and metastatic tumour recurrence.* Nat Commun, 2018. **9**(1): p. 1944.

353. Fluegen, G., et al., *Phenotypic heterogeneity of disseminated tumour cells is preset by primary tumour hypoxic microenvironments.* Nat Cell Biol, 2017. **19**(2): p. 120-132.

354. Keith, B., R.S. Johnson, and M.C. Simon, *HIF1alpha and HIF2alpha: sibling rivalry in hypoxic tumour growth and progression.* Nat Rev Cancer, 2011. **12**(1): p. 9-22.

355. Li, J., et al., *PTHrP drives breast tumor initiation, progression, and metastasis in mice and is a potential therapy target.* J Clin Invest, 2011. **121**(12): p. 4655-69.

356. Kiriyama, T., et al., *Transforming growth factor beta stimulation of parathyroid hormone-related protein (PTHrP): a paracrine regulator?* Mol Cell Endocrinol, 1993. **92**(1): p. 55-62.

357. Yin, J.J., et al., *TGF-beta signaling blockade inhibits PTHrP secretion by breast cancer cells and bone metastases development.* J Clin Invest, 1999. **103**(2): p. 197-206.

358. Masuda, T., et al., *ANGPTL2 increases bone metastasis of breast cancer cells through enhancing CXCR4 signaling.* Sci Rep, 2015. **5**: p. 9170.

359. Seagroves, T.N., et al., *VHL deletion impairs mammary alveologenesis but is not sufficient for mammary tumorigenesis.* Am J Pathol, 2010. **176**(5): p. 2269-82.

360. Parker, K.D., et al., *Microbiome Composition in Both Wild-Type and Disease Model Mice Is Heavily Influenced by Mouse Facility.* Front Microbiol, 2018. **9**: p. 1598.

361. Fessler, J., V. Matson, and T.F. Gajewski, *Exploring the emerging role of the microbiome in cancer immunotherapy.* J Immunother Cancer, 2019. **7**(1): p. 108.

362. Gopalakrishnan, V., et al., *The Influence of the Gut Microbiome on Cancer, Immunity, and Cancer Immunotherapy.* Cancer Cell, 2018. **33**(4): p. 570-580.

363. Champy, M.F., et al., *Mouse functional genomics requires standardization of mouse handling and housing conditions.* Mamm Genome, 2004. **15**(10): p. 768-83.

364. Zhang, H., et al., *HIF-1-dependent expression of angiopoietin-like 4 and L1CAM mediates vascular metastasis of hypoxic breast cancer cells to the lungs.* Oncogene, 2012. **31**(14): p. 1757-70.

365. Goto, Y., et al., *UCHL1 provides diagnostic and antimetastatic strategies due to its deubiquitinating effect on HIF-1alpha.* Nat Commun, 2015. **6**: p. 6153.

366. Wong, C.C., et al., *Hypoxia-inducible factor 1 is a master regulator of breast cancer metastatic niche formation.* Proc Natl Acad Sci U S A, 2011. **108**(39): p. 16369-74.

367. Dunn, G.P., L.J. Old, and R.D. Schreiber, *The immunobiology of cancer immunosurveillance and immunoediting.* Immunity, 2004. **21**(2): p. 137-48.

368. Andrews, L.P., H. Yano, and D.A.A. Vignali, *Inhibitory receptors and ligands beyond PD-1, PD-L1 and CTLA-4: breakthroughs or backups.* Nat Immunol, 2019. **20**(11): p. 1425-1434.

369. Mantovani, A., et al., *Tumour-associated macrophages as treatment targets in oncology.* Nat Rev Clin Oncol, 2017. **14**(7): p. 399-416.

370. Sceneay, J., et al., *Primary tumor hypoxia recruits CD11b+/Ly6Cmed/Ly6G+ immune suppressor cells and compromises NK cell cytotoxicity in the premetastatic niche.* Cancer Res, 2012. **72**(16): p. 3906-11.

371. Deep, G., et al., *Exosomes secreted by prostate cancer cells under hypoxia promote matrix metalloproteinases activity at pre-metastatic niches.* Mol Carcinog, 2020. **59**(3): p. 323-332.

372. Yu-Lee, L.Y., et al., *Osteoblast-Secreted Factors Mediate Dormancy of Metastatic Prostate Cancer in the Bone via Activation of the TGFbetaRIII-p38MAPK-pS249/T252RB Pathway.* Cancer Res, 2018. **78**(11): p. 2911-2924.

373. Yu-Lee, L.Y., et al., *Bone secreted factors induce cellular quiescence in prostate cancer cells.* Sci Rep, 2019. **9**(1): p. 18635.

374. Martin, T.J. and R.W. Johnson, *Multiple actions of parathyroid hormone-related protein in breast cancer bone metastasis.* Br J Pharmacol, 2019.

375. Fleming, N.I., et al., *Parathyroid hormone-related protein protects against mammary tumor emergence and is associated with monocyte infiltration in ductal carcinoma in situ.* Cancer Res, 2009. **69**(18): p. 7473-9.

376. Henderson, M., et al., *Parathyroid hormone-related protein production by breast cancers, improved survival, and reduced bone metastases.* J Natl Cancer Inst, 2001. **93**(3): p. 234-7.

377. Henderson, M.A., et al., *Parathyroid hormone-related protein localization in breast cancers predict improved prognosis.* Cancer Res, 2006. **66**(4): p. 2250-6.

378. Micucci, C., et al., *HIF2alpha is involved in the expansion of CXCR4-positive cancer stem-like cells in renal cell carcinoma.* Br J Cancer, 2015. **113**(8): p. 1178-85.

379. Zhang, J. and Q. Zhang, *VHL and Hypoxia Signaling: Beyond HIF in Cancer.* Biomedicines, 2018. **6**(1).

380. Minervini, G., M. Pennuto, and S.C.E. Tosatto, *The pVHL neglected functions, a tale of hypoxia-dependent and -independent regulations in cancer.* Open Biol, 2020. **10**(7): p. 200109.

381. Okuda, H., et al., *The von Hippel-Lindau tumor suppressor protein mediates ubiquitination of activated atypical protein kinase C.* J Biol Chem, 2001. **276**(47): p. 43611-7.

382. Iturrioz, X., et al., *The von Hippel-Lindau tumour-suppressor protein interaction with protein kinase Cdelta.* Biochem J, 2006. **397**(1): p. 109-20.

383. Pal, S., et al., *The von Hippel-Lindau gene product inhibits vascular permeability factor/vascular endothelial growth factor expression in renal cell carcinoma by blocking protein kinase C pathways.* J Biol Chem, 1997. **272**(44): p. 27509-12.

384. Guo, J., et al., *pVHL suppresses kinase activity of Akt in a proline-hydroxylation-dependent manner.* Science, 2016. **353**(6302): p. 929-32.

385. Gould, C.M. and A.C. Newton, *The life and death of protein kinase C.* Curr Drug Targets, 2008. **9**(8): p. 614-25.

386. Newton, A.C., *Protein kinase C: poised to signal.* Am J Physiol Endocrinol Metab, 2010. **298**(3): p. E395-402.

387. Hinz, N. and M. Jucker, *Distinct functions of AKT isoforms in breast cancer: a comprehensive review.* Cell Commun Signal, 2019. **17**(1): p. 154.